Order Number 9328609

Evidence of solar oscillations in Rayleigh-scattered light

Germain, Marvin Edward, Ph.D.

The University of Arizona, 1993

U·M·I
300 N. Zeeb Rd.
Ann Arbor, MI 48106

EVIDENCE OF SOLAR OSCILLATIONS IN RAYLEIGH-SCATTERED LIGHT

by

Marvin Edward Germain

A Dissertation Submitted to the Faculty of the

DEPARTMENT OF PHYSICS

In Partial Fulfillment of the Requirements
For the Degree of

DOCTOR OF PHILOSOPHY

In the Graduate College

THE UNIVERSITY OF ARIZONA

1 9 9 3

THE UNIVERSITY OF ARIZONA
GRADUATE COLLEGE

As members of the Final Examination Committee, we certify that we have read the dissertation prepared by Marvin Edward Germain

entitled Evidence of Solar Oscillations in Rayleigh-Scattered Light

and recommend that it be accepted as fulfilling the dissertation requirement for the Degree of Doctor of Philosophy

Henry A. Hill	5-6-93 Date
John D. McCall	May 6 '93 Date
Charles T. Tindal	6 May '93 Date
Lyle Kien	My 6, 93 Date
R. H. Parmenter	5/6/93 Date

Final approval and acceptance of this dissertation is contingent upon the candidate's submission of the final copy of the dissertation to the Graduate College.

I hereby certify that I have read this dissertation prepared under my direction and recommend that it be accepted as fulfilling the dissertation requirement.

Henry A. Hill	5-6-93
Dissertation Director	Date

STATEMENT BY AUTHOR

This dissertation has been submitted in partial fulfillment of requirements for an advanced degree at The University of Arizona and is deposited in the University Library to be made available to borrowers under the rules of the Library.

Brief quotations from this dissertation are allowable without special permission, provided that accurate acknowledgement of source is made. Requests for permission for extended quotation from or reproduction of this manuscript in whole or in part may be granted by the copyright holder.

SIGNED: Marvin E. Germain

ACKNOWLEDGEMENTS

I wish to acknowledge the following individuals who have contributed to the success of this project: Professor Henry Hill who conceived of the sky monitor and contributed several key insights into the noise reduction problem; Don Fraser who provided the opto-mechanical design and assisted with the fabrication and assembly of the instrument; and Dr. Paul Oglesby who provided the data-acquisition software and the design of the I/O board, assisted in modifying the A-to-D board, and whose constant encouragement and expert advice made completion of this project possible.

Important scientific discussions were also held with Dr. Chris Cornuelle, Dr. Yeming Gu and Ron Kroll. I would also like to express my thanks to Dr. Yeming Gu for providing the data for figures 1.1 and 1.2, and to William Hunter for his assistance in preparing figure 2.1. Critical readings of the manuscript were provided by Professor Hill and Dr. Paul Oglesby, and editorial assistance was provided by Elaine Segura and Dr. Ross Rosenwald. Finally, I would like to express my deepest gratitude to my entire family for their patience and generosity throughout these long years at SCLERA.

This work was funded in part by a grant from the National Aeronautics and Space Administration.

for my mother

TABLE OF CONTENTS

TABLE OF CONTENTS–continued

LIST OF ILLUSTRATIONS

LIST OF ILLUSTRATIONS–continued

LIST OF TABLES

ABSTRACT

A new instrument has been developed for making unimaged whole-disk observations of low-degree solar normal-mode oscillations. The apparatus, referred to as the *sky monitor*, does not track the solar disk, but instead measures the radiant flux scattered by the Earth's atmosphere at 1.6 and 0.5 μ. The expected diurnal flux variation was obtained from a detailed radiative transfer calculation. Data was acquired for 15.5 months during 1991–92. Seventy-two days of data were analyzed for evidence of solar p modes in the frequency range 1800–4776 μHz. Noise generated by the Earth's atmosphere was reduced by scaling the Fourier amplitude computed from the infrared signal and subtracting it from the Fourier amplitude computed from the visible signal. A superimposed frequency analysis was then performed which revealed $\sim 2\ \sigma$ peaks within 0.3 μHz of symmetry-allowed locations, while no excess power was detected at the symmetry-forbidden frequencies. The probability of obtaining by chance the observed excess power density at symmetry-allowed frequencies and deficit of power density at symmetry-forbidden frequencies was computed to be 6.9×10^{-3}. Correcting the frequencies for solar-cycle variations, the probability was reduced to 2.9×10^{-4}. These results indicate that it is quite unlikely that the observed symmetry properties have occurred by chance, and support the hypothesis that solar normal-mode signals are manifested in the data. The amplitudes $\mathcal{I}'/\mathcal{I}_\circ$ averaged over radial order n of the $\ell = 0$ and $\ell = 2$, $m = 0$ modes were found to be $(7.54 \pm 0.54) \times 10^{-7}$ and $(7.68 \pm 0.56) \times 10^{-7}$, respectively. These results are about a factor of two smaller than the amplitude of total irradiance oscillations measured from space. While the rotational splitting of the $\ell = 2$ multiplet appears to be consistent with that reported by Hill (1985a), results for $\ell = 1$ and $\ell = 3$ are inconclusive.

Chapter 1

Detection of Solar Oscillations

1.1 Introduction

No object in nature is more vital to life on Earth than the Sun. The Sun drives the weather and climate and provides the energy which sustains the entire food web. Today, serious gaps exist in our understanding of solar structure and dynamics. For example, the solar cycle, the low neutrino flux, and the high coronal temperature all remain unaccounted for. The richest source of information about the solar interior is the phenomenon of global solar oscillations, the study of which is known as *helioseismology*. Assuming a solar model, the frequencies of normal modes of oscillation can be predicted. Conversely, accurate measurement of these frequencies allows one to work backwards, obtaining knowledge of the solar interior. Thus, observation of global solar oscillations will play a central role in furthering our understanding of the Sun.

Strategies for detecting solar oscillations fall into three broad categories: (1) The velocity field of the Sun's outer layers is inferred from the Doppler shifts of spectral lines; (2) Diameter and differential radius measurements detect changes in the Sun's *limb-darkening* function, which is sensitive to temperature perturbations in the Sun's outer layers; (3) Perturbations in radiation intensity are measured in spectral lines and in the continuum. Comparison of different observations has led to disagreement over the frequency and amplitude of oscillations. This is due in part to the weakness of the signals, and in part to the complicated manner in which oscillations are manifested in velocity, limb darkening, and intensity measurements. Resolution of these discrepancies will necessarily involve new independent observations.

Toward this end, a new instrument has been developed which measures radiation intensity at two wavelengths in the continuum. This instrument, referred to hereafter as the *sky monitor*, is unique in that it does not track the Sun, but instead measures the intensity of light scattered by the Earth's atmosphere. The simplicity of design results in low cost and high reliability, which are particularly important in helioseismology. In addition, it eliminates an entire class of systematic errors associated with tracking of the solar disk. Noise due to the Earth's atmosphere is vastly reduced by combining information from both wavelengths. A detailed description of the sky monitor is provided in Chapter 2. Chapter 3 describes the data acquisition and reduction in the time domain. The results of frequency-domain analysis are presented in Chapter 4. The remainder of this chapter is devoted to the development of

relevant concepts within a historical framework, and to a discussion of observational techniques.

1.2 Five-Minute Oscillations

Solar oscillations were first observed at Mount Wilson observatory in the Doppler shifts of spectral lines (Leighton 1961; Leighton, Noyes and Simon 1962). The oscillations had periods of about 300 seconds, and have come to be known as the *five-minute oscillations*. These observations were soon confirmed by other researchers (Evans and Michard 1962; Howard 1962) but their interpretation remained problematic for more than a decade. Many attempts were made to identify these oscillations as either acoustic or gravity waves propagating in the solar envelope (see Stein and Leibacher 1974). Acoustic and gravity waves may be differentiated on the basis of their restoring forces. Pressure differences act as the restoring force in the case of acoustic waves, while buoyancy is the restoring force for gravity waves.

A powerful tool in understanding the nature of the five-minute oscillations is the diagnostic, or $k-\omega$ diagram in which contours of constant oscillatory power density are plotted as a function of frequency and horizontal wave number. To use this information to evaluate a model of solar oscillations, one also needs a theoretical dispersion relation such as

$$k_z^2 = \frac{\omega^2 - \omega_{ac}^2}{c^2} - k_h^2\left(1 - \frac{N^2}{\omega^2}\right) \tag{1.1}$$

(Whitaker 1963). Here, ω is the frequency of oscillation and k_z and k_h are the vertical and horizontal wave numbers, respectively. The *acoustic cutoff* frequency ω_{ac} is the minimum frequency at which an acoustic wave can propagate, and c is the local sound speed. The *Brunt-Väisälä* frequency N is the frequency at which a volume of fluid oscillates about its equilibrium height due to buoyancy. The characteristic frequencies N and ω_{ac} and the sound speed c are functions of radius, and can be computed from a solar model. Thus, for given k_h and ω, waves will be trapped in propagation zones where k_z^2 is positive, and will be evanescent elsewhere. For a given range of altitudes, the locus of oscillatory power density can be plotted on the diagnostic diagram. These curves can then be compared with the observed concentrations of power density in the k_h–ω plane.

Using the data of Evans and Michard (1962), Mein (1966) constructed a diagnostic diagram and concluded that acoustic waves with periods above 240 seconds are evanescent in the solar atmosphere. Similarly, Frazier (1968) found that gravity waves with periods of five minutes cannot propagate in the solar atmosphere. He conjectured that the convection zone might be a propagation region for the observed five-minute oscillations. This insight proved to be correct. In 1970, Ulrich used equation (1.1) to predict the locus of power density in the diagnostic diagram assuming the five-minute oscillations were standing acoustic waves trapped in the convection zone. Ulrich's theoretical curves were in close agreement with the power density found by Frazier (Ulrich 1970).

While Ulrich's theory had met with some success, there was evidence that this was not the whole story. Gonzi and Roddier (1969) found that the temporal coherence of the five-minute oscillations was at least one hour, and Musman and Rust (1970) had observed spatial coherence extending over 50,000 km. Moreover, Reif and Musman (1971) presented evidence that the observed oscillations were due to interference between two or more oscillations. These observations prompted Wolff (1972) to suggest that the five-minute oscillations were in fact a superposition of global normal modes of oscillation. Such modes would have horizontal spatial properties given by the spherical harmonics $Y_\ell^m(\vartheta,\varphi)$, where the angular degree ℓ is the number of nodal lines on a spherical surface, and the azimuthal order m is the number of longitudinal nodal lines.

1.3 Normal Modes

In the case of global oscillations, $k_h^2 = \ell(\ell+1)/r^2$, where r is the solar radius. Introducing the *Lamb frequency*, $L_\ell^2 = \ell(\ell+1)c^2/r^2$, the dispersion relation (1.1) may be rewritten as

$$k_z^2 = \frac{1}{\omega^2 c^2}(\omega^2 - L_\ell^2)(\omega^2 - N^2). \tag{1.2}$$

Here, advantage has been taken of the near equality of N and ω_{ac} (Shibahashi 1990). It is now clear that waves can propagate if $\omega > N, L_\ell$ or $\omega < N, L_\ell$. Normal modes falling into the first category are pressure modes (p modes) since pressure is the operative restoring force, while normal modes of the second type are called gravity modes

(g modes) because they are restored by buoyancy. Gravity modes are intrinsically *nonradial*, having $\ell > 0$. Lifetimes of the modes range from about five days for five-minute oscillations to thousands of years for g modes and low-order, low-degree p modes.

Figure 1.1 shows $N/2\pi$ and $L_\ell/2\pi$ as functions of fractional radius computed from the standard solar model of Christensen-Dalsgaard (1990). The base of the photosphere corresponds to $r/R = 1$. From the figure it can be seen that the propagation zone for p modes is strongly ℓ dependent. Pressure modes with $\ell \gtrsim 30$ are confined to about the outer 50% by radius. Purely radial ($\ell = 0$) p modes for which $L_\ell = 0$ penetrate to the core. The g-mode propagation zone extends from the core to the base of the convection zone. The Brunt-Väisälä frequency drops to zero at that point since the turbulent conditions which prevail in the convection zone preclude buoyant oscillations. Conditions in the deep solar interior can be inferred only from a study of g modes and low-degree p modes.

A wave equation for global solar oscillations can be derived beginning with the equations for conservation of mass, momentum and energy. The oscillations are usually assumed to be nearly adiabatic since the thermal time scale associated with heat transport is much longer than a period of oscillation. The amplitudes of solar oscillations are small, permitting the use of first-order perturbation theory. This results in a linearized fourth-order set of differential equations for the oscillatory perturbations in density, pressure, displacement, and gravitational potential (Unno

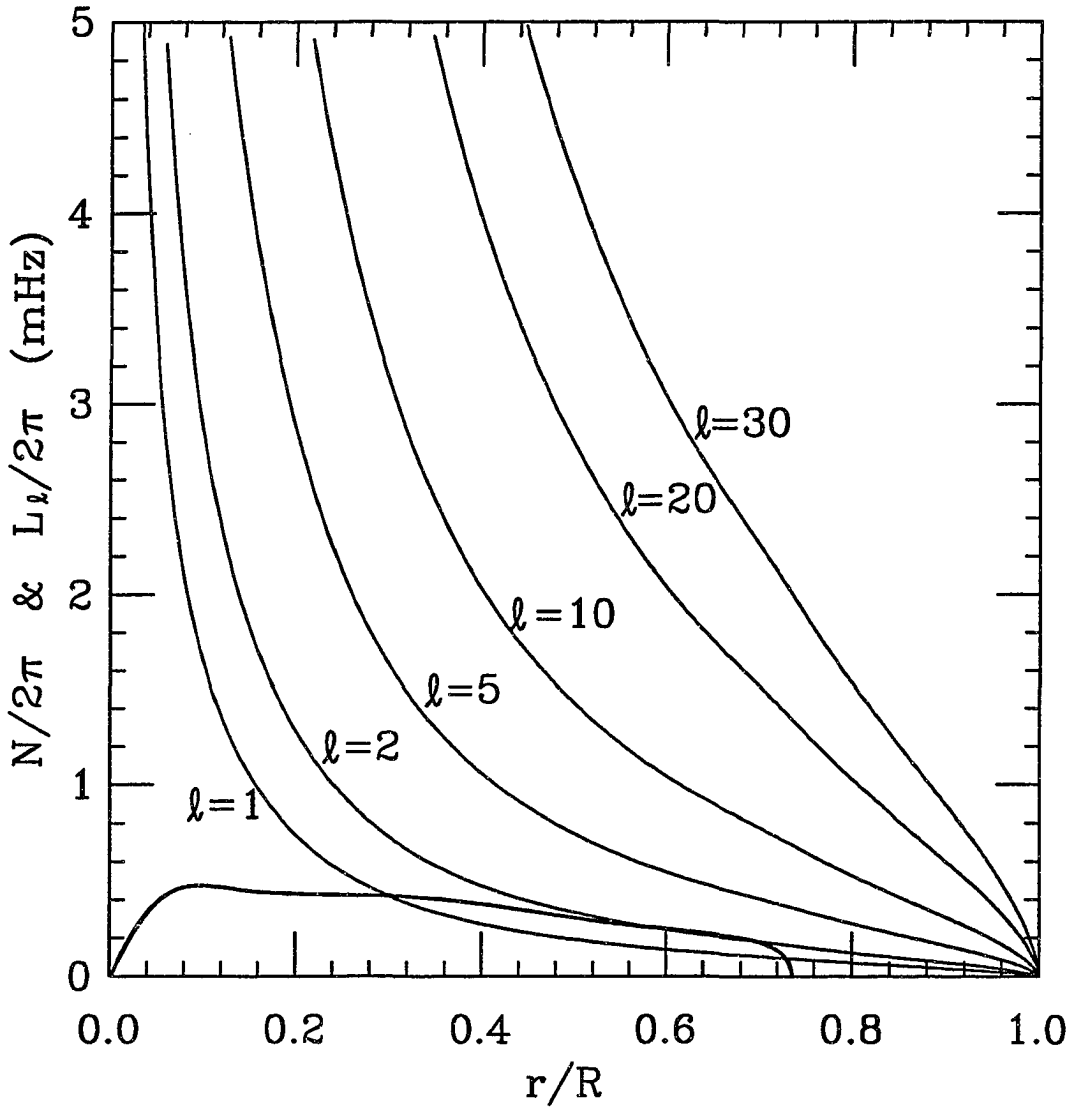

Figure 1.1: The Lamb frequency L_ℓ for ℓ = 1, 2, 5, 10, 20, and 30, and the Brunt-Väisälä frequency N (bold line) as functions of the fractional radius.

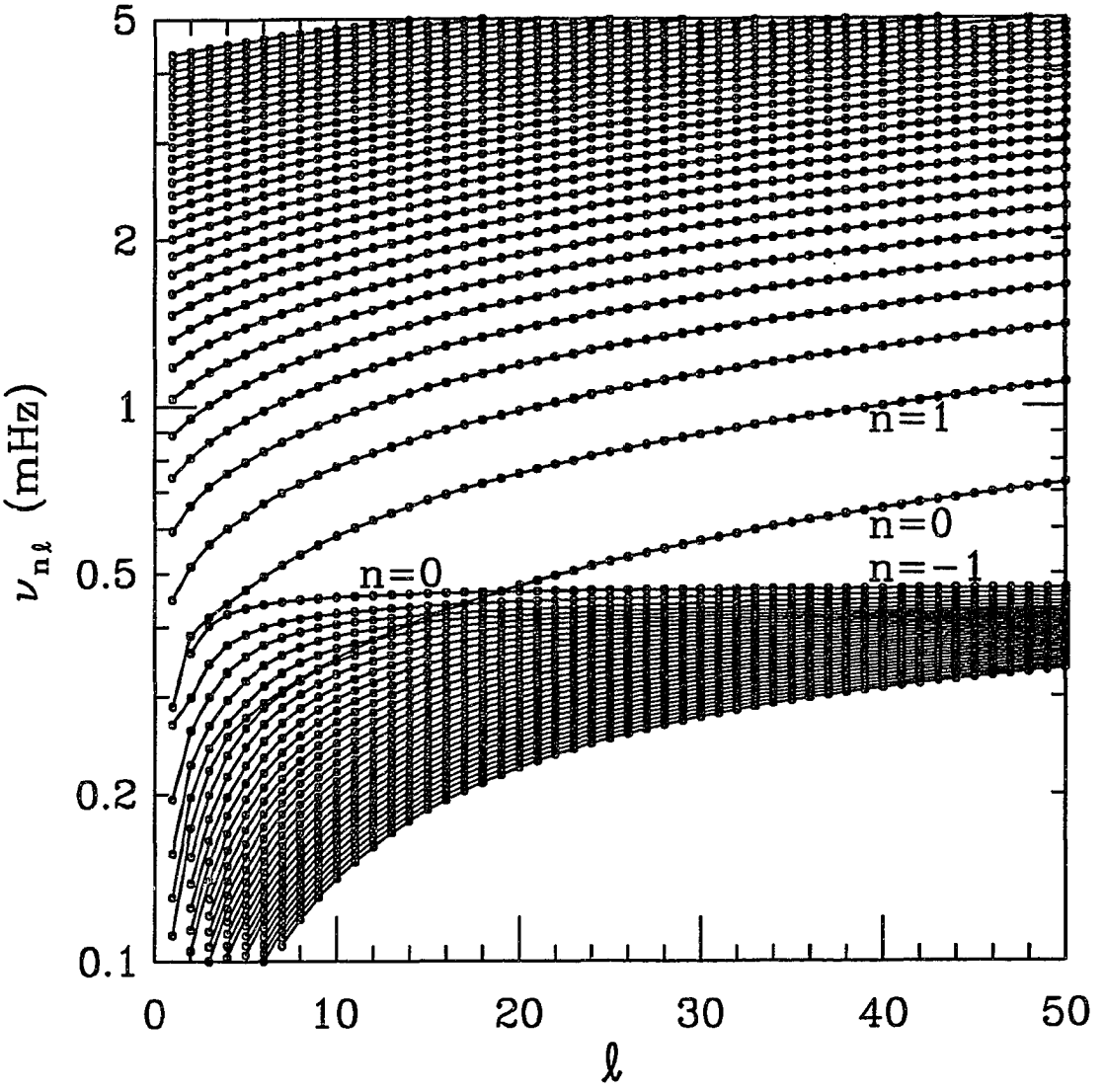

Figure 1.2: Spectrum of solar oscillations. Curves connect modes with the same n.

et al. 1979). The eigenfunctions have depth-dependent amplitudes and a number of radial nodes given by the magnitude of the radial order n. By convention, $n > 0$ for p modes and $n < 0$ for g modes, while $n = 0$ corresponds to the fundamental, or f modes.

Figure 1.2 shows the position of axisymmetric ($m = 0$) normal modes in the ℓ–ν plane. The concentration of power along the lines of constant n is a primary prediction of the normal-mode hypothesis and is invaluable in mode classification. For a given n, the frequencies are seen to increase with k_h (or ℓ). The g modes are more closely spaced than the p modes and, for a given ℓ, lie at frequencies entirely below the p-mode spectrum. The f modes follow the p mode spectrum for high ℓ values, but become g modes at low ℓ. A family of modes having the same n and ℓ is called a *multiplet*. There are $2\ell + 1$ modes in a multiplet since m takes on integer values from $-\ell$ to ℓ. Their frequencies would be degenerate in the case of spherical symmetry, but are split into a Zeemann-like pattern due to rotation. This implies that for $m \neq 0$, the modes behave as travelling waves, either prograde or retrograde with respect to rotation. By convention, $m < 0$ for prograde and $m > 0$ for retrograde modes. The properties of a mode are determined primarily at the depth where the amplitude of oscillation is largest. The rotational splitting of a multiplet reflects the weighted average of the rotation rate as a function of radius.

1.4 Early Observations

The first direct evidence of global solar oscillations is found in the 1973 oblateness measurements of Hill and Stebbins (Richard 1974; Hill and Stebbins 1975). These observations were obtained with the SCLERA telescope described by Oleson *et al.* (1974). SCLERA is an acronym for The Santa Catalina Laboratory for Experimental Relativity by Astrometry. Measurements of the oblateness, defined as the difference between equatorial and polar diameters, are inherently global in nature. Figure 10 of Richard clearly shows quasi-periodic oscillations with periods of about 30 minutes in the oblateness measurements. The operational definition of *diameter* used at SCLERA is the distance between diametrically opposed edges of the solar disk which are determined by the Finite Fourier Transform Definition, or FFTD. To apply the FFTD, the limb is scanned from radial position $r_0 - a$ to $r_0 + a$, where a, the *scan amplitude*, is typically several arcseconds. The FFTD of the edge is the point r_0 at which the integral

$$F(r_0, \lambda) = \int_{-a}^{a} G(r, \lambda) \cos\left[2 \arcsin\left(\frac{r - r_0}{a}\right)\right] dr \tag{1.3}$$

vanishes (Hill, Stebbins and Oleson 1975; Hill and Caudell 1979). This integral is sensitive to the shape of the limb-darkening function $G(r, \lambda)$ (Stebbins 1980; Bos and Hill 1983). It was recognized early on that shape changes in the limb-darkening function, as opposed to mass motions, are primarily responsible for the observed diameter oscillations (Hill, Stebbins and Brown 1976). New diameter measurements

in 1975 led to the first publication of global oscillation periods (Hill, Stebbins and Brown 1976; Christensen-Dalsgaard and Gough 1976).

In 1976, two groups published results of global Doppler studies. The first group, working at the Crimean Astrophysical Observatory, used a grating spectrograph to measure the differential line-of-sight velocity between a 0.66 solar radii region at disk center and the remaining outer annulus (Severny, Kotov and Tsap 1976). They detected a single global oscillation with a period of 160 minutes. The second group, at the University of Birmingham, used a *resonant scattering spectrometer* (Brookes, Isaak and van der Raay 1978) to measure the line-of-sight velocity integrated over the entire disk (Brookes *et al.* 1976). They published four periods, the longest of which was in rough agreement with the 160-minute oscillation reported by the Crimean group. Meanwhile, the five-minute oscillations were conclusively identified as normal modes by comparing high-resolution diagnostic diagrams with detailed theoretical calculations (Deubner 1975; Rhodes, Ulrich and Simon 1977) and through whole-disk velocity observations (Claverie *et al.* 1979).

Long-period oscillations had been reported earlier by Fossat and Ricort (1973), but they retracted their claim, attributing their observations to transparency changes in the Earth's atmosphere (Fossat and Ricort 1975). This did not bode well for the Birmingham group since their instruments were quite similar. Grec and Fossat suggested that SCLERA's results could be explained by differential refraction due to fluctuations in air mass along the line of sight (Grec and Fossat 1977; Fossat *et al.*

1977). This mechanism could not account, however, for the observed phase coherence in the SCLERA data (Caudell and Hill 1980). In addition, the difference in oscillatory power obtained using two different scan amplitudes clearly demonstrated that shape changes in the limb-darkening function were producing the observations at SCLERA (Hill and Caudell 1979). Capitalizing on this result, the 1979 SCLERA observations measured the *differential radius* at six points on and near the solar equator. Differential radius is defined as the difference in the edge location computed using two different scan amplitudes. Each of the six measurements was sensitive to shape changes of the limb-darkening function only in a small neighborhood about one limb position, thereby reducing the amplitude of differential refraction effects by a factor of 300 relative to diameter observations. Information from the six limb positions was used to test the symmetry properties of the normal modes whose horizontal spatial properties were expected to be those of the spherical harmonics (Bos and Hill 1983).

The solar origin of the 160-minute oscillation was questioned since 160 minutes is precisely one-ninth of a day. Fossat and Grec (1978; Grec and Fossat 1979) argued that the Crimean technique enhanced the eighth, ninth and tenth harmonics of spurious diurnal signals. The existence of the signal was confirmed by Scherrer and Wilcox at Stanford University using an instrument very similar to that of the Crimean group (Scherrer *et al.* 1979). The phases reported by the two groups were also in close agreement. Grec and Fossat (1979) pointed out that this phase correlation could be accounted for in terms of terrestrial atmospheric effects, since the two

observatories were nearly 4 × 160 minutes apart in longitude. Eventually, observations from the South Pole confirmed the solar origin of the 160-minute oscillation. It was found to have a period more precisely of 160.01 minutes (Scherrer *et al.* 1980) and to be in phase as measured at the South Pole, in the Crimea, and at Stanford (Grec, Fossat and Pomerantz 1980).

1.5 Detection Sensitivity

Doppler shifts of spectral lines due to line-of-sight velocities are detected through the difference in intensity measured at two wavelengths nominally equidistant from line center. Such observations are sensitive to $\omega\,\delta r$, where δr is the Lagrangian perturbation in radius due to an oscillation with angular frequency ω. Oscillations in the five-minute band are found to have $\delta r/r \sim 10^{-5}$, and are easily detected by this method. Sensitivity is reduced for oscillations of longer period, however. It has been suggested that the 160-minute oscillation is actually detected through an *apparent* velocity which arises due to a combination of intensity perturbations and solar rotation (Hill, Tash and Padin 1986). The spectral lines used in whole-disk and differential velocity observations are broadened by solar rotation. Oscillation-induced differences in the intensity of light emanating from the east and west hemispheres will produce a time-varying line asymmetry which mimics a Doppler shift. This mechanism allows the detection of modes that would otherwise be inaccessible to velocity techniques. Since intensity perturbations are strongly depth dependent, sensitivity to apparent velocities will depend on the height of formation of the observed spectral line. It has

been found that Crimean observations of the Fe I 5124 line formed at $\tau_{0.5} = 0.05$ are three to four times more sensitive to apparent velocities than resonant-scattering spectrometer observations using the Na I 5896 and K 7699 lines formed at $\tau_{0.5} \sim 10^{-3}$ (Germain and Hill 1987).

The fractional temperature perturbation due to an oscillation is three orders of magnitude larger than the fractional displacement in the photosphere (Hill, Caudell and Rosenwald 1977; Hill, Rosenwald and Caudell 1978). However, efforts to detect long-period temperature perturbations through intensity measurements have been problematic (Livingston, Milkey and Slaughter 1977; Musman and Nye 1977; Beckers and Ayres 1977). Using the observations of Tanenbaum *et al.* (1969) and the theory of wave propagation in the photosphere due to Hill, Rosenwald and Caudell (1978), Hill, Caudell and Rosenwald (1977) found that the response in continuum intensity for the five-minute oscillations is a factor of 35 below that expected for a black body. It was also found that the temperature sensitivity of some spectral lines is one to two orders of magnitude below that predicted from static line-formation theory (Hill, Caudell and Rosenwald 1977; Hill, Livingston and Caudell 1977). These studies illustrate the complexity of the relationship between temperature and intensity in the photosphere. When spectral lines are used as temperature probes, the measured amplitudes may be reduced since the time required for an atomic species to reach equilibrium after an environmental change may be comparable to the period of oscillation (Hill, Caudell and Rosenwald 1977). Also, a photospheric temper-

ature increase leads to an increase in opacity which tends to partially cancel the expected intensity increase (Hill, Caudell and Rosenwald 1977; Hill, Livingston and Caudell 1977; Hill, Tash and Padin 1986). This produces the strong depth dependence mentioned above. Herein lies the advantage of SCLERA-type measurements, since strongly depth-dependent temperature perturbations are manifested in shape changes of the limb-darkening function.

The effect of aperture geometry on detection sensitivity is determined by the *spatial filter function*, which can be obtained for a given ℓ and m by integrating the observable quantity weighted by $Y_\ell^m(\vartheta,\varphi)$ over the aperture (Hill 1978). For whole-disk observations, the spatial filter function is zero if $\ell+m$ is odd due to the antisymmetry of these modes with respect to reflections about the equator. For whole-disk velocity observations, the spatial filter function peaks at $\ell = 1$ (Christensen-Dalsgaard and Gough 1982) and then decreases as ℓ^{-3} (Hill 1978). In contrast, Hill found that the spatial filter function of whole-disk intensity measurements decreases as $\ell^{-3/2}$. The spatial filter function has also been computed (Hill 1978) for differential velocity measurements. It remains high for $\ell < 12$ and decreases as ℓ^{-2} for $\ell \geq 12$. Also, for a given ℓ, the sensitivity increases monotonically with m, approximately doubling between $m = 0$ and $m = \ell$. For SCLERA observations, the sensitivity remains high for $\ell \lesssim 40$ due to the small effective aperture associated with a scan of the limb. The sensitivity of these observations is strongly m dependent, increasing by a factor of 6 between $m = 0$ and $m = 10$ (Hill, Alexander and Caudell 1985).

1.6 Sampling

The amplitude and phase of an oscillatory signal of a given period can be estimated from a time series of data by finding the best-fit sine wave. The statistical stability of this estimate is maximized in a *superposed epoch* analysis in which the time string is divided into segments of length equal to the period under consideration. A sine wave is then fit to the superposition of these segments using the least-squares criterion. An alternative approach is to compute the discrete Fourier transform of the time series. For each frequency ν, the discrete Fourier transform produces a real and imaginary Fourier component, denoted by a_ν and b_ν, respectively. The amplitude at a given frequency is $A_\nu = \sqrt{a_\nu^2 + b_\nu^2}$ and the phase is $\phi_\nu = \arctan(b_\nu/a_\nu)$. The function $A^2(\nu)$ is commonly referred to as a *power spectrum*. If the total length of time spanned by a data set is τ, then the resolution of the power spectrum, or the frequency interval between independent points, is $1/\tau$. The Fourier-transform method is computationally advantageous due to the availability of highly efficient Fast Fourier Transform, or FFT, algorithms. Scargle (1982) has shown that power spectrum analysis and superposed epoch analysis are equivalent. Therefore, only the Fourier-transform method will be considered in the remainder of this work.

The highest frequency signal that can be represented in a power spectrum is the *Nyquist* frequency, equal to half the sampling rate. If the time series is not band-width limited before sampling to frequencies below the Nyquist frequency, higher frequency signals will produce *alias* peaks in the power spectrum. The alternat-

ing pattern of data and gaps into which a time string is divided due the Earth's rotation, inclement weather or equipment malfunction is referred to as the *window function*. This causes a redistribution of power from central signal peaks into distant sidelobes, or *sidebands*. The strongest sidebands are due to the Earth's rotation at 1/day = 11.57 μHz from the central peak. As a rule, the greater the duty cycle of a time series, the lower will be the 1/day sidebands. The finite length of a data set also results in leakage of power from signal peaks into nearby sidelobes. This effect can be mitigated to some extent by smoothly tapering the ends of each time string to zero (Blackman and Tukey 1958).

Duty cycles of 100% over many days are achievable in principle by observing from the South Pole, from space, or by the use of global networks of observing stations. Global networks of ground-based observing stations are the best long-term solution to the demands of helioseismology. It has been found that at least six stations are required for nearly continuous, year-round observation (F. Hill and Newkirk 1985). Networks are in operation or under development employing imaging and nonimaging velocity and intensity techniques as well as limb-darkening measurements (see F. Hill 1990). Observations from the geographic South Pole have been made by groups using a variety of techniques (Stebbins and Wilson 1983; Duvall, Harvey and Pomerantz 1986; Fossat, Gelly and Grec 1989). Duty cycles of over 90% have been obtained for ten-day observing runs. The irregular spacing of interruptions due to weather makes corrections for these gaps feasible (Harvey 1990). Antarctic observations also

have the advantages of exceptional atmospheric transparency, and nearly constant solar zenith angle. Although conditions are harsh and logistical support is difficult, Antarctic expeditions are economically attractive in comparison to space missions.

Observations from space are free of all atmospheric interference and again offer the possibility of continuous data. Space-borne observations suffer from a different set of problems, however. Spacecraft are subject to large velocity variations which complicate line-of-sight velocity measurements. Observations with high spatial resolution are difficult due to the requirement of accurate pointing. Also, the large volume of data involved in such measurements poses a challenge in telemetry. Measurements of the Sun's total irradiance obtained with the Active Cavity Radiometer Irradiance Monitor (ACRIM) aboard the Solar Maximum Mission (SMM) satellite were analyzed for p modes by Woodard and Hudson (1983), and for g modes by Fröhlich and Delache (1984) and by Hill and Kroll (1986). The SMM did not permit continuous observation, however, as it was not originally designed for helioseismology. One-hundred-sixty days of uninterrupted irradiance measurements were obtained by the IPHIR (InterPlanetary Helioseismology by IRradiance measurements) experiment aboard the Soviet PHOBOS mission to Mars. This data resulted in a very high resolution power spectrum substantially free of sidelobes (Fröhlich *et al.* 1990). The SOlar and Heliospheric Observatory (SOHO) under development by the European Space Agency will carry three helioseismological instruments in 1995 (Domingo 1990).

1.7 Noise

A time series may be contaminated by random or quasi-periodic noise originating in the instrument, the Earth's atmosphere, or on the Sun. Instrumental noise is highly dependent on the experimental arrangement, but the systematic effects of tracking the apparent motion of the Sun across the sky apply to nearly all ground-based helioseismology experiments. Accurate servo-controlled tracking is critical for observing modes of high angular degree since image motion will effectively lower the spatial resolution. Servo-loops can introduce spurious oscillations into the data, however, and so must be designed with great care. Active tracking systems may also have deleterious effects on low- or no-resolution intensity observations. The error signals for a servo-controlled tracking system come from samples of the intensity at several points near the solar limb. Intensity differences due to solar oscillations can masquerade as a tracking error, causing a slight displacement of the servo-controlled image position. The net result is a lowering of sensitivity for intensity observations of low-degree modes.

Atmospheric seeing, caused by turbulence in the Earth's atmosphere, produces blurring of the solar image. This will tend to degrade observations of high-degree modes (Ulrich *et al.* 1984). The FFTD of the solar edge used in SCLERA observations is by design quite insensitive to atmospheric seeing. Of more concern is the effect of differential refraction by the Earth's atmosphere. It has been mentioned that beginning with the 1979 season, SCLERA measured the differential radius in-

stead of the diameter in order to eliminate differential refraction as a source of error. Differences in air mass along the line of sight which may give rise to differential refraction can also interfere with velocity observations. Unequal atmospheric transparency along the line of sight to the east and west hemispheres of the Sun will produce spurious apparent velocity signals in observations with low spatial resolution.

Atmospheric transparency fluctuations are an even more serious source of noise in intensity observations. Oglesby (1987) has developed a method of differentiating intensity changes due to transparency fluctuations and those due to solar temperature perturbations. He measured the intensity at 48 wavelengths from 0.5 to 1.7 μ at disk center. Temperature perturbations are expected to produce wavelength-dependent changes in intensity. In particular, intensity perturbations in the near infrared are expected to be out of phase with intensity perturbations at 0.5 μ. Atmospheric transparency changes cause intensity perturbations that are wavelength independent. Oglesby performed a least-squares polynomial fit to the intensity as a function of wavelength. He then Fourier analyzed the linear coefficient in the expansion obtaining excellent agreement with the results of differential radius observations.

Granulation is the visible manifestation of convection below the photosphere. The rising gas in the center of a granular cell is hotter than the sinking material around the periphery of the cell. The net effect is an apparent blue shift of spectral lines observed near disk center. The effect is absent near the limb since the granular motion there is perpendicular to the line of sight (Jiménez *et al.* 1988). Super granulation is

manifested primarily as horizontal flows, however, which does result in velocity noise at the limb. Worden and Simon (1976) invoked super granular cells rotating through the field of view to explain the observed 160-minute oscillation. This explanation was insufficient to account for the observed phase coherence, however. Brown *et al.* (1978) estimated the fraction of the power in the 1975 diameter observations that could be ascribed to granulation to be $\lesssim 2\%$. While granulation must be considered when high spatial resolution is used, its effects tend to average out in whole-disk observations.

Solar activity is an important noise source for whole-disk intensity and velocity observations. Solar active regions can have lifetimes of several months. As active regions rotate across the solar disk, they produce a slow modulation of both velocity and intensity signals. This generates sidebands in the power spectra spaced at about 0.42 μHz which may easily be mistaken for rotational splitting (Hill *et al.* 1991). Rotation of active regions also produces very long period signals in whole-disk observations. This is illustrated by the 13-day period signal reported by the Birmingham group (Claverie *et al.* 1982; Isaak *et al.* 1984). Detailed analyses indicated that these observations could be accurately reproduced by considering the effect of solar activity (Durrant and Schröter 1983; Andersen and Maltby 1983; Edmunds and Gough 1983). Andersen (1984) has found that the Fe I 5124 line used by the Crimean group is less strongly influenced by solar activity than the potassium and sodium lines used in resonant-scattering spectrometers.

Random noise that is not identically removed from the data can be driven down in amplitude by averaging large amounts of data either in the time or frequency domain. Broad-band noise will be divided into as many independent frequency bins as are available, so that the signal-to-noise ratio in a given frequency bin can often be increased simply by increasing resolution. Even quasi-periodic noise may be handled in this way if the noise source has a coherence time that is short compared to the lifetime of solar oscillations. Phenomena which fall into this category include g modes in the Earth's atmosphere which have lifetimes of about three hours (Volland 1988).

1.8 Mode Classification

In order to use frequency determinations to infer conditions in the solar interior, modes must be classified by their n, ℓ, and m values. Five-minute oscillations were the first modes to be successfully classified. High-resolution diagnostic diagrams allowed a direct association between frequencies and ℓ values. Moreover, the distinctive ridge-pattern in the k–ω plane permits unambiguous n classification of the modes. A single day of data provides sufficient frequency resolution to classify axisymmetric ($m = 0$) five-minute oscillations with $\ell \gtrsim 140$ (Deubner, Ulrich and Rhodes 1979; Rhodes *et al.* 1981; F. Hill, Toomre and November 1983). Low-degree axisymmetric five-minute oscillations with $0 \leq \ell \leq 3$ and $n > 10$ have been classified by comparing the results of unimaged, whole-disk velocity observations with the theoretical frequency distribution (Grec, Fossat and Pomerantz 1983). Similarly, Scherrer *et*

al. (1983) contributed the classifications of $\ell = 4$ and 5 modes using differential velocity data. The gap was bridged by Duvall and Harvey (1983) who used velocity data spanning 74 hours to construct a very high resolution diagnostic diagram. This allowed unambiguous ℓ and n classification of modes with $\ell > 16$. In addition, they pushed their classifications down to $\ell = 2$ by extrapolation of the resolved ridges in the k-ω plane, thereby confirming the n classification of low-degree five-minute oscillations.

At this point, a consensus had been established regarding classification of the axisymmetric five-minute oscillations. Reasonable agreement was also obtained for the rotation-induced frequency splitting of high-degree p mode multiplets. As these modes are confined to a cavity near the solar surface, it is not surprising that their splittings are close to the observed surface rotation rate (see Harvey 1988). Such agreement is not found in the rotational splitting results for low-degree ($\ell \leq 5$) p modes. Woodard (1984), in an analysis of ACRIM data, has set an upper limit on the $\ell = 1$ splitting of 0.5 μHz. While Henning and Scherrer (1986) and Fröhlich (1990) find values below this limit, Duvall and Harvey (1984) reported a splitting of 0.66 μHz, and the Birmingham group has found splittings of 0.75 μHz (Claverie *et al.* 1981; Isaak 1986). The low-degree rotational splittings obtained at SCLERA are about 1.8 μHz (Hill 1985a). These discrepancies translate into disagreement in the core rotation rate by a factor of six. Thus, the internal rotation rate of the Sun must be considered an open question.

Detection of g modes and low-order, low-degree p modes by velocity techniques is difficult due to the low frequencies of these modes. Classifications of low-order low-degree p modes have been reported by SCLERA (Hill 1984) and by Angura Gubau *et al.* (1990). Direct comparison of these results is not possible since there is very little overlap between the modes classified by the two groups. The SCLERA classifications, obtained from differential radius observations, have been supported by an analysis of intensity observations (Oglesby 1987), and by an analysis of diameter data obtained in 1978 (Hill and Caudell 1985). Six groups have contributed classifications of low-degree g modes, the most extensive set being that of SCLERA (Hill 1985b; Hill and Gu 1990). A detailed comparison of the different sets of g mode classifications has been provided by Hill *et al.* (1991). They find no significant correlation among the various sets but, once again, Oglesby (1987) found a significant correlation between the SCLERA frequencies and peaks in his power spectrum obtained from intensity observations. Evidence of the classified g modes was also found in the 1978 diameter data (Hill 1992). The rotational splittings of the g modes and low-order, low-degree p modes, obtained as an integral part of the SCLERA mode-classification procedure, form an internally consistent set, and are consistent with splittings found for the higher-order p modes.

1.9 Whole-Disk Intensity Observations

The subject of this work is a new method of obtaining unimaged whole-disk intensity observations of solar oscillations. Whole-disk observations project out modes with angular degrees $\ell = 0$ to ≈ 3. The adiabatic condition, assumed in the computation of eigenfrequencies, breaks down in the photosphere where the oscillations are manifested. The theoretical treatment of nonadiabatic normal modes predicts the ratio of intensity perturbation to line-of-sight velocity as a function of frequency of oscillation (Gough 1980). This ratio has been measured by several researchers with differing results. Jiménez *et al.* (1988) found that the ratio of the log of the intensity perturbation to the velocity amplitude decreased by an order of magnitude between 2.5 and 3.5 mHz, while Fröhlich and van der Raay (1984) obtained a strong peak in the ratio at 3 mHz. On the other hand, Libbrecht (1990) found only weak frequency dependence. Theoretical and observational studies at SCLERA indicate that the ratio of intensity perturbation to velocity amplitude increases by a factor of about 20 in going from a period of five minutes to one hour (Hill 1985a). It appears that more work is needed in this area.

Unsuccessful ground-based attempts to observe whole-disk intensity oscillations at frequencies below the five-minute band have been made by Beckers and Ayres (1977) and Livingston, Milkey and Slaughter (1977). Claverie *et al.* (1981) was unsuccessful in identifying five-minute oscillations in ground-based, whole-disk intensity observations, while Deubner (1981), Schmidt-Kaler and Winkler (1984), and Jiménez

et al. (1987) obtained positive results marginally above the detection threshold. Terrestrial atmospheric noise has been the limiting factor in these observations. Various schemes have been proposed for increasing the signal-to-noise ratio in whole-disk intensity measurements. Andersen (1986) suggested taking the ratio of the intensity in an absorption line to that in the continuum. He assumed that the solar signal would have reduced amplitude in the continuum while fluctuations in transmission through the Earth's atmosphere would be equal in amplitude at two closely spaced wavelengths. Jefferies *et al.* (1988) tried unsuccessfully to reduce atmospheric noise by dividing the intensity transmitted by a filter with a passband of 7 Å by that transmitted by a filter having a passband of 400 Å. The idea was that the solar signal would be weaker for the broader passband, while the atmospheric noise signal would be the same for both filters. Fröhlich (1984) attempted to avoid atmospheric noise by flying photometers aboard a balloon. He also obtained only marginal results. The best whole-disk intensity observations of the five-minute oscillations are those from the ACRIM space-borne instrument (Woodard and Hudson 1983).

In principle, the noise-reduction technique of Oglesby (1987) described in § 1.7 could be extended to whole-disk observations. Oglesby used the wavelength dependence of intensity oscillations in the time domain to discriminate against atmospheric noise. An alternative approach would be to take advantage of wavelength-dependent differences in the frequency domain. This course was followed by Andersen and Domingo (1989). Taking the ratio of oscillatory power outside the five-minute band

obtained at 0.5 and 0.87 μ, they scaled the power at one wavelength by this ratio and subtracted it from the power at the other wavelength within the five-minute band. Assuming that the power outside the five-minute band is entirely due to noise, and that the ratio of this power obtained at different optical wavelengths is frequency independent, some cancellation of terrestrial noise can be expected. One pitfall of such a procedure is that the solar signal is likely to be attenuated in the process as well. In the present work, a similar approach is taken, but care is taken to ensure that significant attenuation of the solar signal does not occur. Also, in a distinct departure from previous work, only the intensity of light scattered from the Earth's atmosphere is measured in the current study. The successful application of this method to scattered light would suggest that similar success may be expected in observations of direct sunlight. The method could be extended from two to three wavelengths, thereby enabling the observer to reduce the contribution of solar noise. This work therefore has important implications for the data-reduction methodology that will be adopted for the three-color photometric telescopes currently being installed as part of the SCLERA international network (Oglesby 1993).

Chapter 2

The Sky Monitor

2.1 Opto-Mechanical Design

The sky monitor is designed to measure the spectral flux of scattered light within a solid angle of 0.035 sr at 0.5 and 1.6 μ. The instrument, located atop the Gould-Simpson Science Building on the University of Arizona campus, is rigidly fixed in an orientation parallel to the Earth's axis of rotation. This ensures that the scattering angle of light into the field of view is essentially constant for a given day. The decrease in potential down time resulting from the absence of a tracking system allows greater statistical stability in the power spectrum, as discussed in § 1.6. The low cost introduced by the simplicity of design is especially attractive in helioseismology where global networks of observing sites are often considered. The sky monitor is also free of a host of systematic errors that can be introduced by a poorly designed tracking

system. The absence of a tracking system implies that the sky monitor can make only unimaged, whole-disk intensity measurements of low-degree modes. Pressure modes of angular degree $\ell = 0 - 3$ are of particular interest since they yield information about the inner 20% of the Sun by radius.

The sky monitor can be thought of as four independent telescopes, each having a field of view of 5.2°. The four principle rays span 6.9° so that four slightly different regions of the sky are sampled simultaneously. This four-fold redundancy increases the probability of obtaining sufficient data to detect solar oscillations. The sky monitor is diagrammed in figure 2.1. A 10 cm objective having a focal length of one meter and mounted in a 64-mm-thick aluminum plate forms the entrance pupil. In a second plate that is parallel to the first are mounted four 2.5 cm field lenses having 3.5 cm focal lengths. The field lenses are uniformly spaced on a circle of radius 60 mm measured from the optical axis defined by the objective. The separation between the objective and field-lense plates is fixed at one meter by a set of 2.5-cm-diameter aluminum support rods. A filter wheel rotates in a plane 2.5 cm before and parallel to the field-lens plate. A pair of square interference filters, measuring 5.0 cm on a side, are mounted at opposite points on the filter wheel with their diagonals along a diameter. The wavelengths were chosen to avoid water vapor absorption lines in the Earth's atmosphere. Filter specifications are summarized in table 2.1. A synchronous motor mounted to the rear of the field-lens plate drives the filter wheel at a constant 72 rpm.

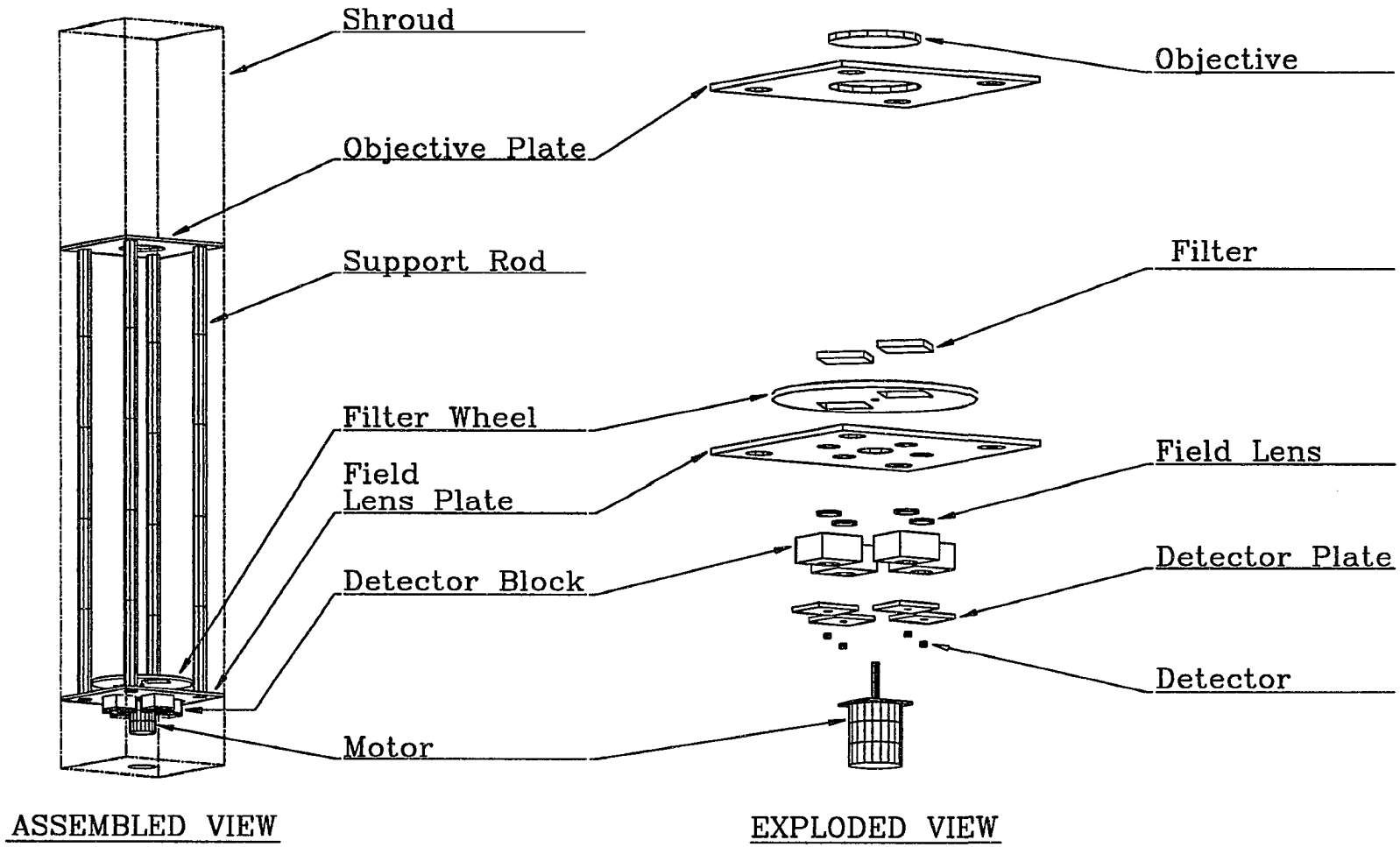

Figure 2.1: Opto-mechanical components of the sky monitor.

TABLE 2.1

Interference Filter Specifications

λ	Bandwidth	Transmittance	
		Pass Band	Stop Band
0.5 μ	.009 μ	0.4	10^{-4}
1.6 μ	.033 μ	0.4	10^{-4}

The aluminum frame is shrouded in plywood which extends 50 cm beyond the objective in order to block stray light. The frame and the inside of the shroud are painted flat black which reduces the scattering of light within the instrument. The outside of the instrument was originally painted white, but was later wrapped in aluminum foil as this was found to be less attractive to flying insects. In addition to the motor, the compartment behind the field-lense plate houses the electronics and a dual power supply which provides $\pm$15 V for the analog electronics and +5 V for the digital components. The power cords for the power supply and motor pass through line filters and exit on the right of the compartment as viewed from the rear. The analog and digital signal cables pass through an opening in the rear of the instrument and are at right angles to the power cords, minimizing coupling to the 60 Hz line voltage. The rear compartment is shielded by aluminum sheet metal tied to the telescope frame which serves as chassis ground. The power supply shield is also tied to chassis ground. The motor chassis is an integral part of the telescope frame by virtue of its mounting.

Four images of the objective are formed on the one-millimeter square detectors which lie 28 mm behind the field lenses on a circle of radius 62 mm. The detectors are of two types. Two germanium (Ge) detectors lie opposite one another along a line parallel to the horizon, while on a line perpendicular to this are mounted two lead sulfide (PbS) detectors. All are packaged in cylindrical TO-5 canisters and are mounted in 64-mm-thick teflon plates which provide both electrical and thermal isolation. The teflon detector plates are attached to four aluminum blocks which are in turn fixed to the back of the field-lense plate. Each block is fitted with threaded studs to which the analog detector circuits are attached. An image of the objective is somewhat larger than the active area of the respective detector so that mechanical vibrations are not directly manifested in the measured signals. Since the sensitivity of an optical radiation detector is typically nonuniform across the active area, an oscillatory signal can be produced by an inhomogeneous intensity distribution coupled with a mechanical vibration. Such inhomogeneities can arise in this application due to dust or dirt on the objective. This potential systematic error is removed by slightly defocusing the images of the objective in the detector plane.

2.2 Analog Electronics

The Ge and PbS detectors operate by different physical mechanisms, and so require different circuitry for their implementation. The PbS detectors are of the photoconductive type. Photons of sufficient energy incident on the PbS film excite electrons

from the valence band into the conduction band thereby increasing the conductivity (Dereniak and Crowe 1984). The conductivity can be expressed as

$$\sigma(\mathcal{F}_\lambda, T) = \sigma(0, T) + C(T)\mathcal{F}_\lambda^{\eta(T)}, \tag{2.1}$$

where $\mathcal{F}_\lambda$ is the radiant flux at the wavelength λ and T is the temperature. The temperature dependence represented by the coefficient $C(T)$ and the exponent $\eta(T)$ is determined by film preparation, and so differs from cell to cell. The quantity $1 - \eta(T)$ may be positive or negative with an absolute magnitude $\lesssim 0.5$ (Mahlman, Nottingham and Slater 1956).

Conductivity variations are converted to a voltage signal by a voltage divider as in figure 2.2. The series resistor R_s was chosen to be equal to the average resistance of the PbS film, producing the maximum voltage change for a given change in conductivity. Latching relays were used to switch a 45 V instrumentation battery into and out of the circuit with only a momentary current in the relay. A second set of relays allowed the battery to be tested without having permanant test leads connected to the circuit. The test and switch leads are routed to a control panel at the top of the instrument so that opening of the rear compartment is rarely necessary. The batteries were tested daily and replaced when the voltage difference dropped below 30 V. The relays and battery cases were grounded directly to the chassis. All analog and digital returns were tied to the chassis at a single point.

As seen in figure 2.2, the PbS detector circuit contains four operational amplifiers labeled A1–A4. The input signal to A2 is lowpass filtered with a time constant of 10 s,

integrating over about 12 revolutions of the filter wheel. This is used as a reference signal, denoted by S_R, and is primarily a measure of temperature. The input signal to A1 is lowpass filtered with a time constant of 1.4 ms, allowing rapid settling of the signal when the aperture is opened or closed. The difference between the inputs to A1 and A2 is amplified by a factor of 96 and transmitted to a multiplexer circuit via shielded, twisted-pair cable. The difference signal emerging from the multiplexer circuit will be denoted by S_λ when the aperture is open, and by S_d for the dark, or closed-aperture case. From the circuit in figure 2.2 and equation (2.1) it can be seen that $S_\lambda - S_d \propto \mathcal{F}_\lambda^\eta$. The reference signal S_R is buffered by A4 before transmission to the multiplexer board by a separate cable. The cable shields are tied to ground only on the detector boards, minimizing noise coupling (Ott 1988). The small current into the input of A4 could introduce an asymmetry in the temperature dependence of the outputs of A1 and A2. This effect is compensated by the additional resistor in the feedback network of A2.

The eight differential signal lines are multiplexed to a single shielded, twisted-pair cable which communicates the data to a Burr-Brown A-to-D converter located in a laboratory approximately 8 m below. The transmission line is driven by a pair of LF355 operational amplifiers in a differential-amplifier configuration. The source impedances of the twisted pair are balanced for improved noise immunity (Ott 1988). The gain of the differential amplifier is 19 when the signals S_λ or S_d are selected. This results in a difference signal $S_{0.5}$ ($> S_{1.6}$) of 3 – 6 V at midday. When the

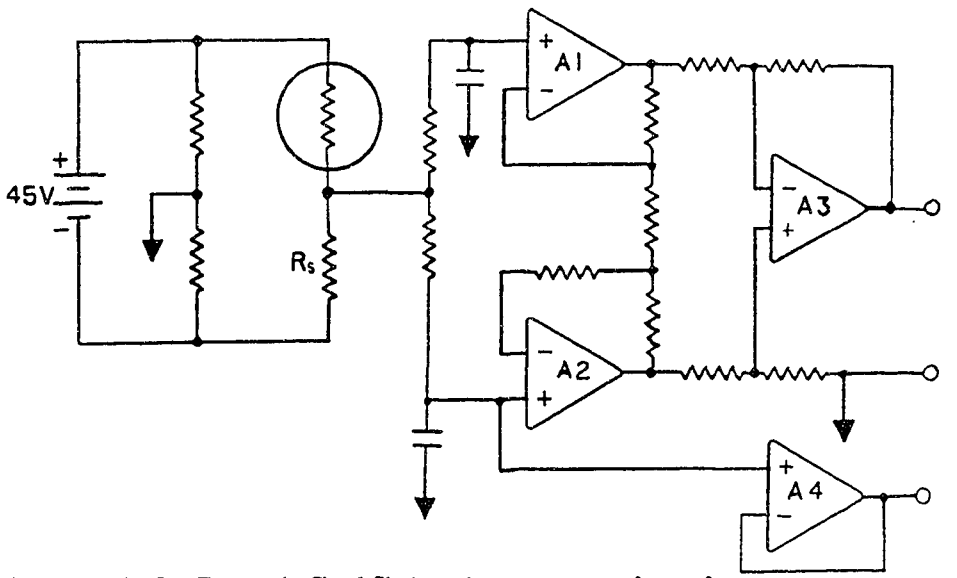

Figure 2.2: Lead-Sulfide detector circuit.
The PbS photoconductor is circled.

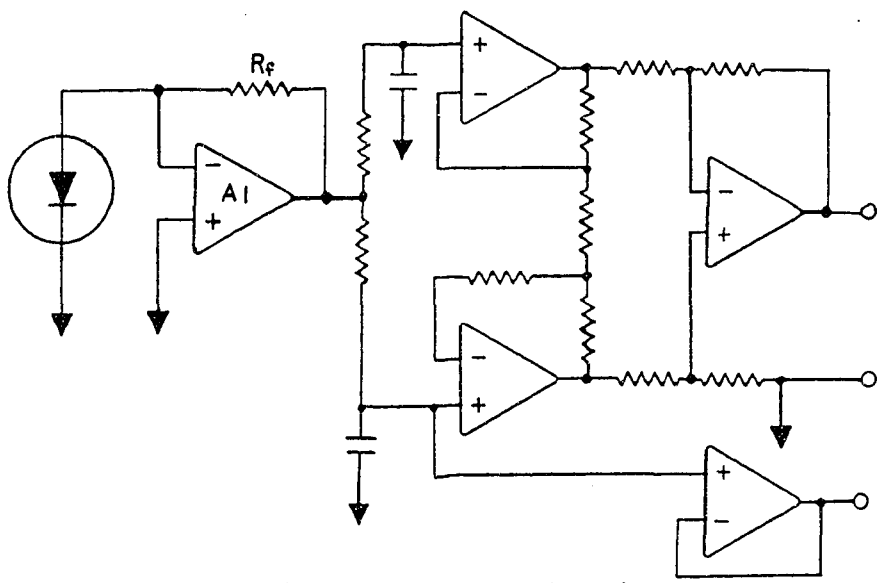

Figure 2.3: Germanium detector circuit.
The Ge photodiode is circled.

reference signals S_R are selected, the differential amplifier is converted into a pair of followers having a gain of unity. This keeps the reference signals within the ±10 V range of the A-to-D.

The Ge detectors are of the photovoltaic type. They contain a P-N junction so that when valence electrons are excited into the conduction band by an incident photon, a small current is generated. This current produces a voltage drop across R_f, shown in figure 2.3, which is proportional to the incident flux. The resistor R_f was chosen to give a voltage signal of about the same magnitude as the PbS signal. The low-noise amplifier A1 maintains the detector in a zero-bias configuration, minimizing detector noise (Dereniak and Crowe 1984). The output stage of the Ge circuit is identical to that of the PbS circuit. The Ge reference signal S_R was found to be $\sim 10^3$ times less than that of the PbS detector. Since the sensitivity of the Ge detector is only weakly temperature dependent, the Ge reference signal was much less valuable as a calibration signal than the PbS reference signal. Calibration is discussed in detail in Chapter 3.

2.3 Digital Electronics

The data acquisition system is shown in block form in figure 2.4. The heart of this system is the timing circuit which controls the multiplexing and the digital filtering, triggers the 12-bit Burr-Brown A-to-D converter, and sends interrupts to the Harris computer when data is to be transferred to the hard disk. The timing circuit is driven

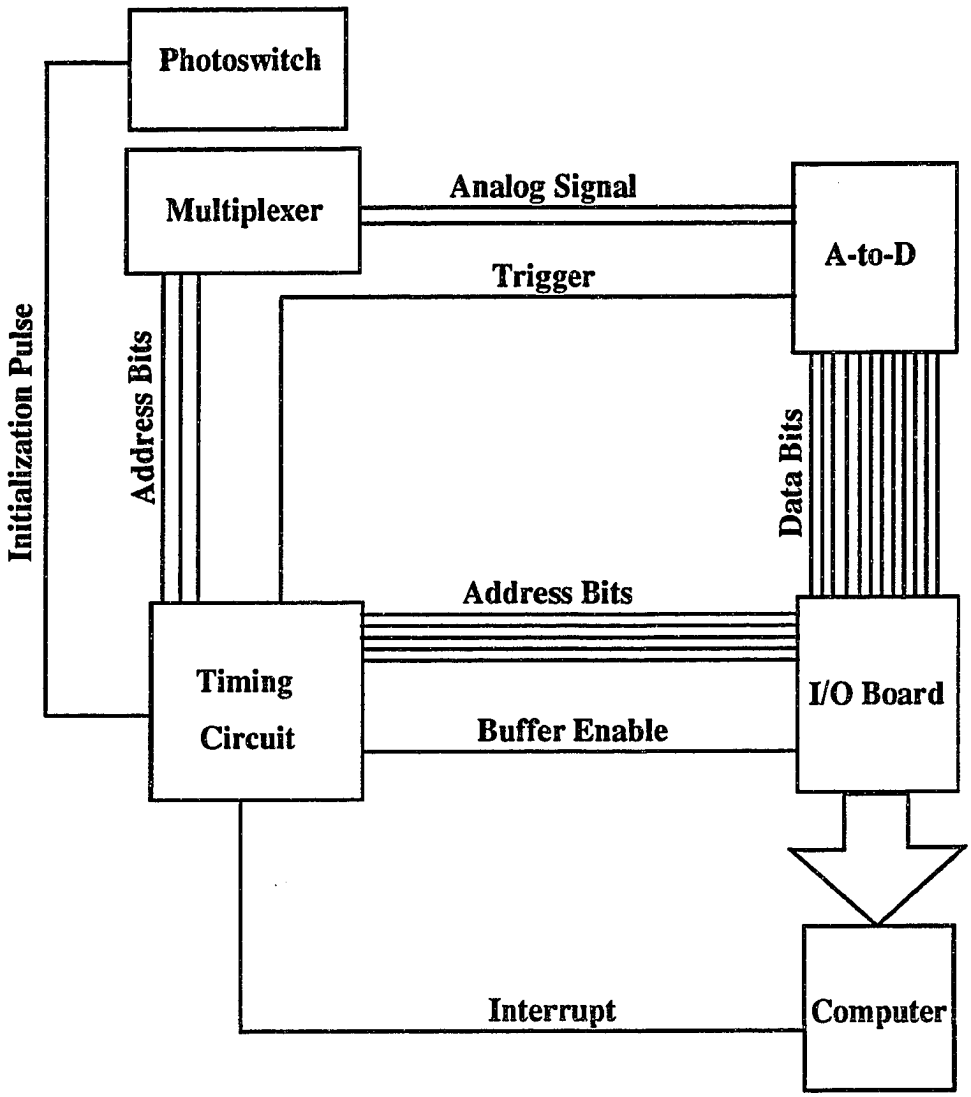

Figure 2.4: Data-Acquisition System.

by a 1 MHz quartz oscillator, and is initialized by means of a photoswitch mounted to one of the aluminum support rods. A thin aluminum needle attached to the edge of the filter wheel adjacent to the 0.5 μ filter interrupts the switch beam at the beginning of each cycle, producing a 1 ms pulse in the normally-high switch output. The switch position is adjusted so that the output returns high just at the moment when the signal from the western-most detector has leveled off to its open-aperture value. This detector is defined as detector 1. The other detectors are numbered in a clockwise fashion as viewed from the rear.

The eight multiplexer channels are selected in a sequence that is synchronized with the rotation of the filter wheel. While the 0.5 μ filter is in front of detector 1, the 1.6 μ filter is in front of detector 3. During a 50-ms interval, the difference signals S_λ from detectors 1 and 3 are each sampled 25 times in an interleaved fashion. After a 20-ms pause, the reference signals from detectors 1 and 3 are sampled 25 times each in the same way. While the reference signals are sampled, the filter wheel continues to rotate until the apertures for detectors 1 and 3 are completely closed. After another 20 ms pause, the dark signals S_d from detectors 1 and 3 are sampled in the same manner as S_λ and S_R. By this time the filter wheel has rotated 90°, and the filters are in position in front of detectors 2 and 4. The signals from these detectors are selected in the same sequence as for detectors 1 and 3. When the filter wheel has completed one half cycle, the selection of multiplexer channels begins anew, but the second half cycle begins with the 1.6 μ filter in front of detector 1. One complete

cycle takes 840 ms, after which the timing circuit is reinitialized for the next pass.

The A-to-D is triggered 200 μs after the multiplexer is changed to a new channel, allowing the signal to settle before a conversion commences. The I/O board is the interface between the A-to-D converter and the computer. The result of each conversion is added to the previous contents of the appropriate memory location on the I/O board. After every 18 revolutions of the filter wheel, the computer receives an interrupt signal from the timing circuit causing the data acquisition software to initiate the transfer of data from the I/O board to the hard disk. The I/O board memory is simultaneously cleared, and the data is displayed on the terminal screen. Thus, the computer performs a sequence of reads and writes only once every 15 seconds. Each data record contains the date and local time and a set of 32 integers corresponding to the 32 memory locations on the I/O board. Eight of these channels are inactive, and another eight contain redundant information. This is because the reference and closed-aperture signals are sampled during each half cycle of the filter wheel, and the results stored in separate memory locations. The integer values range from 0 – 450 $\times$ 4095 since each signal is sampled 450 times per integration interval and the output of the 12-bit A-to-D ranges from 0 to 4095. An A-to-D output of 0 corresponds to an input of -10 V, while an output of 4095 corresponds to $+10$ V.

The transfer function from 0 to 80 Hz is shown in figure 2.5. Note that the third zero of the envelope of the transfer function occurs at 60 Hz. Thus, line voltage that is picked up by the signal cables is eliminated in the sampling process. The

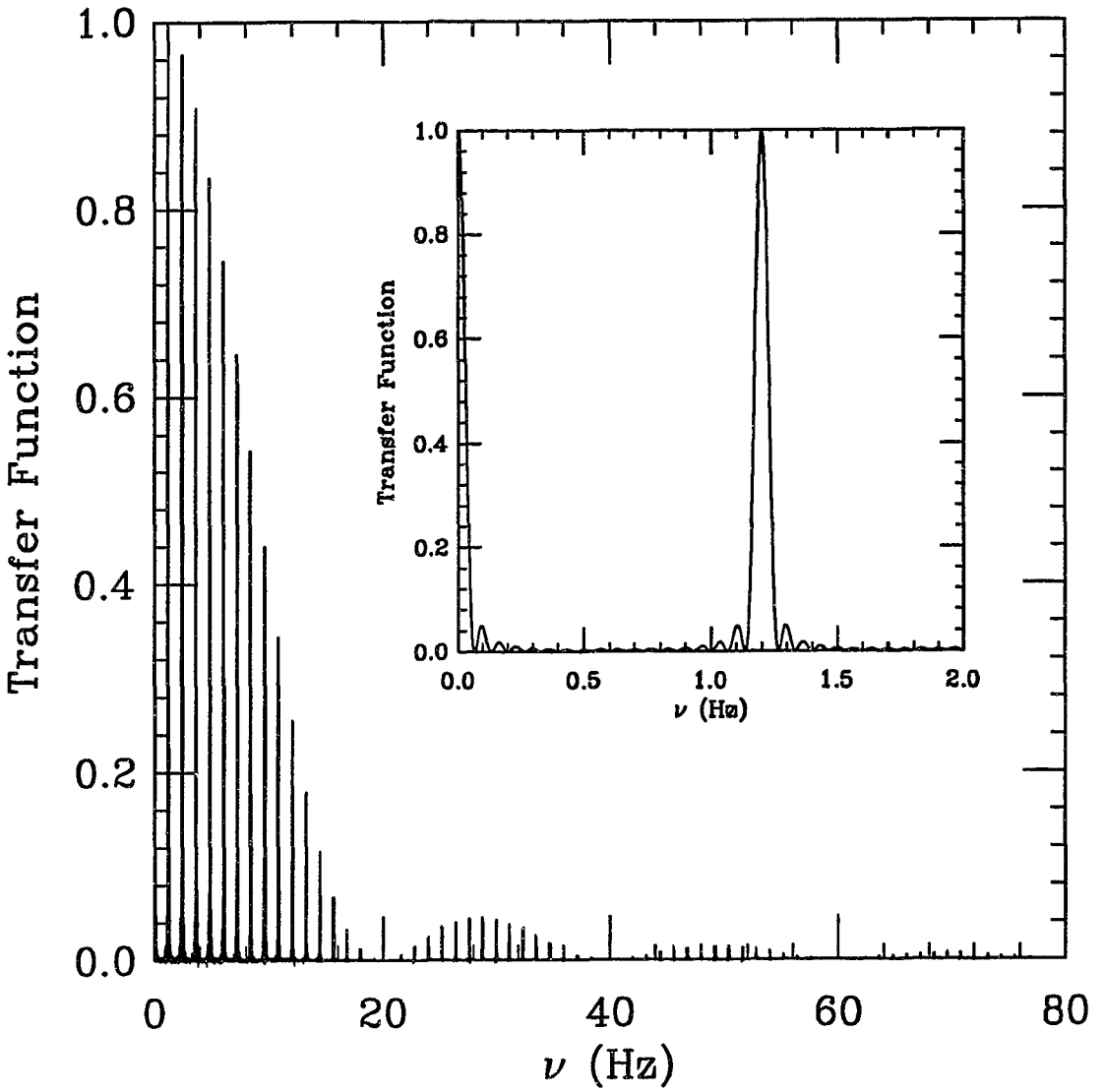

Figure 2.5: Transfer function from 0 to 80 Hz. Peaks occur at harmonics of the 1.2 Hz rotational frequency of the filter wheel. The envelope has zeros at harmonics of 20 Hz.
Inset: Low-frequency region of transfer function.

Nyquist frequency corresponding to a sampling interval of 2 ms is 250 Hz. Power at frequencies near twice the Nyquist frequency will be aliased into the frequency domain of the solar oscillations. The transfer function in the neighborhood of two times the Nyquist frequency is less than 5% of the DC value as a result of the analog filter which has a half-power point of 113 Hz. The closely-spaced peaks in figure 2.5 are at harmonics of the 1.2 Hz rotational frequency of the filter wheel. In the inset, an expanded view of the region from 0 to 2 Hz shows that the first zero occurs at 67 mHz. The frequency domain of the solar oscillations lies below 6 mHz. Therefore, the solar signals are essentially unattenuated by the analog and digital filtering.

2.4 Expected Levels

Assuming perfect blocking of radiation outside the filter passbands, the expected open-aperture output of the circuits in figures 2.2 and 2.3 is

$$S_\lambda = G D_\lambda P_\lambda \Delta\lambda, \tag{2.2}$$

where P_λ is the radiant power density at the wavelength λ incident on the detector, $\Delta\lambda$ is the bandwidth of the filter, D_λ is the detector responsivity in units of volts per watt, and the gain of the system $G = 1824$. The power density and responsivity are taken to be constant over the narrow bandwidth $\Delta\lambda$. The spectral power incident on the detectors is related to the spectral flux $\mathcal{F}_\lambda$ incident on the objective within a

5.2° field of view by

$$P_\lambda = t_l t_f \frac{A_o A_d}{A_s} \mathcal{F}_\lambda, \tag{2.3}$$

where t_f is the passband transmittance of the filter; t_l is the transmittance of the lenses; and A_o, A_d, and A_s are the areas of the objective, the detector, and the illuminated spot in the detector plane, respectively. The numerical value of this combination of areas is 4.72×10^{-4} m^2, while $t_l = 0.85$ and $t_f = 0.4$. An approximate expression for the incident flux can be obtained by a consideration of radiative transport in the Earth's atmosphere. In the following derivation, reference is made to figure 2.6, which shows an incident beam scattered by an angle ψ into the field of view of the sky monitor.

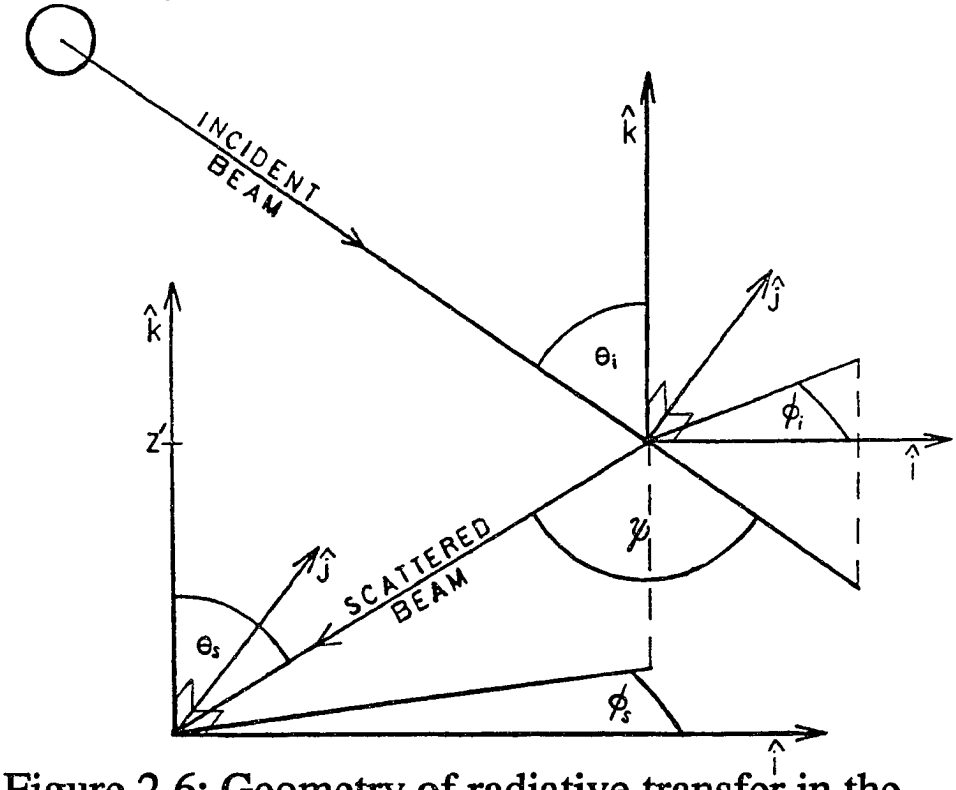

Figure 2.6: Geometry of radiative transfer in the Earth's atmosphere.

The extinction due to scattering into all directions as the incident beam traverses a distance ds at elevation z' along the direction (θ_i, ϕ_i) is given by the equation of transfer

$$d\mathcal{I}_\lambda(z', \theta_i, \phi_i) = -\mathcal{I}_\lambda(z', \theta_i, \phi_i)\kappa_\lambda \rho \, ds \tag{2.4}$$

where κ_λ is the mass scattering coefficient and ρ is the air density. For a plane-parallel atmosphere, the intensity transmitted to elevation z is

$$\mathcal{I}_\lambda(z, \theta_i, \phi_i) = \mathcal{I}_\lambda(z_{max}, \theta_i, \phi_i) \exp\left(\int_{z_{max}}^{z} \kappa_\lambda \rho \frac{dz'}{\cos\theta_i}\right), \tag{2.5}$$

where the elevation z_{max} corresponds to the top of the atmosphere. The intensity Rayleigh scattered into the field of view of the sky monitor at elevation z is

$$\mathcal{I}_\lambda(z, \theta_s, \phi_s) = \frac{3}{16\pi}(1 + \cos^2\psi)\kappa_\lambda \rho \mathcal{I}_\lambda(z, \theta_i, \phi_i) \tag{2.6}$$

(Chandrasekhar 1960), where θ_s and ϕ_s define the direction of the scattered beam. The equation of transfer may be integrated from elevation z to the ground along the (θ_s, ϕ_s) direction to obtain the intensity transmitted to the ground due to scattering through angle ψ at elevation z. Integrating the result over z gives the total intensity at ground level due to scattering at all elevations,

$$\mathcal{I}_\lambda(0, \theta_s, \phi_s) = \int_0^{z_{max}} \mathcal{I}_\lambda(z, \theta_s, \phi_s) \exp\left(\int_z^0 \kappa_\lambda \rho \frac{dz'}{\cos\theta_s}\right) dz. \tag{2.7}$$

Combining equations (2.5), (2.6), and (2.7), and assuming an isothermal atmosphere, one obtains

$$\begin{aligned} \mathcal{I}_\lambda(0,\theta_s,\phi_s) &= \frac{3}{16\pi}(1+\cos^2\psi)\frac{\cos\theta_i}{\cos\theta_i-\cos\theta_s} \\ &\times \left[\exp\left(\frac{-\kappa_\lambda\rho_o H}{\cos\theta_i}\right)-\exp\left(\frac{-\kappa_\lambda\rho_o H}{\cos\theta_s}\right)\right] \\ &\times \mathcal{I}_\lambda(z_{max},\theta_i,\phi_i) \end{aligned} \tag{2.8}$$

where H is the density scale height.

The opacity $\kappa_\lambda\rho_o$ at ground level is $\simeq 32\pi^3(n-1)^2/(3N_o\lambda^4)$ (Jackson 1975), where n is the index of refraction at the surface and N_o is the surface number density of air. One finds that $\kappa_\lambda\rho_o H \simeq 0.12$ at $\lambda = 0.5\ \mu$, and $\kappa_\lambda\rho_o H \simeq 1.11\times10^{-3}$ at $\lambda = 1.6\ \mu$. Thus, the exponentials in equation (2.8) may be expanded to first order with a maximum error of 3.4% at 0.5 μ. At midday, $\phi_i = 0$ so that $\cos\psi = \cos\theta_i\cos\theta_s$. An upper limit on the flux is obtained by setting $\cos\theta_i = 1$. Integrating over a 5.2° field of view centered on the optical axis of the telescope, one obtains for the spectral flux

$$\mathcal{F}_\lambda = (3.56\times10^{-4})\kappa_\lambda\rho_o H\Upsilon\pi B_\lambda(T), \tag{2.9}$$

where $\mathcal{I}_\lambda(z_{max},\theta_i,\phi_i)$ has been replaced by the Planck function $B_\lambda(T)$ times $\Upsilon\pi$ (Mihalas 1978), $\Upsilon = 7.6\times10^{-5}$ sr is the angular size of the solar disk, and $T = 5777$ K is the surface temperature of the Sun. Computing the flux from equation (2.9) and substituting into equation (2.3) for the spectral power yields $P_{0.5} = 4.4\times10^{-5}$ W/μ and $P_{1.6} = 4.6\times10^{-8}$ W/μ.

The detector responsivity D_λ appearing in equation (2.2) is a function of the circuit configuration. Taking the typical noontime signal $S_{0.5} \simeq 5$ V and using the above estimate of power density, the responsivity at 0.5 μ is found to be about 7×10^3 V/W. Both types of detectors are more sensitive in the infrared than in the visible. Typical responsivity curves provided by the manufacturers indicate that the PbS detectors are twice as sensitive at 1.6 μ, while the Ge detectors are about 14 times more sensitive at this wavelength than at 0.5 μ. Scaling D_λ by these ratios and substituting into equation (2.2), the expected 1.6 μ signals $S_{1.6}$ are found to be 0.27 V and 38 mV for the Ge and PbS detectors, respectively.

Corrections to the expected levels due to the finite transmittance in the stopband of the filters may be determined by evaluating the integral

$$\begin{aligned} S_L &= G\int_0^\infty D_\lambda P_\lambda \, d\lambda \\ &= \alpha \int_0^\infty D_\lambda B_\lambda(T)\lambda^{-4} \, d\lambda. \end{aligned} \tag{2.10}$$

The subscript L indicates that this signal is due to leakage in the stopband. In this case, the transmittance of the filter $t_f = 10^{-4}$. All numerical coefficients have been absorbed into the factor α. To a first approximation, the responsivity is assumed to be a linear function of wavelength up to the long-wavelength cutoff. Approximating the Planck function at $T = 5777$ K by

$$B_\lambda \simeq 2hc^2\lambda^{-5}\left[\exp(-2.5/\lambda) + \exp(-5.0/\lambda)\right] \tag{2.11}$$

introduces a maximum error of $\sim 5\%$ at 1.6 μ. Repeated integration by parts yields

S_L = 45 mV for the PbS detectors and S_L = 64 mV for the Ge detectors. Thus, leakage in the stopband more than doubles the estimated PbS signal at 1.6 μ and increases the Ge signal at 1.6 μ by about 24%. The contribution of leakage to the 0.5 μ signals is 0.9% and 1.3% for the PbS and Ge detectors, respectively.

The foregoing calculations have presupposed that the atmosphere is clean and dry so that only Rayleigh scattering need be considered. In practice, nonselective, or *Mie* scattering due to atmospheric aerosols will contribute to the observed radiation flux. The distribution of atmospheric aerosols is highly variable in both time and space making the contribution of Mie scattering difficult to predict. A crude estimate of the ratio of the 1.6 μ signal to the 0.5 μ signal due to Mie scattering may be obtained by multiplying the ratio for Rayleigh scattering by $(1.6/0.5)^4$. Ratios for the two types of scattering and for both types of detectors are presented in table 2.2.

TABLE 2.2

Ratio of 1.6 μ to 0.5 μ Signals

Detector	Scattering	$S_{1.6}/S_{0.5}$
PbS	Rayleigh	0.017
PbS	Mie	1.8
Ge	Rayleigh	0.067
Ge	Mie	7.0

Chapter 3

Data Reduction

3.1 Data Acquisition & Preprocessing

Data were collected on 216 days spanning 15.5 months from April 1, 1991 to July 15, 1992. The closed-aperture signals were subtracted from the open-aperture signals yielding quantities proportional to the spectral flux, and the redundant measurements of the reference signals were averaged. Wild points, or *glitches* were next removed from the time series (Otnes and Enochson 1978). Such glitches are introduced into the data either through the passage of clouds through the field of view or by spikes in the power supply voltage, and may lie five or more standard deviations from the local mean. They were edited out by means of an interactive software package which allowed these points to be visually identified and flagged. The flagged points were ignored in the curve fitting procedure described below, and were ultimately replaced

by zeros prior to computation of the discrete Fourier transform.

Examples of daily time strings are shown in figures 3.1 – 3.5. The abscissas are local time in seconds. The striking difference between the Ge and PbS signals in the visible results from the strong temperature dependence of the PbS responsivity. This is apparent from the similarity between figure 3.3 and the reference signal in figure 3.5, which is primarily a function of the temperature. The decrease of PbS detection sensitivity with temperature is less apparent in the infrared due to the increasing contribution of Mie scattering toward midday. Evidence of variations in the atmospheric aerosol concentration is found in the relatively temperature-insensitive Ge infrared signal. The observed ratios between the 1.6 and 0.5 μ signals suggest that about 2% of the visible signal is due to Mie scattering.

3.2 Calibration

The general relationship between the output signals and the radiant flux may be expressed as

$$S_\lambda - S_d = C(T)\mathcal{F}_\lambda^{\eta(T)}, \tag{3.1}$$

where the coefficient $C(T)$ and exponent $\eta(T)$ are functions of the temperature as in equation (2.1). Calibration data was obtained in order to determine the exponent $\eta(T)$. The objective was stopped down in increments of one-fifth of the objective area over a period of about five minutes. The temperature of the detectors and the brightness of the sky were assumed to remain constant for the duration of the calibra-

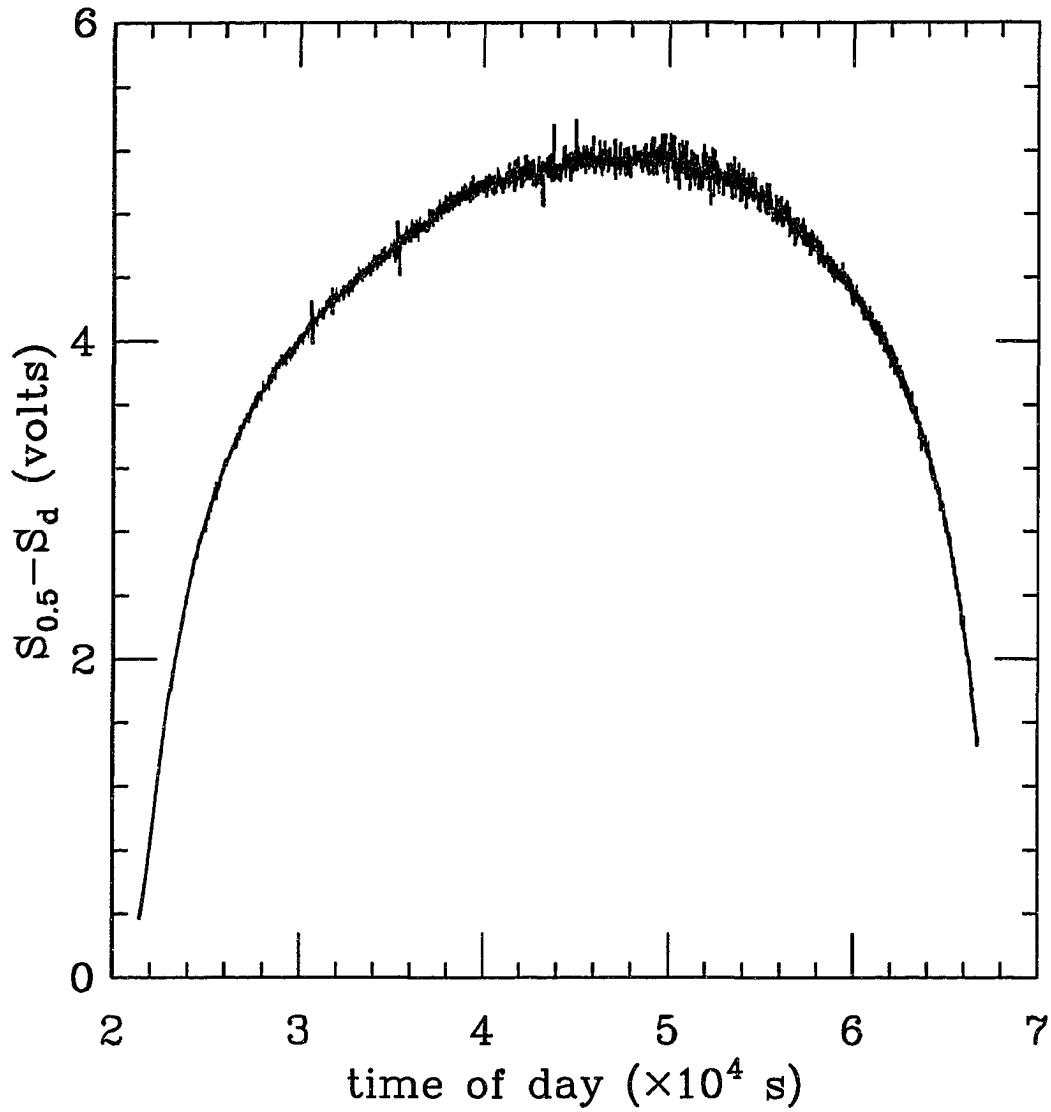

Figure 3.1: Daily time series obtained April 14, 1991 at 0.5 microns with Ge detector #1.

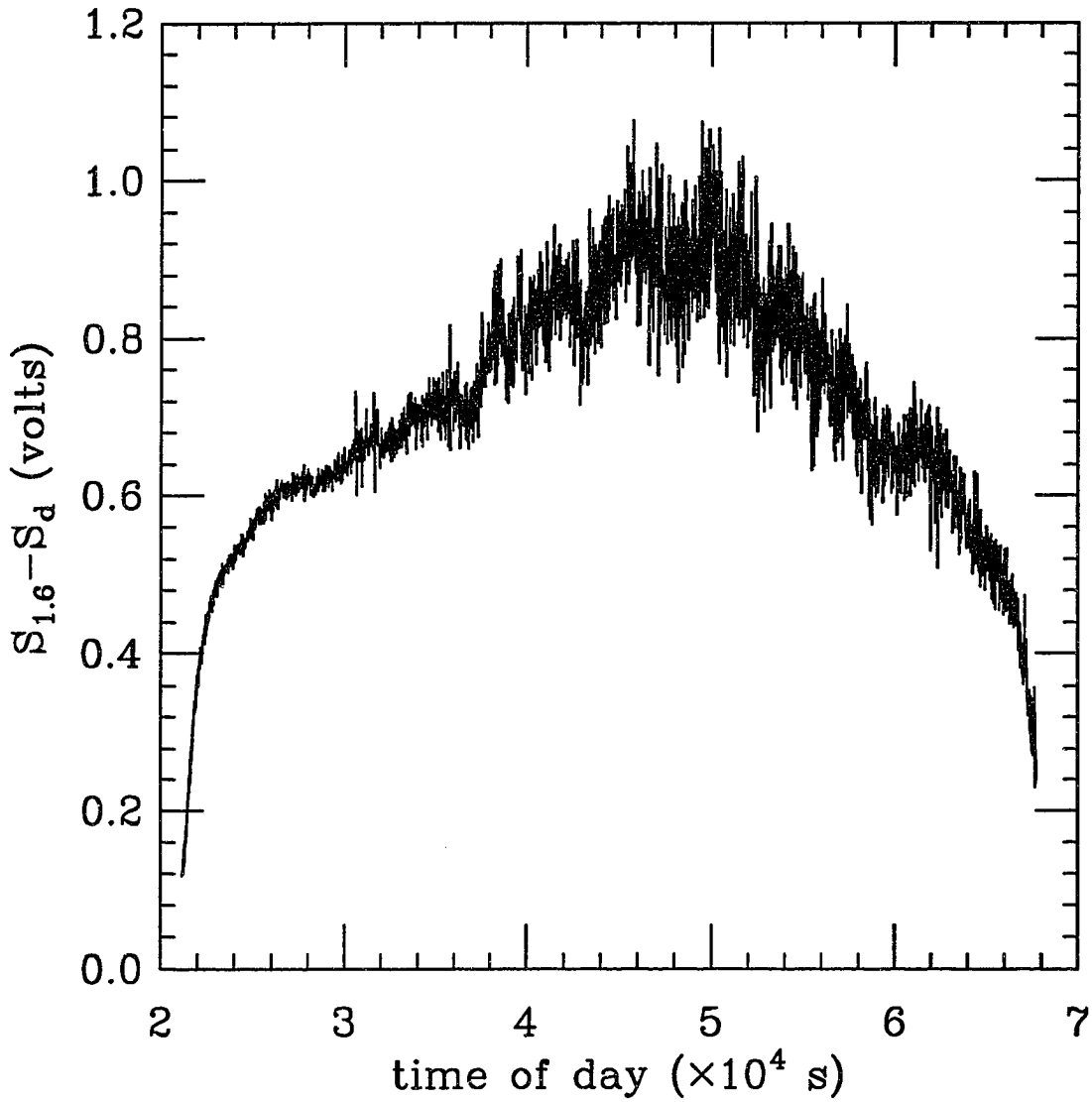

Figure 3.2: Daily time series obtained April 14, 1991 at 1.6 microns with Ge detector #1.

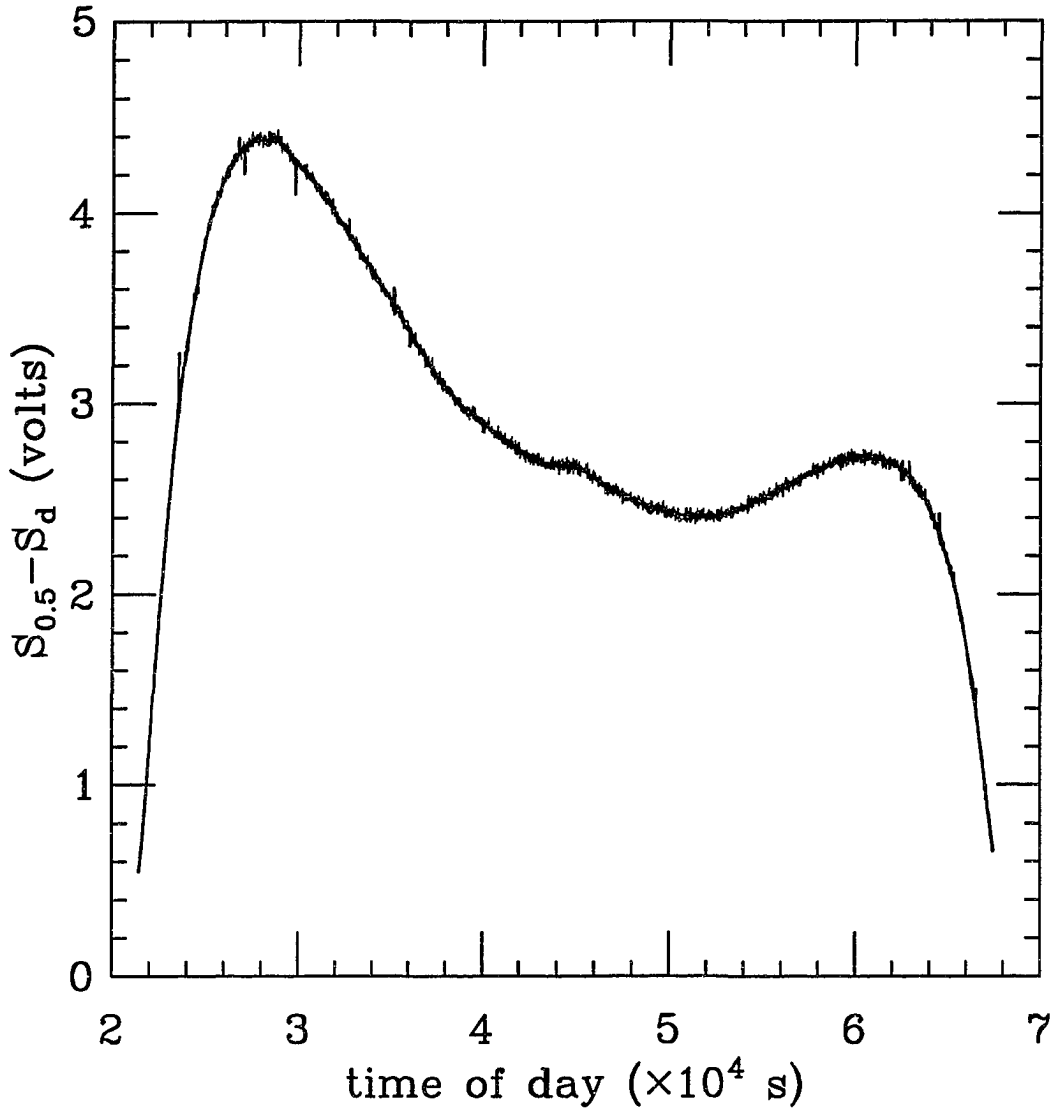

Figure 3.3: Daily time series obtained April 14, 1991 at 0.5 microns with PbS detector #2.

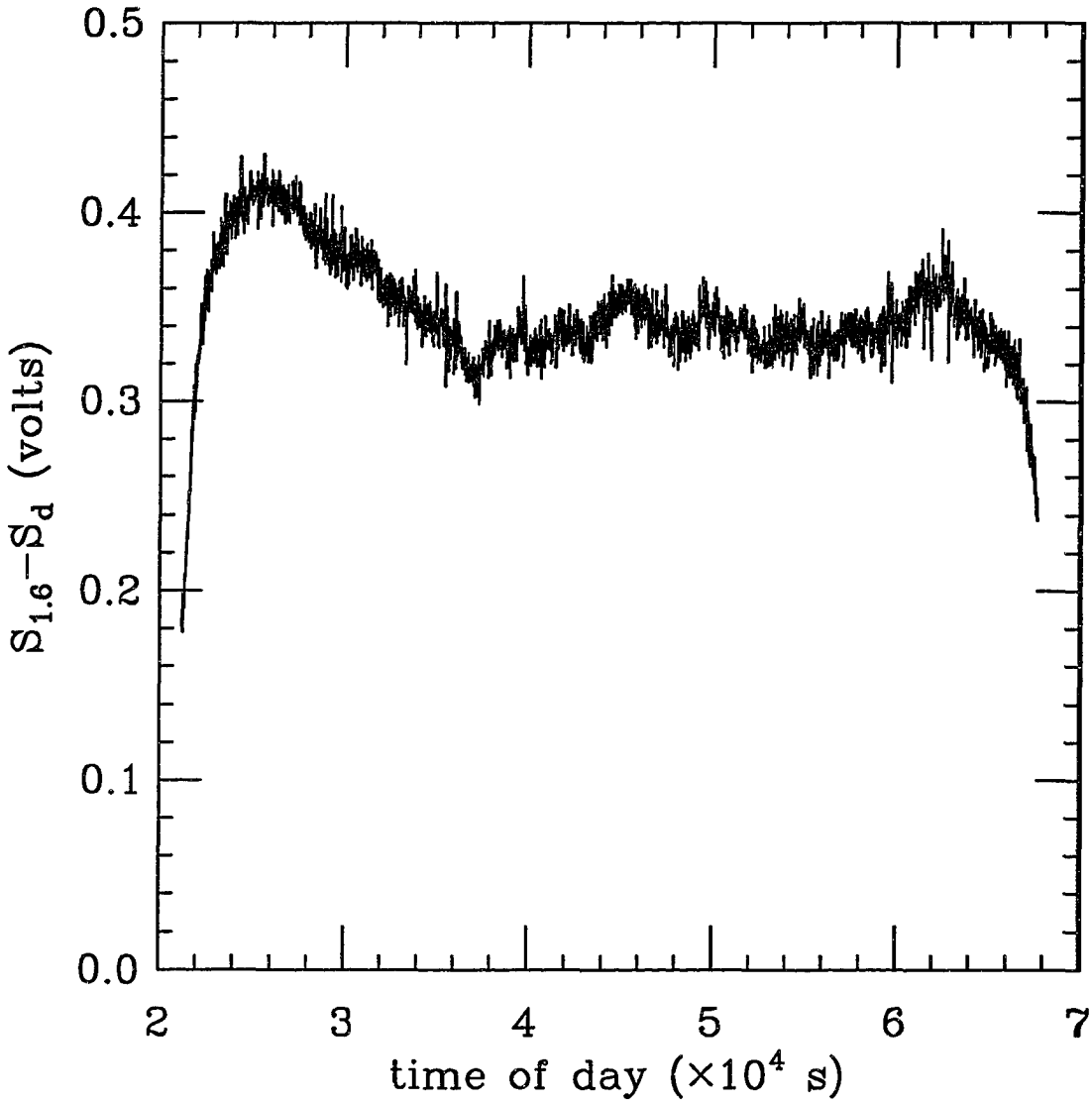

Figure 3.4: Daily time series obtained April 14, 1991 at 1.6 microns with PbS detector #2.

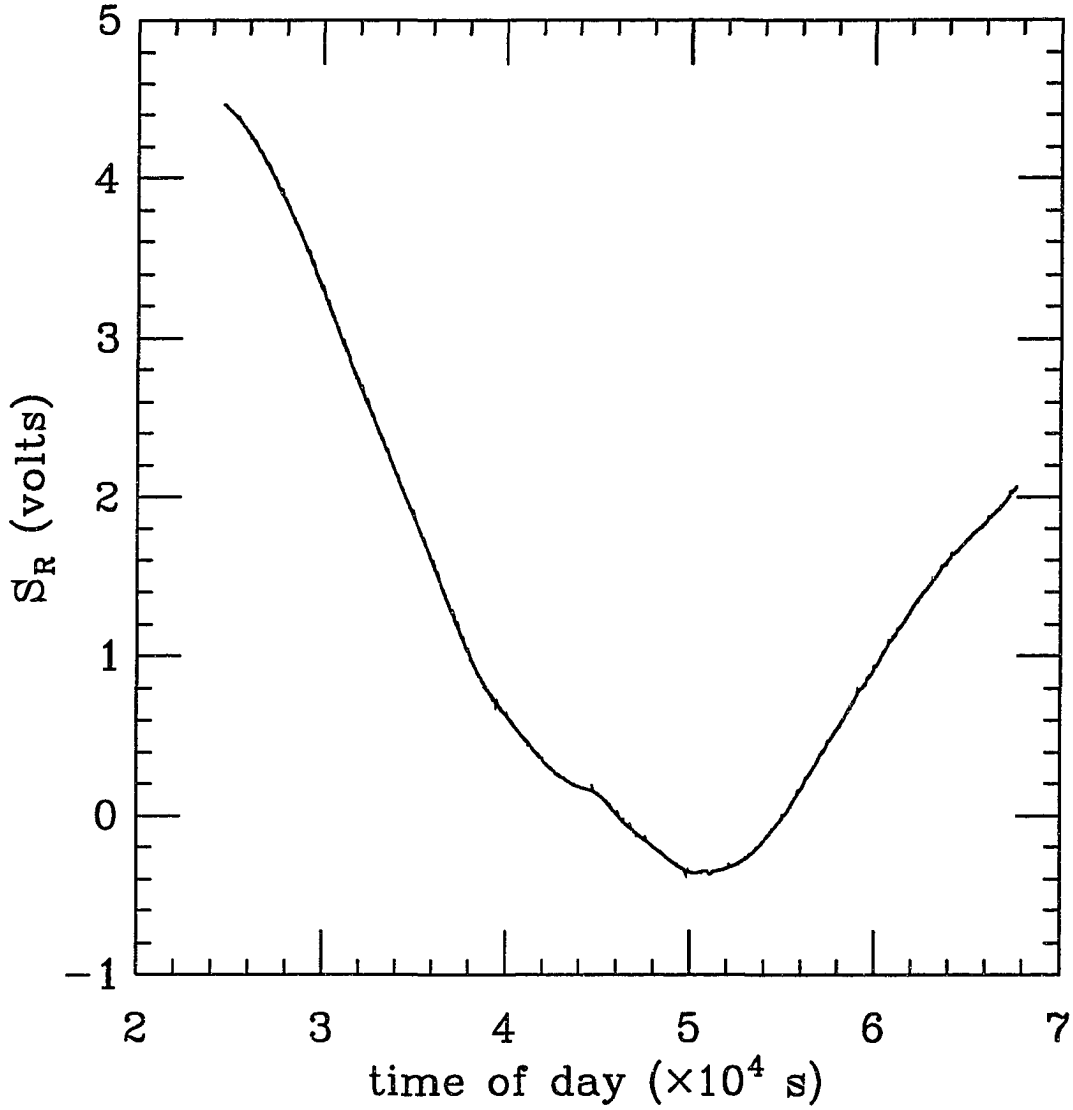

Figure 3.5: Reference signal obtained April 14, 1991 with PbS detector #2.

tion run. A plot of $\log(S_\lambda - S_d)$ versus $\log(f)$, where f is the fraction of the exposed objective area, yields the exponent $\eta(T)$ at the fixed temperature T. This exercise was repeated at several different temperatures with the results shown in figures 3.6 and 3.7. The reciprocal of the reference signal from PbS detector 2, a monotonically increasing function of temperature, is used as the abscissa in both figures. The exponents are seen to be strongly wavelength dependent. Both types of detectors exhibit a drop in sensitivity to infrared radiation with increasing temperature. The PbS detectors show a more modest decrease in sensitivity with temperature in the visible, while the sensitivity of the Ge detectors to visible light does not appear to vary strongly with temperature. The Ge detectors displayed much greater variability between cells than did the PbS detectors. Average values of the exponent $\overline{\eta}$ are given for the four detectors in table 3.1.

TABLE 3.1
Average Detector Response

Detector	Type	λ (μ)	$\overline{\eta}$
1	Ge	0.5	0.470
1	Ge	1.6	0.842
2	PbS	0.5	0.782
2	PbS	1.6	0.471
3	Ge	0.5	0.982
3	Ge	1.6	0.838
4	PbS	0.5	0.797
4	PbS	1.6	0.496

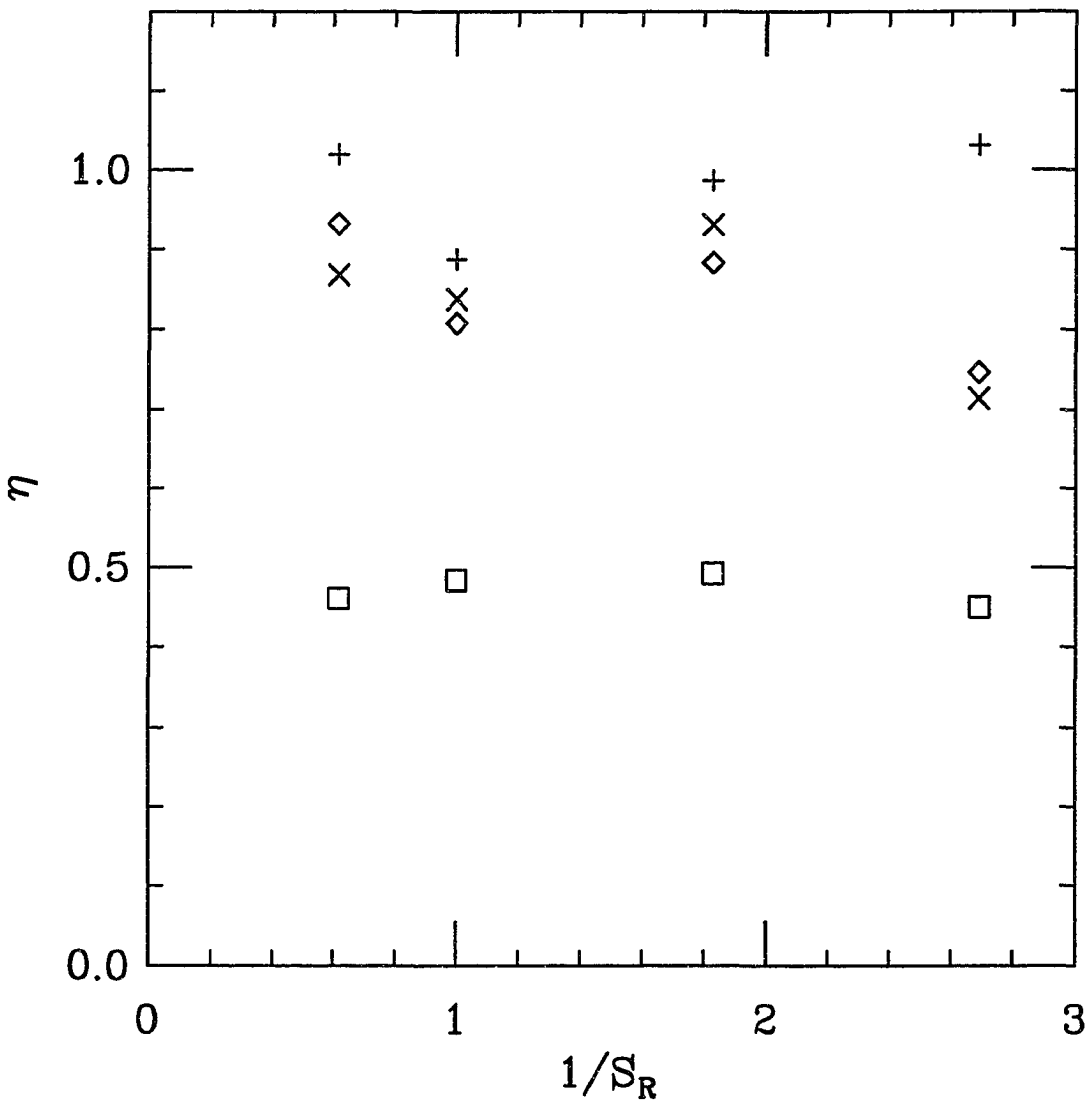

Figure 3.6: Ge response as a function of $1/S_R$.
Square - detector #1 at 0.5 μ.
Diamond - detector #1 at 1.6 μ.
Plus - detector #3 at 0.5 μ.
Cross - detector #3 at 1.6 μ.

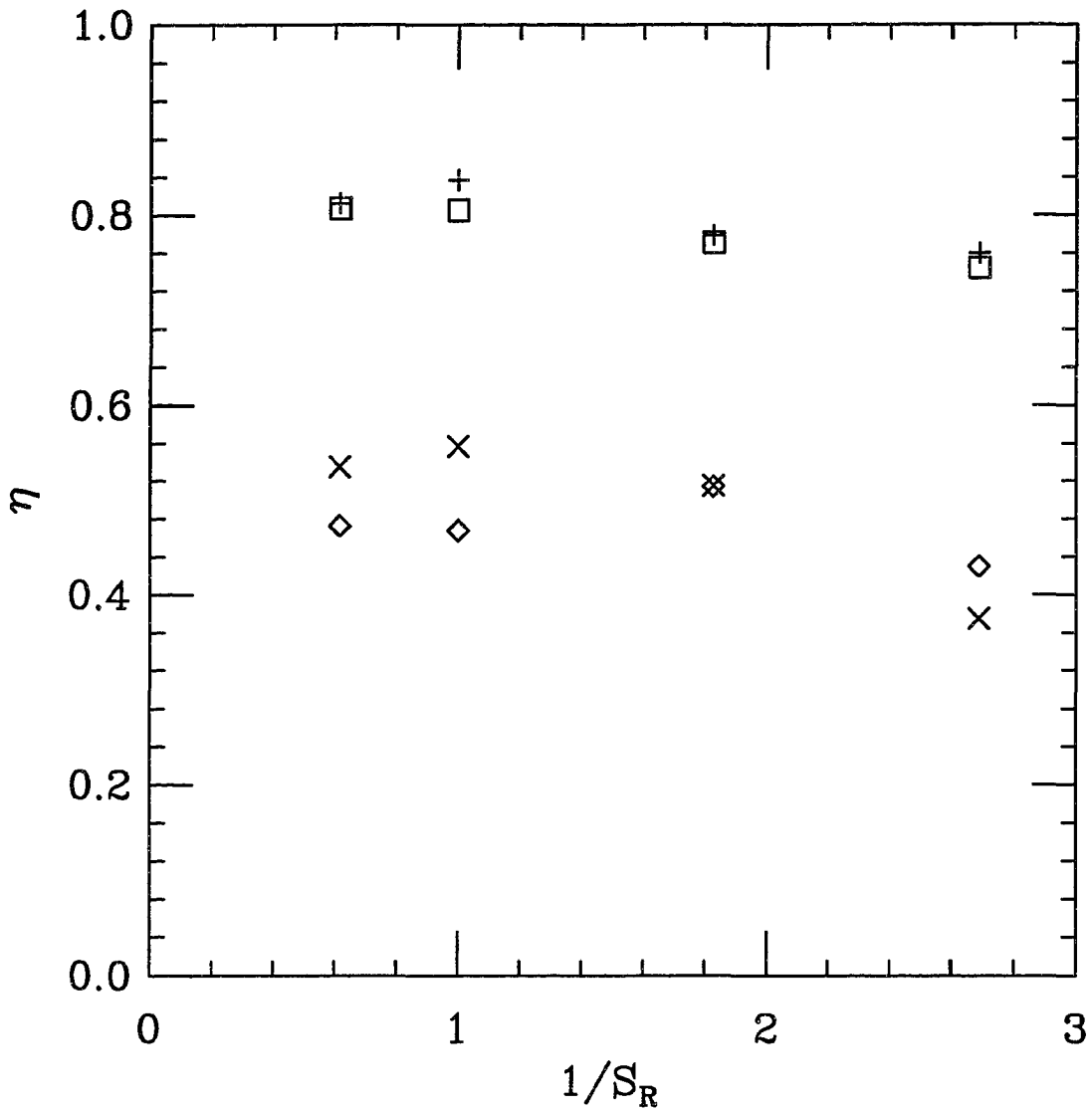

Figure 3.7: PbS response as a function of $1/S_R$.
Square - detector #2 at 0.5 μ.
Diamond - detector #2 at 1.6 μ.
Plus - detector #4 at 0.5 μ.
Cross - detector #4 at 1.6 μ.

3.3 Theoretical Flux Variation

The signals displayed in figures 3.1 – 3.4 are dominated by the diurnal variations in temperature and radiant flux due to the Earth's rotation. To prevent these effects from dominating the power spectrum, these trends must be removed prior to the computation of the FFT. The PbS reference signals provide the needed temperature information. To obtain the theoretical time variation of the flux due to Rayleigh scattering, the calculation of § 2.4 for a plane-parallel atmosphere is extended to the spherical case with the origin of coordinates at the center of the Earth. The angles θ_i and θ_s used in equations (2.5) – (2.8) must now be measured with respect to the position vector **r** and obey the relation

$$r n_r \sin\theta = \text{constant} \tag{3.2}$$

(Born and Wolf 1959), where n_r is the index of refraction at the radius r. For the incident beam, the constant is taken as $r_o \sin\theta_o$, where the subscript refers to the top of the atmosphere. For the scattered beam the constant is $R n_R \sin\theta_d$, where R is the radius of the Earth, n_R is the index of refraction at the surface, and θ_d is the angle between the optical axis of the telescope and the zenith.

Figure 3.8 shows the projection onto a plane of an incident ray that is refracted as it propagates through the Earth's atmosphere. The angle between the line connecting the Earth and Sun and the position vector which locates the sky monitor is defined as the zenith angle Φ. The spherical-polar analog of equation (2.5) for the intensity

transmitted to elevation r in a beam which is at angle θ_o to the position vector $\mathbf{r}$ at the top of the atmosphere is

$$\mathcal{I}_\lambda(r,\theta_o) = \mathcal{I}_\lambda(r_o,\theta_o)\exp\left(\int_{r_o}^{r} \frac{\kappa_\lambda \rho r' n_{r'}\, dr'}{\sqrt{(r'n_{r'})^2 - (r_o \sin\theta_o)^2}}\right). \tag{3.3}$$

The time dependence is embedded in the angle θ_o, which is related to the zenith angle Φ through the integral equation

$$\Phi = \theta_o + \int_{r}^{r_o} \frac{r_o \sin\theta_o\, dr'}{r'\sqrt{(r'n_{r'})^2 - (r_o \sin\theta_o)^2}}. \tag{3.4}$$

The zenith angle Φ is in turn related to the time t through

$$\cos\Phi = \cos\zeta\cos\xi\cos(\Omega(t-t_r)) + \sin\zeta\sin\xi, \tag{3.5}$$

where ζ represents the declination, ξ represents the geographic lattitude, Ω is the rotational frequency of the Earth, and t_r is the time of transit. For given Φ and r, equation (3.4) was solved for θ_o by iteration using $\theta_o = \arcsin(r\sin\Phi/r_o)$ as the initial guess.

Equation (3.3) is strictly valid only for $\Phi \leq \pi/2$. When $\Phi > \pi/2$ there will be a point of closest approach r_{min}, at which $\theta_i = \pi/2$ and beyond which the incident beam is travelling away from the surface. This situation is represented in figure 3.9.

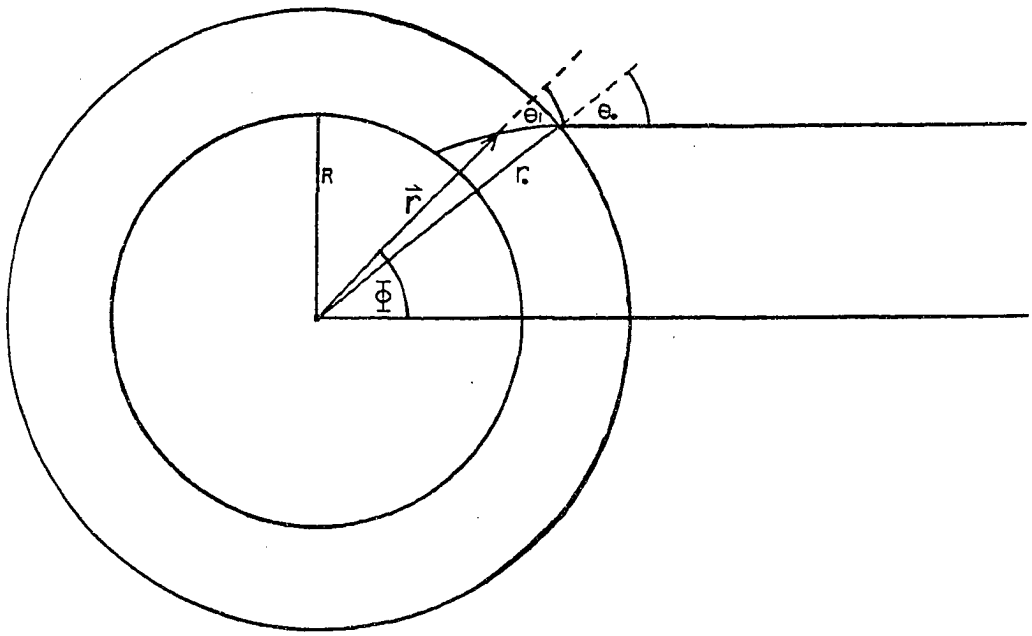

Figure 3.8: Geometry used in radiative transfer calculations for the case $\Phi \leq \pi/2$.

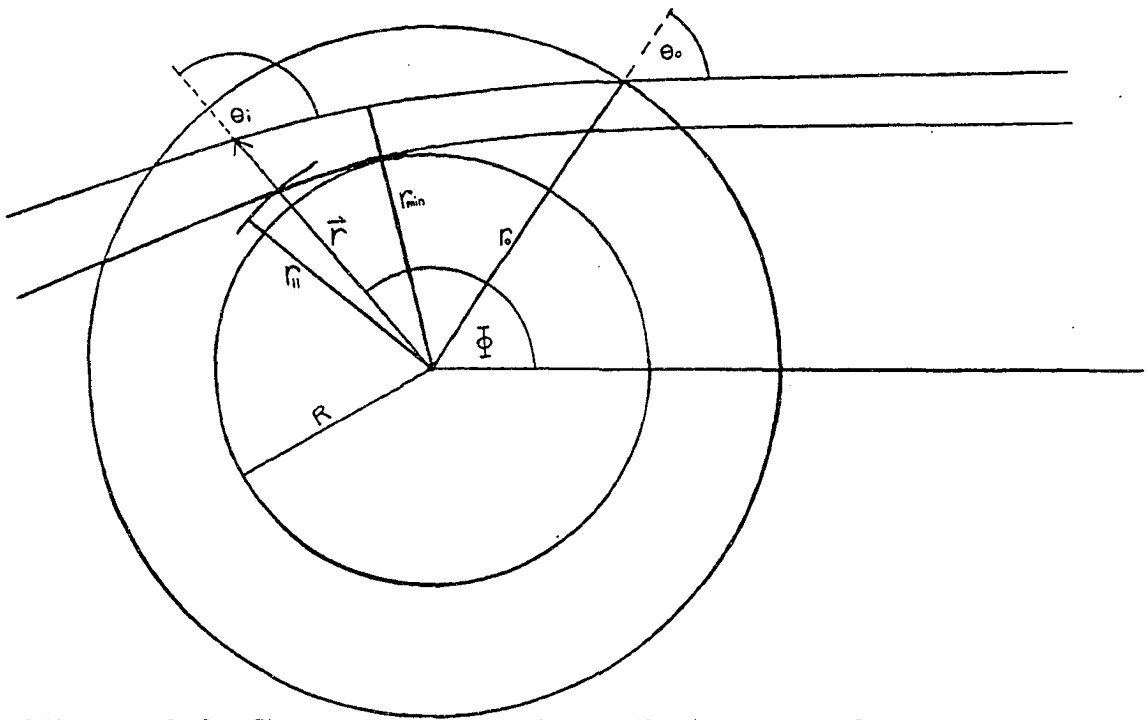

Figure 3.9: Geometry used in radiative transfer calculations for the case $\Phi > \pi/2$.

In this case, equation (3.3) becomes

$$\mathcal{I}_\lambda(r,\theta_o) = \mathcal{I}_\lambda(r_o,\theta_o)\exp\left(\int_{r_o}^{r_{min}} \frac{\kappa_\lambda \rho r' n_{r'}\, dr'}{\sqrt{(r'n_{r'})^2 - (r_o \sin\theta_o)^2}}\right) \times \exp\left(-\int_{r_{min}}^{r} \frac{\kappa_\lambda \rho r' n_{r'}\, dr'}{\sqrt{(r'n_{r'})^2 - (r_o \sin\theta_o)^2}}\right), \quad (3.6)$$

where r_{min} is obtained from the condition $r_{min} n_{r_{min}} = r_o \sin\theta_o$. The spherical-polar analog of equation (2.7) for the total intensity transmitted to the ground due to Rayleigh scattering at all elevations into the field of view of the sky monitor is

$$\mathcal{I}_\lambda(0,\theta_d) = \frac{3}{16\pi}(1+\cos^2\psi)\int_R^{r_o} \kappa_\lambda \rho \mathcal{I}_\lambda(r,\theta_o)\exp\left(\int_r^R \frac{\kappa_\lambda \rho r'\, dr'}{\sqrt{(r')^2 - (R\sin\theta_d)^2}}\right) dr. \quad (3.7)$$

Once again, this equation is strictly valid only for $\Phi \leq \pi/2$. As Φ increases beyond $\pi/2$, the observation point is soon cast in shadows and the lower limit becomes greater than R. It is observed that $\Phi - \theta_i = 35.4'$ at sea level when $\Phi = 90°$ (Allen 1973). Utilizing this information, the correct lower limit in equation (3.7) for the case $\Phi > \pi/2$ is obtained from an equation similar to equation (3.4):

$$\Phi = 90°35.4' + \int_R^{r_{ll}} \frac{R n_R\, dr}{r\sqrt{(r n_r)^2 - (R n_R)^2}}, \quad (3.8)$$

where r_{ll} is the desired lower limit. This equation is solved by an iterative procedure beginning with an initial guess of $r_{ll} = R/\cos(\Phi - 90°35.4')$. Corrections appear as a series of terms in the argument of the cosine.

To obtain the flux from equation (3.7), $(1 + \cos^2\psi)$ is integrated over the field of view of the sky monitor, and $\mathcal{I}_\lambda(r_o,\theta_o)$ is replaced by $\pi\Upsilon B_\lambda$ as before. The results of numerical integration of equations (3.3) and (3.7) are shown in figures 3.10 and 3.11.

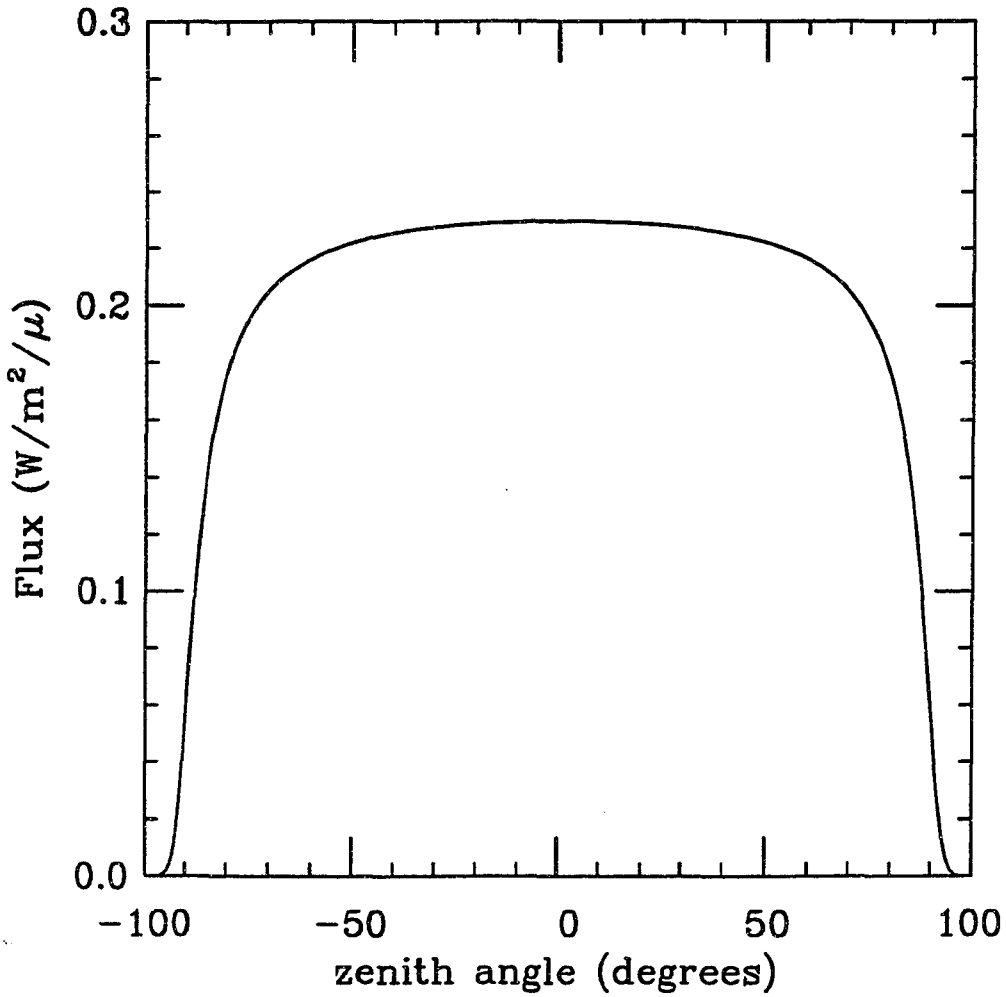

Figure 3.10: Theoretical spectral flux at 0.5 μ within field of view of the sky monitor.

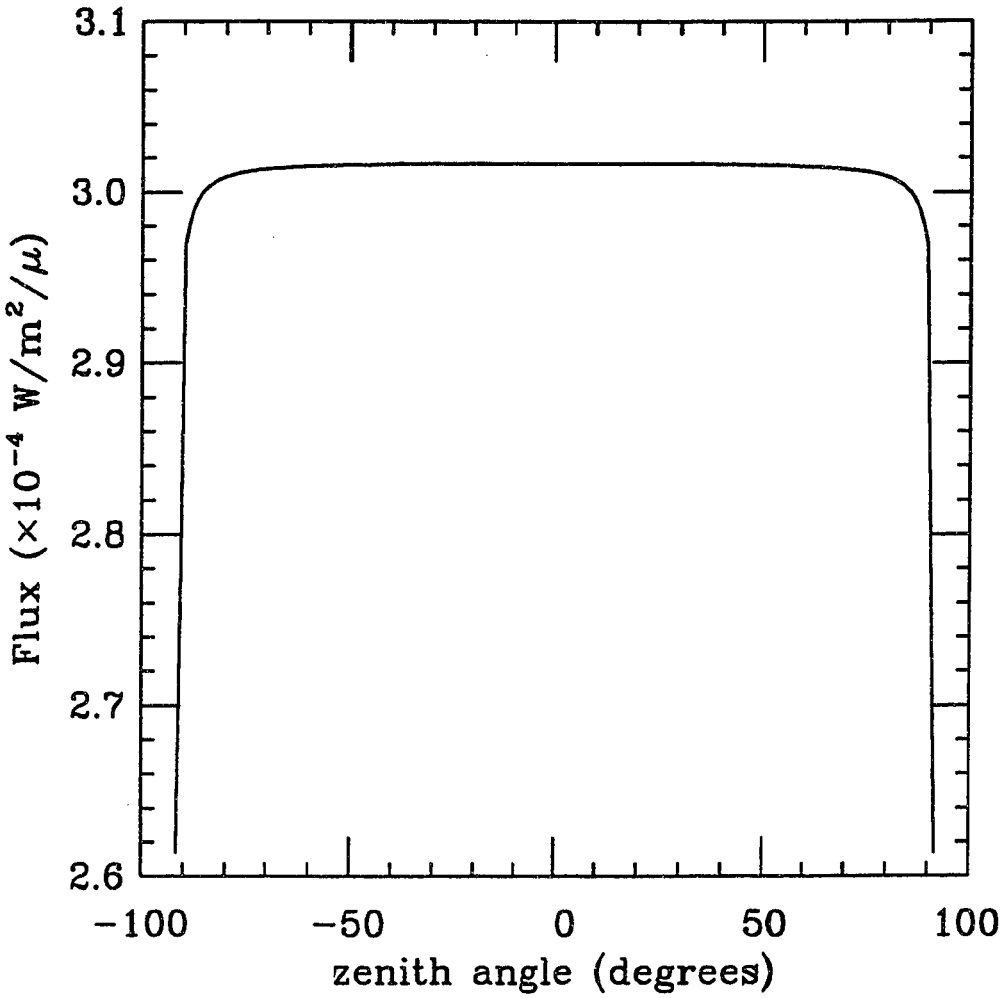

Figure 3.11: Theoretical spectral flux at 1.6 μ within field of view of the sky monitor.

The values at $\Phi = 0$ are in good agreement with the upper limits found in the previous chapter. The flux is seen to be nearly constant in the infrared for $\mid \Phi \mid \lesssim 85°$ and in the visible for $\mid \Phi \mid \lesssim 70°$. The spectral flux at 0.5 μ has been plotted out to $\pm 100°$ and is seen to go smoothly to zero at about $\Phi = 97°$.

3.4 Trend Removal

In removing the diurnal trends by least-squares fitting, care must be taken not to remove the solar signals that one is searching for. This could occur if the time strings to be fit are too short or if too many free parameters are allowed. The longest-period solar normal modes have periods of about four hours. Thus, the daily time strings were divided into four-hour segments with a minimum of overlap. In keeping with common practice, only data for which $\mid \Phi \mid < 70°$ was used in this analysis. Future work may include zenith angles $\gtrsim 90°$. The strings were decimated by replacing every 11 points by their mean. This was necessary to limit the amount of computing time required. Least-squares fits were obtained for each four-hour segment and were smoothly joined in the overlap regions. The time strings were parametrized using the time t, the PbS reference signal S_R, and the radiant flux due to Rayleigh scattering $\mathcal{F}_{R\lambda}$. The contribution to the flux due to Rayleigh scattering has been modeled in the previous section. The parametrization of the time strings is complicated, however, by the contribution due to Mie scattering. The best set of parameters was found to depend on the detector and the wavelength, and to vary from day to day. Therefore,

the parametrization of each four-hour segment of data was tailored to achieve the best least-squares fit. In each case, a linear combination of three or more of the following parameters, plus a constant term, was used:

1) t	2) t^2	3) S_R	4) S_R^2
5) $t\mathcal{F}_{R\lambda}^{\overline{\eta}}$	6) $t^2\mathcal{F}_{R\lambda}^{\overline{\eta}}$	7) $S_R\mathcal{F}_{R\lambda}^{\overline{\eta}}$	8) $S_R^2\mathcal{F}_{R\lambda}^{\overline{\eta}}$
9) $\mathcal{F}_{R\lambda}^{\overline{\eta}}$	10) $S_R\mathcal{F}_{R\lambda}^{\overline{\eta}}\log\mathcal{F}_{R\lambda}$	11) $S_R^2\mathcal{F}_{R\lambda}^{\overline{\eta}}\log\mathcal{F}_{R\lambda}$	

The terms involving $\log\mathcal{F}_{R\lambda}$ allow for temperature-dependent corrections to the exponent $\overline{\eta}$. Additional terms beyond three were included if the additional term reduced χ^2 by at least 5%. The maximum number of terms allowed in a given fit was six.

These fits were then used to normalize the daily time strings. Writing the flux in terms of the background flux $\mathcal{F}_{o\lambda}$, a noise term $\mathcal{F}_{N\lambda}$, plus a sum of perturbations due to solar oscillations, equation (3.1) may be expanded as

$$S_\lambda - S_d = C\mathcal{F}_{o\lambda}^{\eta}\left(1+\eta\frac{\sum_i \mathcal{F}'_{i\lambda}+\mathcal{F}_{N\lambda}}{\mathcal{F}_{o\lambda}}\right), \tag{3.9}$$

where $\mathcal{F}'_{i\lambda}$ is the Eulerian perturbation to the flux due to the ith mode of oscillation. Dividing by the fit and subtracting one from each side, this becomes

$$\mathcal{S}_\lambda = \eta\frac{\sum_i \mathcal{I}'_{i\lambda}+\mathcal{I}_{N\lambda}}{\mathcal{I}_{o\lambda}}, \tag{3.10}$$

where the proportionality between intensity and flux has been employed. The unitless quantity $\mathcal{S}_\lambda$ is the normalized signal less one, and $\mathcal{I}_{o\lambda}$, $\mathcal{I}'_{i\lambda}$ and $\mathcal{I}_{N\lambda}$ are defined analagously to $\mathcal{F}_{o\lambda}$, $\mathcal{F}'_{i\lambda}$ and $\mathcal{F}_{N\lambda}$.

3.5 Data Rejection

The standard deviation of the mean was chosen as a measure of the quality of a day of data. This quantity reflects the noise level at dc and, in the case of purely white noise, at all other frequencies. Figure 3.12 shows the standard deviation of the mean on 176 days for Ge detector 1 at 0.5 μ. The days have been sorted into the order of increasing standard deviation. Only the 176 best days have been used in the plot. The vertical line indicates the cutoff beyond which the days were rejected. The position of the cutoff was chosen somewhat subjectively. As discussed in § 1.6, the duty cycle of a data set determines the overall statistical stability of a power spectrum. Thus, while a given day may increase the noise power in the spectrum, its omission may cause the redistribution of signal power away from the central peak. Either effect results in a lower signal-to-noise ratio. Therefore, the effect on the window function of omitting particular days was considered in choosing the position of the cutoff in figure 3.12. When a day was rejected based on the standard deviation of the signal from one detector, the data from the other three detectors were rejected as well. Thus, a small number of days falling below the cutoff in figure 3.12 was also omitted. Approximately 20% of the data was rejected by this method.

At this point it is possible to make a preliminary estimate of the signal-to-noise ratio. From figure 3.12 and the discussion above, the noise amplitude per frequency bin for a white noise source is of the order of 10^{-3} for one day of data. Taking 10^{-6} as an estimate of the expected fractional intensity variation due to a solar mode of

oscillation, one would predict a signal-to-noise power ratio per mode per day of 10^{-3} in amplitude, or 10^{-6} in power. It must be emphasized, however, that the noise power is in general not uniformly distributed in frequency. It will be seen in the next chapter that the noise power is concentrated at low frequencies making this preliminary estimate overly pessimistic. Moreover, the signal-to-noise ratio will be improved by an increase of resolution beyond that obtained from a single day of data as mentioned at the end of § 1.7. For M days of data, both the signal power and the noise power are increased by the factor M. The noise power is distributed among τf_N independent frequency bins where f_N is the Nyquist frequency and τ is the total time spanned by the data. In the case of white noise, the noise power is divided evenly among the available frequency bins. On the other hand, power due to a signal with a lifetime $\gtrsim \tau$ will be concentrated in a central peak and a small number of sidelobes. Thus it is expected that for M days of data, the signal-to-noise ratio will be proportional to M. Additional methods of improving the signal-to-noise ratio are introduced in the next chapter.

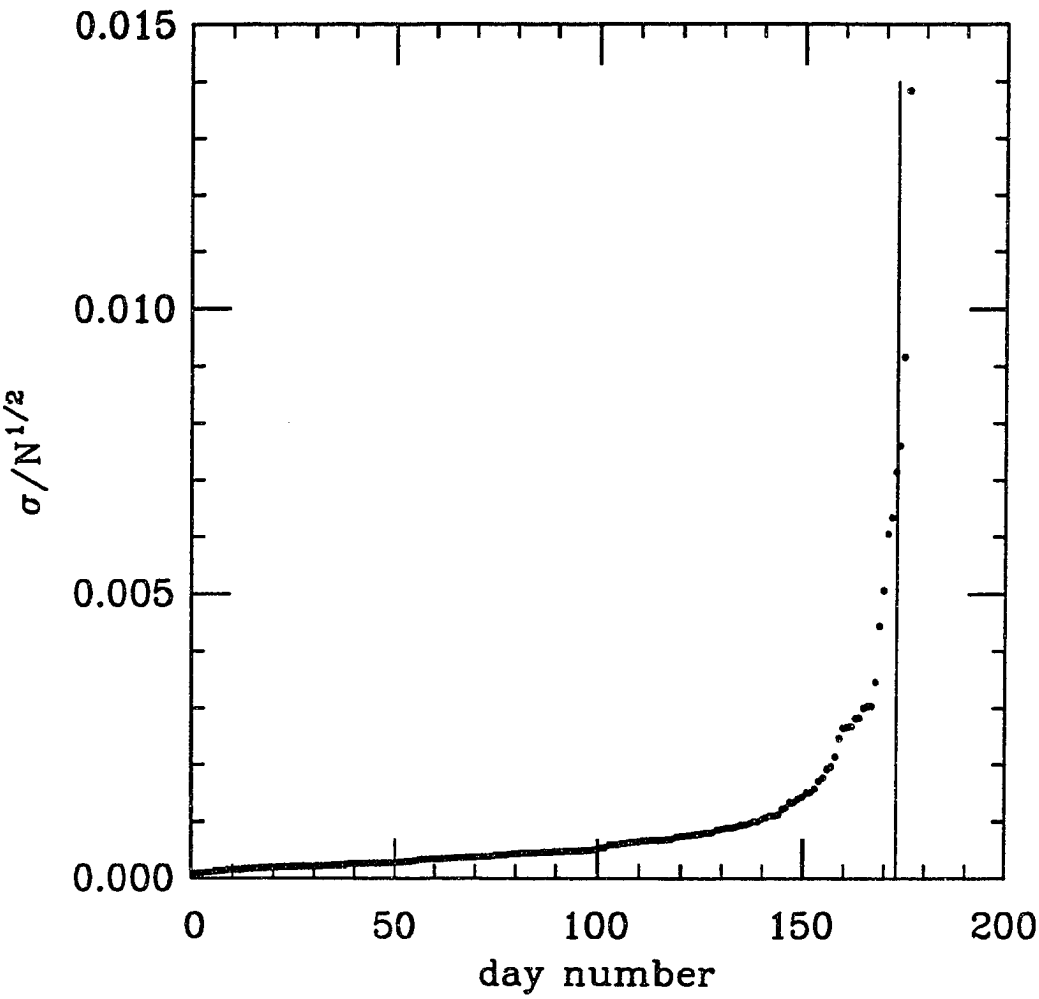

Figure 3.12: Standard deviation of the mean as a function of day number. The days have been ranked in order of increasing standard deviation. The vertical line is the cutoff above which days were rejected. Results are for Ge detector #1.

Chapter 4

Power Spectrum Analysis

4.1 Computation of the FFT

The Fourier Transform of the data was computed using an FFT routine which allows the spectrum to be computed on subintervals of the total frequency range. This represents a savings in both computation and memory, since the regions of the spectrum expected to be devoid of solar normal modes need not be computed. For each day d, the real and imaginary parts of the Fourier transform are stored. The power density P_ν at the frequency ν for a given window function consisting of D days is then obtained from

$$P_\nu = \left(\frac{1}{N}\sum_{d=1}^{D} a_{d\nu}\right)^2 + \left(\frac{1}{N}\sum_{d=1}^{D} b_{d\nu}\right)^2, \tag{4.1}$$

where N is the total number of non-zero points in the time domain, and $a_{d\nu}$ and $b_{d\nu}$ are the real and imaginary parts of the Fourier transform, respectively. This procedure allows one to change the combination of days used in the Fourier transform without

recomputing the $a_{d\nu}$'s and $b_{d\nu}$'s. It is essential in implementing equation (4.1) that all times are measured relative to a common origin. In this case, the reference time was chosen as midnight, January 1, 1991.

Prior to computation of the FFT, a few final time-domain operations were performed on the daily time series $\mathcal{S}_\lambda(t)$ that were obtained as described in § 3.3. Gaps in the daily time series were filled with zeros, and the ends of each daily time series of n_d points were smoothly tapered to zero by multiplying the first 10% of the points by $\sin^2(5\pi j/n_d)$, where j runs from 1 to $n_d/10$, and the last 10% of the points by $\sin^2(5\pi(n_d - j)/n_d)$, where j runs from n_d to $0.9n_d$. Finally, the residual DC component was removed by subtracting the mean. The natural linewidths for the five-minute oscillations have been found to be on the order of 1 μHz corresponding to a lifetime $1/(\pi\Delta\nu) \sim 3 - 5$ days (Hill 1985a). Spectral resolution of 1 μHz can be obtained in the Fourier analysis of time strings spanning 10 days. Increasing the resolution beyond the natural line widths of the five-minute oscillations would complicate their detection since modes that are reexcited with an arbitrary relative phase lag would produce interference patterns in the power spectrum (Hill 1985a). Also, high duty cycles which enhance statistical stability in the frequency domain are more difficult to achieve in very lengthy time strings. Therefore, the data were grouped into sets spanning 9 or 10 days and having high duty cycles. A total of 72 days of data were grouped into 9 such sets. The dates and duty cycles are given in table 4.1. Note that one day, October 11, 1991, has been used in two sets.

TABLE 4.1

Time Strings Analyzed For Solar Oscillations

Dates	Duty Cycle
April 9, 1991 – April 17, 1991	33.9%
April 19, 1991 – Apr28, 1991	20.6%
May 11, 1991 – May 19, 1991	35.6%
June 15, 1991 – June 23, 1991	34.5%
October 2, 1991 – October 11, 1991	23.7%
October 11, 1991 – October 19, 1991	23.0%
October 31, 1991 – November 8, 1991	27.1%
November 17, 1991 – November 25, 1991	17.7%
February 19, 1992 – February 28, 1992	22.1%

The effect of the window functions on the distribution of signal power in the frequency domain was tested by performing a Fourier transform on artificial data having the same window function as the real data modulating a single sinusoid of frequency 3mHz. This was done for each of the nine data sets in table 4.1. The average of the resulting power spectra is displayed in figure 4.1. First and second order 1/day sidebands are clearly visible at ± 11.57 and ± 23.14 μHz from the central peak. It should be borne in mind that the duty cycles quoted in table 4.1 are rather good for a single observing site at a temperate latitude. Nevertheless, a considerable amount of signal power is seen to leak into the sidebands.

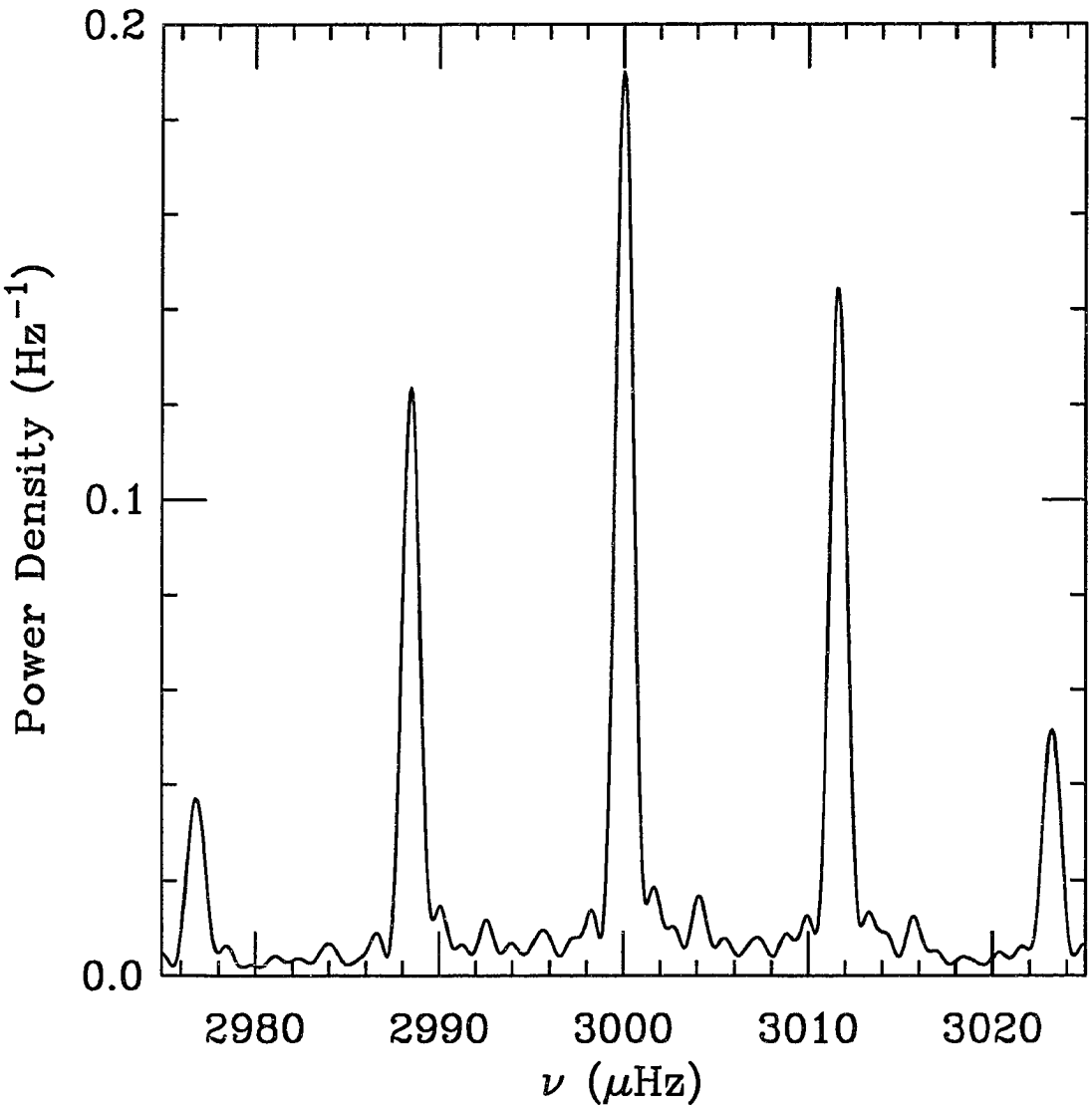

Figure 4.1: Average window function test for the nine time strings given in table 4.1.

The average power spectrum was computed for Ge detector 1 using the data sets in table 4.1. The result obtained from the data at 0.5 μ is plotted from 0 to 6 mHz in figure 4.2. The large peaks beween 100 and 400 μHz contain too much power to be attributable solely to solar oscillations. In fact, the power density in the region below 1.5 mHz exhibits a $1/\nu$ behavior typical of power spectra of noisy data. The power at the lowest frequencies has been significantly attenuated by the data reduction techniques in the time domain. The concentration of noise power at low frequencies is encouraging from the standpoint of detection of five-minute oscillations. It indicates that the preliminary estimate of the signal-to-noise ratio based on a white noise source given at the end of the previous chapter was overly conservative. Moreover, the signal-to-noise ratio per frequency bin has been improved by roughly a factor of 25 over that obtainable from single days simply by increasing the resolution. Another factor of three was obtained in averaging nine independent power spectra. The resulting mean power density in the five-minute band, from 1.5 to 5.5 mHz, is 2.42×10^{-13} Hz^{-1} which is near the magnitude expected for solar oscillations. At this point, one cannot predict with certainty the precise signal-to-noise ratio since the signal amplitudes are *a priori* unknown. It appears, however, that a ratio of ~ 1 is within reach. A procedure is introduced in the next section which drives down the noise power by an additional factor of 2.7.

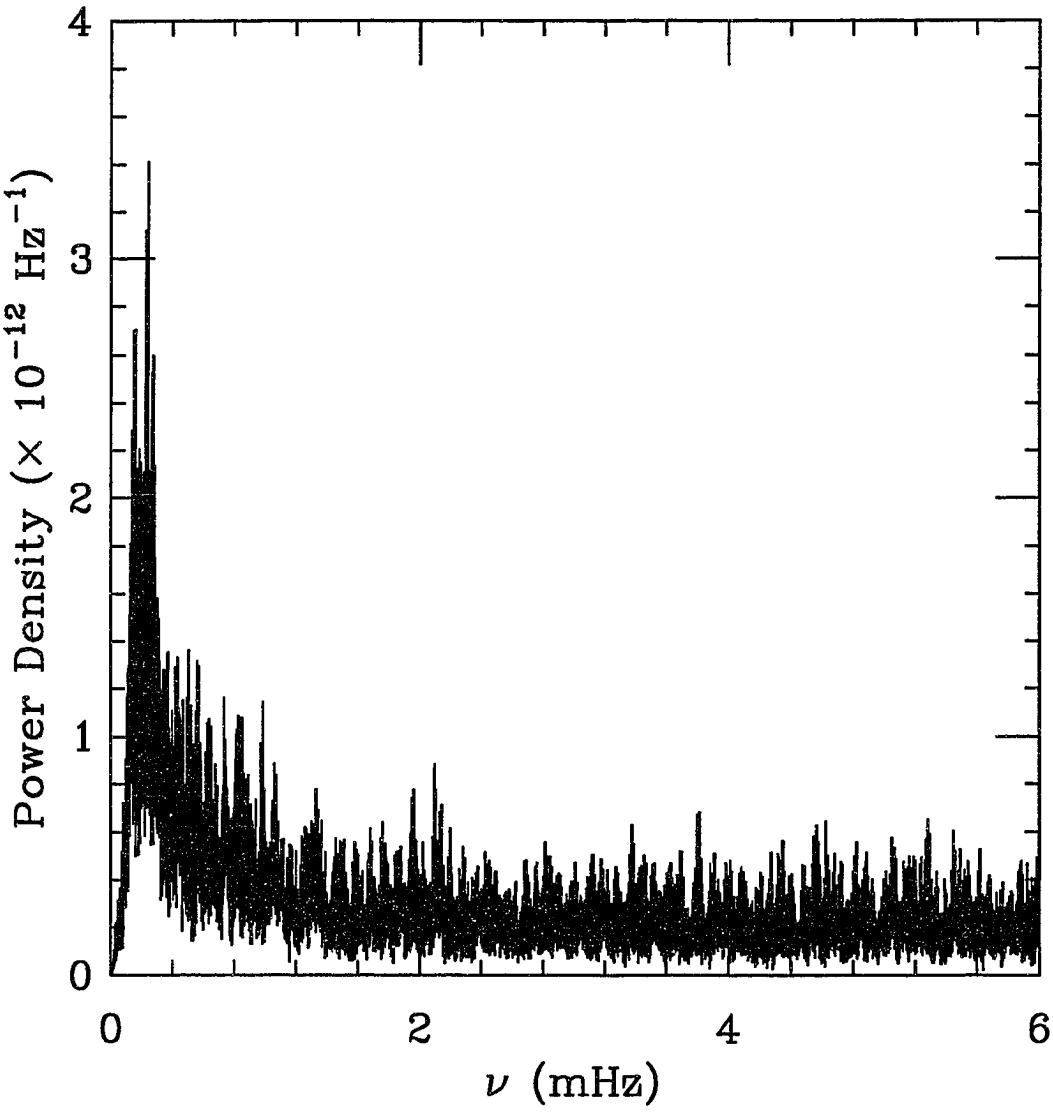

Figure 4.2: Average power density spectrum obtained for Ge detector #1 at 0.5 microns.

4.2 Noise Reduction in the Frequency Domain

Since the concentration of atmospheric aerosols responsible for Mie scattering is highly variable in space and time, Mie scattered radiation represents a significant broad-band source of noise in these observations. Figures 3.1 – 3.4 indicate that while the amplitudes of the infrared signals are roughly 10 times smaller than the visible signals, the former are more strongly influenced by changing aerosol concentrations. In fact, it was predicted in § 2.4 that the ratio of the infrared to the visible signals due to Mie scattering is 100 times greater than that due to Rayleigh scattering. Variations in the infrared signals due to a changing distribution of atmospheric aerosols should therefore be larger than the corresponding variations in the visible signals. This is confirmed in the frequency domain where it is found that the average power density computed from the infrared signals is about 100 times that of the visible signals. One may therefore conclude that the average noise power density due to Mie scattering is $\sim$ 100 times greater in the infrared power spectra than in the visible. This important observation is now used to reduce the noise power in the visible spectrum which originates in the Earth's atmosphere.

The power spectral density at the frequency ν may be written as

$$P_\nu = P_{s\nu} + P_{n\nu} + \sqrt{P_{s\nu} P_{n\nu}} \cos \varphi_\nu, \tag{4.2}$$

where the subscripts s and n refer to solar signal and noise, respectively, and φ_ν is the relative phase between the signal and noise amplitudes. From the above discussion,

the power spectrum derived from the infrared signal is expected to be dominated by noise. Scaling the IR power density by a factor of about 0.01 would result in a power density of the same magnitude as that derived from the visible signal. Under the hypothesis that the solar signal power density in the unscaled IR spectrum is of the same order of magnitude as that in the visible spectrum, subtraction of the scaled IR spectrum from the visible spectrum would be expected to significantly attenuate the noise power while leaving the solar signal in the visible spectrum relatively unaffected. This approach in general leads to negative as well as positive power densities, however, which may complicate the interpretation. Therefore, a slightly different procedure was followed in which the infrared amplitude $A_{i\nu} \equiv +\sqrt{P_{i\nu}}$ is scaled and subtracted from the visible amplitude $A_{v\nu} \equiv +\sqrt{P_{v\nu}}$. The difference is then squared yielding a positive-definite quantity with units of power density:

$$P_\nu = [A_{v\nu} - r_\nu A_{i\nu}]^2 . \tag{4.3}$$

The scale factor r_ν was allowed to vary gradually with frequency as

$$r_\nu = a_0 + a_1\nu + a_2\nu^2, \tag{4.4}$$

where the constants a_0, a_1, and a_2 are obtained by performing a quadratic least-squares fit to the function $A_{v\nu}/A_{i\nu}$ over the frequency range of interest. It is found that r_ν is on the order of 0.1 as expected. Thus, the solar signal will suffer substantial cancellation only if the solar signal amplitude present in the infrared spectrum is on the order of 10 times that in the visible spectrum.

In combining the power spectra resulting from the nine data sets in table 4.1, P_ν can be evaluated from equation (4.3) for each window function individually, and then averaged. The noise reduction was found to be enhanced by the inclusion of a global scale factor x which is chosen to minimize the integrated power. The resulting function, denoted by $P_{1\nu}$, is written as

$$P_{1\nu} = \frac{1}{M}\sum_{m=1}^{M}\left[A_{\nu\nu m} - x r_{\nu m} A_{i\nu m}\right]^2, \tag{4.5}$$

where $M = 9$ in this case. The need for the additional factor x is understandable since, while the factor r_ν is defined such that the sum $\sum_\nu (r_\nu - A_{\nu\nu}/A_{i\nu})^2$ is minimized, it will not in general minimize the sum $\sum_\nu (A_{\nu\nu} - r_\nu A_{i\nu})^2$. The global scale factor x which minimizes the integrated power is given by

$$x = \frac{\sum_\nu \overline{r_\nu A_{\nu\nu} A_{i\nu}}}{\sum_\nu \overline{r_\nu^2 P_{i\nu}}}, \tag{4.6}$$

where an overbar denotes an average over the nine spectra. The quantity x is proportional to the magnitude of the cross term in equation (4.5), which is a measure of the degree of correlation between $A_{\nu\nu}$ and $A_{i\nu}$. It is the correlated power, moreover, which is attributable to terrestrial noise. The values of x obtained for detectors 1–4 in the domain of the five-minute oscillations are 0.55, 0.60, 0.53, and 0.56, respectively. With the assumption that $A_{\nu s\nu} \gtrsim A_{i s\nu}$, equation (4.5) becomes

$$P_{1\nu} \simeq \overline{(A_{\nu n\nu} - x r_\nu A_{i n\nu})^2} + \left(\frac{3}{2} - x\right)\overline{P}_{\nu s\nu} \pm \frac{1}{3}\sqrt{2\overline{P}_{\nu s\nu} P_{1\nu}}. \tag{4.7}$$

The formal error in $P_{1\nu}$ arises from the average over $\varphi_{\nu\nu}$ and $\varphi_{i\nu}$, and is proportional

to the square root of $P_{1\nu}$ itself. The noise term averaged over frequency is minimized by the choice of x, but is not in general equal to zero for a particular value of ν.

An alternative approach is to average the visible and infrared power spectra before computing the scale factor and taking the difference, with the result

$$\begin{aligned} P_{2\nu} &= \left[\overline{P}_{v\nu}^{1/2} - r_\nu \overline{P}_{i\nu}^{1/2}\right]^2 \\ &\simeq \left[\overline{P}_{vn\nu}^{1/2} - r_\nu \overline{P}_{in\nu}^{1/2}\right]^2 + \frac{1}{4}\left(\frac{S}{N}\right)_{v\nu} \overline{P}_{vs\nu} \pm \frac{1}{3}\overline{A}_{vs\nu}\sqrt{2P_{2\nu}}, \end{aligned} \tag{4.8}$$

where the second line results from the assumption that $A_{vs\nu} \gtrsim A_{is\nu}$. Since the function r_ν is primarily a fit to the ratio of noise amplitudes, the average over frequency of the noise term in equation (4.8) is minimized. The magnitude of this term may well be non-negligible at a particular frequency, however. As in the case of $P_{1\nu}$, the formal error in $P_{2\nu}$ arises from averaging over $\varphi_{v\nu}$ and $\varphi_{i\nu}$, and is proportional to the square root of $P_{2\nu}$ itself. The ratio $(S/N)_{v\nu}$ represents the ratio of signal power to noise power in the visible spectrum. It is estimated to be ~ 0.1 at the frequency of a mode of solar oscillation. Thus the coefficient of the $\overline{P}_{vs\nu}$ term in equation (4.8) ~ 0.025 as compared to ~ 1 in the case of $P_{1\nu}$. Therefore, only the spectrum $P_{1\nu}$ is analyzed for solar signals in the following section.

4.3 Detection of Axisymmetric Five-Minute Oscillations

The frequencies of the axisymmetric ($m = 0$) five-minute oscillations have been well established through Doppler studies of spectral lines. In searching for evidence of these modes in intensity measurements it is natural, therefore, to look for a concentration of power density at the known frequencies. The frequencies used in the current study were taken from tables published by Libbrecht, Woodard, and Kaufman (1990). Frequencies for $\ell = 0$–3 are reproduced here in table 4.2. Twenty-two frequencies are available for each angular degree ℓ. Therefore, a *superimposed frequency analysis* may be performed in which regions of the power spectrum registered to the 22 classified frequencies for each ℓ are averaged, and the statistical significance of peaks in this average spectrum is evaluated. The statistical significance of a peak is given by the number of standard deviations it lies from the mean power density. This quantity is referred to as the Z statistic (see Box, Hunter, and Hunter 1978),

$$Z \equiv \frac{\overline{s} - \mu}{\sigma/\sqrt{n}}, \tag{4.9}$$

where $\overline{s}$ is the sample mean, n is the number of points in the sample, and the population mean μ, and population standard deviation σ are estimated from the spectrum $P_{1\nu}$ between 1800 and 4776 μHz. The probability density of the power $P_{1\nu}$ is distributed approximately as a chi-square distribution with nine degrees of freedom. The means of randomly drawn samples of 22 points are therefore normally

TABLE 4.2
p-Mode Frequencies in μHz
Obtained From Doppler-Shift Measurements

radial order	$\ell = 0$	$\ell = 1$	$\ell = 2$	$\ell = 3$
11			1815.40±0.10	1868.20±1.20
12	1823.60±0.60	1885.50±0.40	1947.50±0.40	2003.40±0.60
13	1957.30±0.40	2020.70±0.40	2084.10±0.30	2138.70±0.30
14	2093.50±0.20	2156.70±0.40	2218.40±0.30	2274.70±0.30
15	2228.60±0.10	2291.90±0.20	2352.20±0.20	2409.40±0.30
16	2362.50±0.10	2426.10±0.20	2486.80±0.10	2541.50±0.21
17	2496.60±0.30	2558.90±0.20	2619.82±0.23	2676.83±0.22
18	2629.60±0.30	2693.60±0.30	2754.67±0.17	2811.29±0.17
19	2764.40±0.10	2828.10±0.20	2889.96±0.16	2947.33±0.20
20	2899.30±0.10	2963.30±0.20	3024.30±0.09	3082.63±0.21
21	3033.80±0.10	3098.70±0.10	3159.78±0.20	3217.94±0.20
22	3168.60±0.20	3233.20±0.30	3295.68±0.25	3354.28±0.18
23	3304.10±0.30	3368.90±0.10	3431.20±0.20	3489.36±0.35
24	3439.80±0.30	3504.60±0.20	3567.20±0.50	3626.10±0.30
25	3576.30±0.60	3640.20±0.40	3703.30±0.20	3760.90±0.30
26	3711.50±0.20	3777.40±0.70	3837.80±0.80	3897.60±0.60
27	3847.40±1.00	3914.10±0.70	3975.50±0.40	4035.00±0.70
28	3984.90±0.30	4052.10±0.70	4112.90±0.40	4171.70±0.70
29	4121.90±0.40	4189.80±0.40	4249.30±0.50	4308.60±1.00
30	4257.40±0.40	4325.60±0.30	4387.30±0.40	4443.80±0.80
31	4394.90±0.20	4463.60±0.70	4524.20±0.40	4583.50±0.30
32	4532.30±0.80	4600.80±0.20	4656.90±0.80	4717.40±0.60
33	4668.60±0.50	4738.60±0.70		

Excerpt from Table 1, Libbrecht, Woodard and Kaufman (1990).

distributed to a high degree of accuracy by virtue of the central limit theorem.

A superimposed frequency analysis has been performed on the power spectrum derived from Ge detector 1. Before presenting the results for the optimum scale factor x given by equation (4.6), it is instructive to observe the properties of $P_{1\nu}$ when x is allowed to vary. For $\ell = 0$–3, the Z statistic has been plotted as a function of the parameter x within a 12 μHz region about the $m = 0$ frequency. The results are displayed in figures 4.3–4.6, respectively. Figures 4.3, 4.4, and 4.6 represent the superposition of 22 independent regions of the power spectrum $P_{1\nu}$. Only 21 regions were superimposed in figure 4.5 for $\ell = 2$, however. This is because a 6 σ peak occurred at the frequency of the $n = 13$, $\ell = 2$ axisymmetric mode. Since this power level is inconsistent with the typical power densities observed at other mode locations, and because the inclusion of this peak would significantly alter the results, it has been omitted in the following analysis. The cancellation of noise power in figures 4.3–4.6 is reflected by the many contours of constant frequency which go through a minimum near $x = 0.55$. At this value of x, power at frequencies where cancellation does not occur becomes relatively more prominent, resulting in a maximum in Z. At some frequencies, maximum cancellation occurs at an x value slightly different from $x = 0.55$. In these cases, peaks in Z will occur near $x = 0.55$ which are due to noise. These noise peaks can often be identified as such by the presence of a local minimum in Z at a nearby value of x. The most important observation concerning figures 4.3–4.6 is that the peaks along the $x = 0.55$ contour are located at frequencies which are

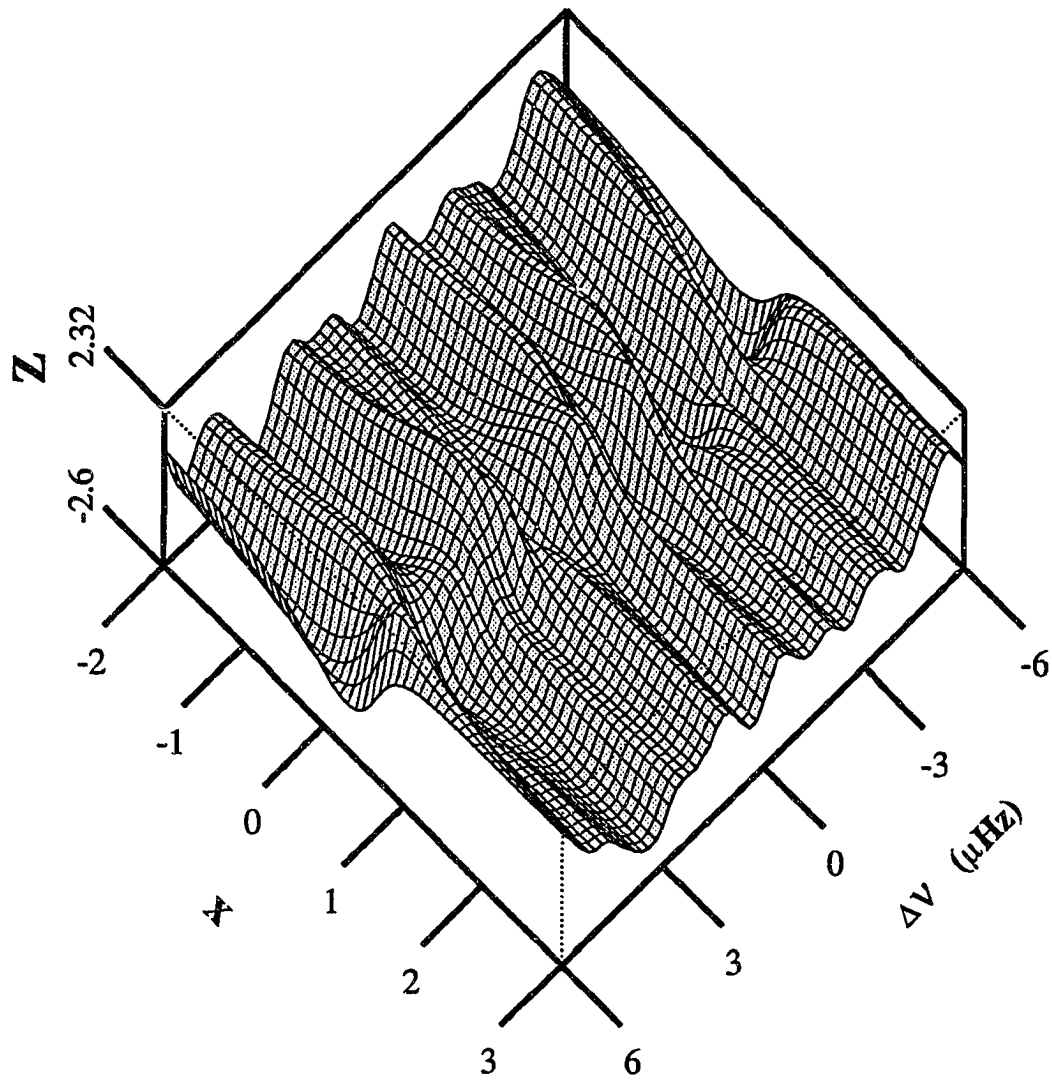

Figure 4.3: The Z statistic computed from 22 regions of the power spectrum as a function of $\Delta\nu$ and x where $\Delta\nu$ is frequency relative to the ℓ=0, m=0 frequencies obtained from velocity observations, and x is a global scale factor by which the infrared amplitude is multiplied prior to subtraction from the visible amplitude.

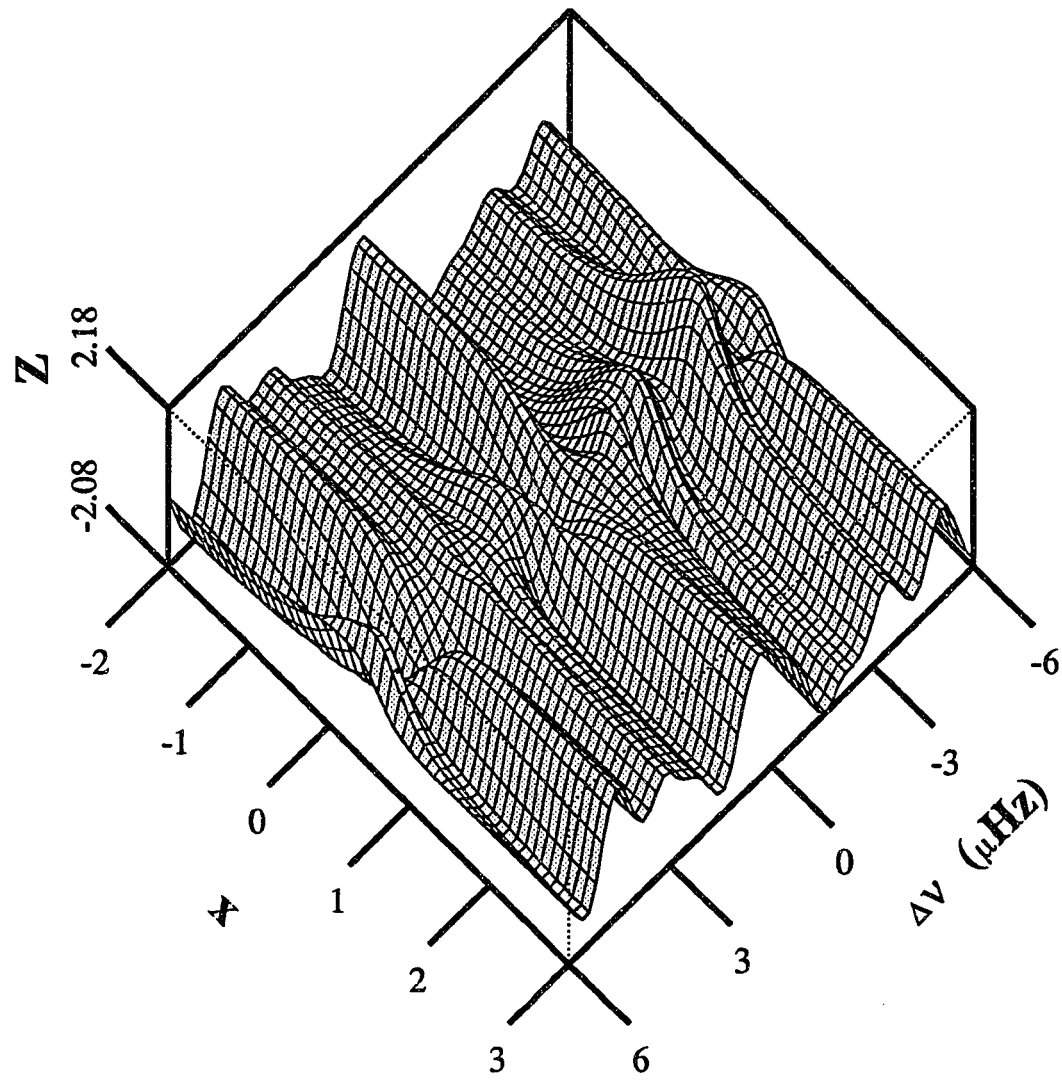

Figure 4.4: The Z statistic computed from 21 regions of the power spectrum as a function of $\Delta\nu$ and x where $\Delta\nu$ is frequency relative to the ℓ=1, m=0 frequencies obtained from velocity observations, and x is a global scale factor by which the infrared amplitude is multiplied prior to subtraction from the visible amplitude.

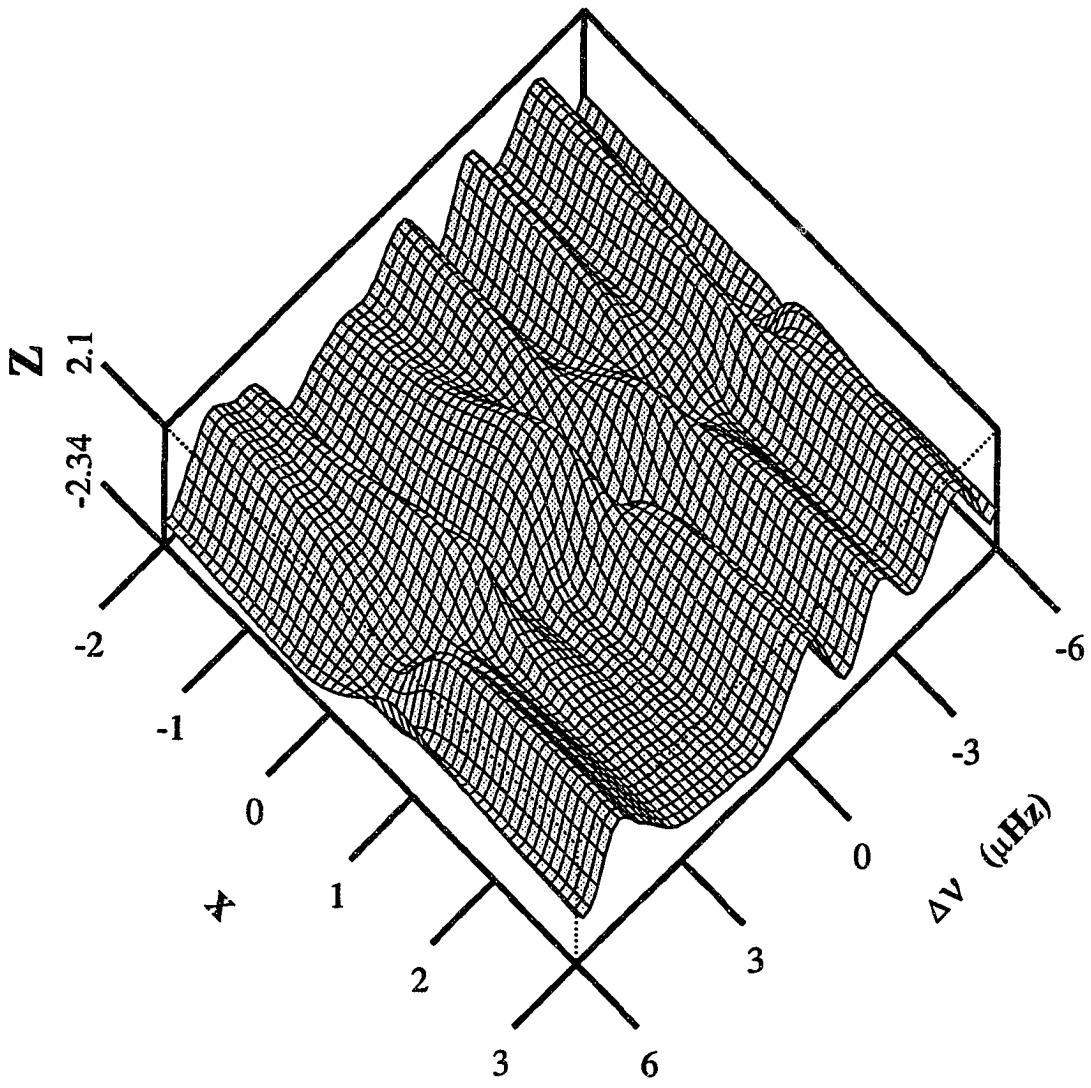

Figure 4.5: The Z statistic computed from 22 regions of the power spectrum as a function of $\Delta\nu$ and x where $\Delta\nu$ is frequency relative to the ℓ=2, m=0 frequencies obtained from velocity observations, and x is a global scale factor by which the infrared amplitude is multiplied prior to subtraction from the visible amplitude.

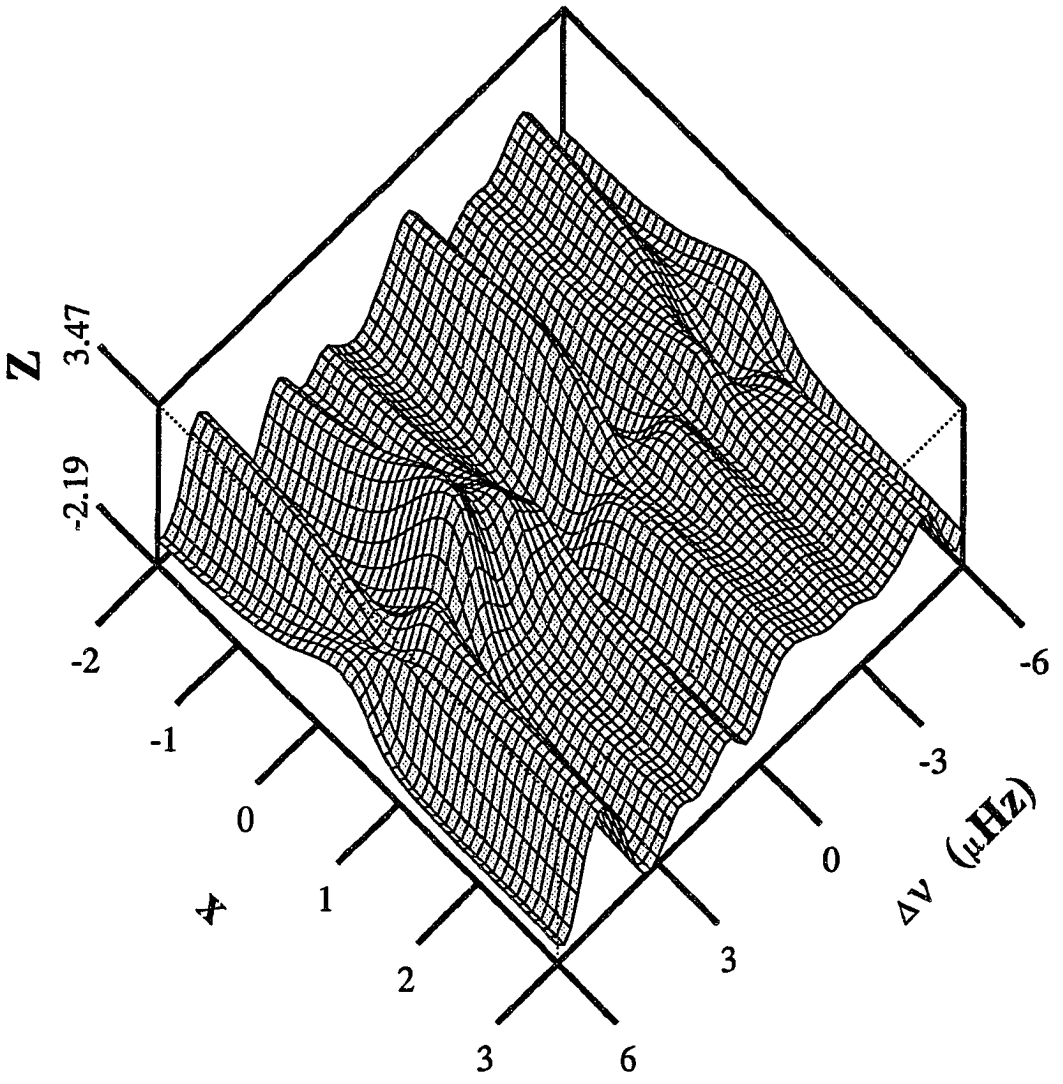

Figure 4.6: The Z statistic computed from 22 regions of the power spectrum as a function of $\Delta\nu$ and x where $\Delta\nu$ is frequency relative to the ℓ=3, m=0 frequencies obtained from velocity observations, and x is a global scale factor by which the infrared amplitude is multiplied prior to subtraction from the visible amplitude.

independent of the frequencies of peaks away from this value. This demonstrates that the subtraction of the scaled infrared amplitude from the visible in is an essential ingredient in the effort to resolve signal peaks.

Consider now the two-dimensional slices through figures 4.3–4.6 taken at $x = 0.55$. These are displayed in figures 4.7–4.10 for the $\ell = 0$–3 multiplets, respectively. The left-hand ordinate in these figures gives the standard deviations from the mean, or Z, while the right-hand ordinate gives the power density. One may at once suspect that a non-random process is at work due to the relatively frequent occurrence of peaks above the 1 σ level. The prominent minima in these figures also point to the presence of coherent signals since destructive interference may occur in the region between two closely spaced signal peaks. Recall from the discussion of detection sensitivity in § 1.5 that, from a consideration of the symmetry properties of the modes, whole-disk observations are sensitive only to modes having $\ell + m$ even. Thus, a concentration of power at the $m = 0$ frequencies is expected for the $\ell = 0$ and 2 multiplets, while no excess power density is expected at the corresponding frequencies for $\ell = 1$ or 3. The significance levels at the $m = 0$ frequency for $\ell = 0$ and 2 are each $\geq 1.05\ \sigma$, corresponding to a probability of $(0.147)^2$, while the significance levels at the $m = 0$ frequency for $\ell = 1$ and 3 are each $\leq 0.17\ \sigma$ corresponding to a probability of $(0.567)^2$. The joint probability of finding power density at the 1.05 σ level or above at both symmetry-allowed locations and finding power density at the 0.17 σ level or below at both symmetry-forbidden locations is $(0.147)^2(0.567)^2 = 6.9 \times 10^{-3}$. Thus

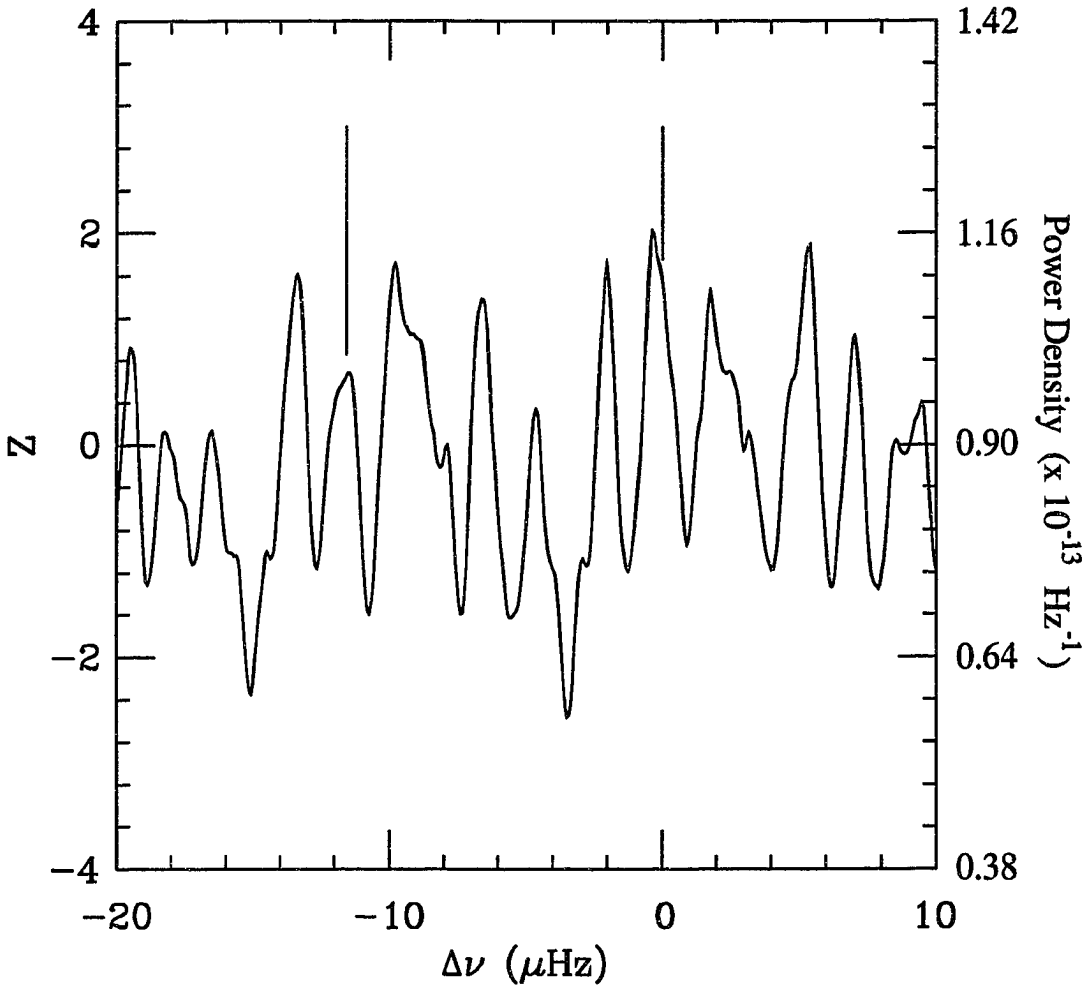

Figure 4.7: Superposition of 22 regions of the power spectrum registered to ℓ=0 frequencies. The right-hand ordinate is in units of power density, and the left-hand ordinate is in units of standard deviations from the mean for the region 1800 - 4776 μHz. The abscissa $\Delta\nu$ is frequency relative to the ℓ=0 frequencies obtained from velocity observations. Vertical lines indicate the expected locations of the ℓ=0 peak and its -1/day sideband.

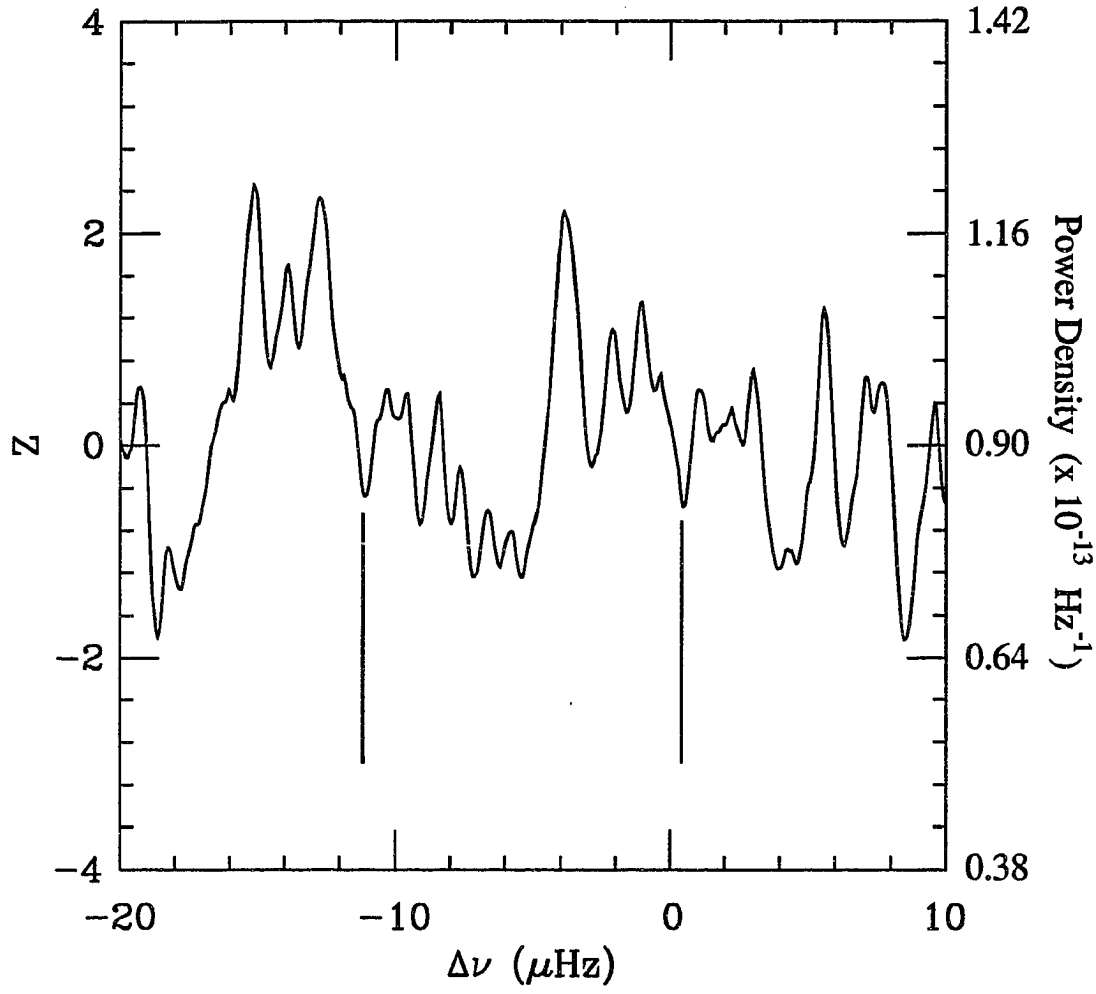

Figure 4.8: Superposition of 22 regions of the power spectrum registered to ℓ=1, m=0 frequencies. The right-hand ordinate is in units of power density, and the left-hand ordinate is in units of standard deviations from the mean for the region 1800 - 4776 μHz. The abscissa $\Delta\nu$ is frequency relative to the ℓ=1, m=0 frequencies obtained from velocity observations. Vertical lines indicate the expected locations of the (symmetry-forbidden) ℓ=1, m=0 mode and its -1/day sideband when solar-cycle effects are included.

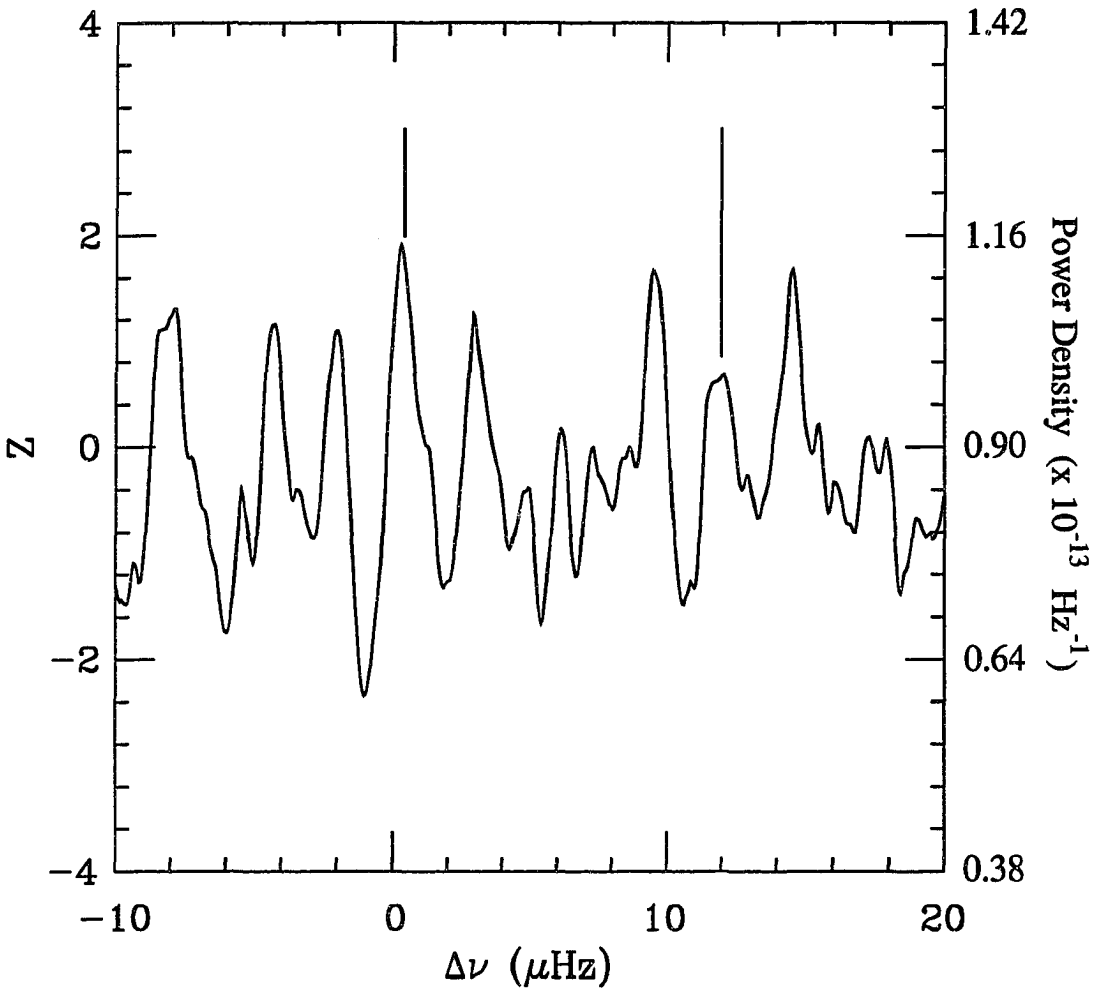

Figure 4.9: Superposition of 21 regions of the power spectrum registered to ℓ=2, m=0 frequencies. The right-hand ordinate is in units of power density, and the left-hand ordinate is in units of standard deviations from the mean for the region 1800 - 4776 μHz. The abscissa Δν is frequency relative to the ℓ=2, m=0 frequencies obtained from velocity observations. Vertical lines indicate the expected locations of the ℓ=2, m=0 peak and its 1/day sideband when solar-cycle effects are included.

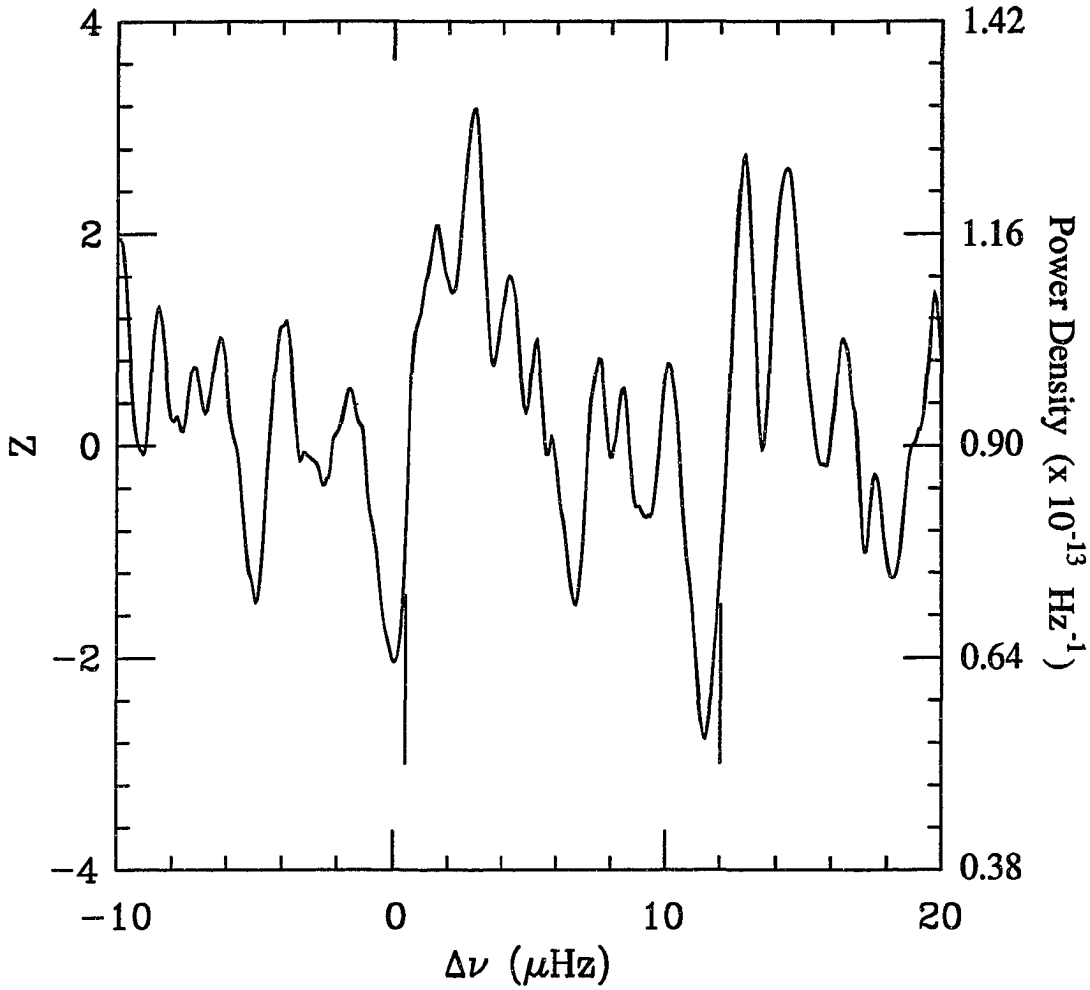

Figure 4.10: Superposition of 22 regions of the power spectrum registered to ℓ=3, m=0 frequencies. The right-hand ordinate is in units of power density, and the left-hand ordinate is in units of standard deviations from the mean for the region 1800 - 4776 μHz. The abscissa $\Delta\nu$ is frequency relative to the ℓ=3, m=0 frequencies obtained from velocity observations. Vertical lines indicate the expected locations of the (symmetry-forbidden) ℓ=3, m=0 mode and its 1/day sideband when solar-cycle effects are included.

it is quite unlikely that the observed symmetry property has occurred by chance.

The Doppler-shift frequencies given in table 4.2 were obtained in 1986–87 during a minimum in solar-activity. The results of the current study are based on data gathered in 1991–92, corresponding to a peak period of solar activity. Oglesby, Hill and Rabaey (1989) reported a change in p mode frequencies over a time interval corresponding to a maximum variation in solar activity. Woodard *et al.* (1991) found a linear correlation between p mode frequencies and the strength of surface activity. Solar-cycle-dependent frequency shifts for low-ℓ modes were measured by Pallé, Régulo and Roca Cortés (1990 a,b). They report shifts of 0.42 ± 0.06, 0.38 ± 0.14, and 0.47 ± 0.10 for $\ell = 1$–3, respectively, when the solar-activity cycle goes from minimum to maximum, the effect being absent for $\ell = 0$. The expected $m = 0$ frequencies when these shifts are included are indicated by the vertical lines in figures 4.7–4.9. Using the power density at the shifted frequencies, the joint probability that the observed symmetry properties have occured by chance is 2.9×10^{-4}

Adopting the hypothesis that the peaks near the $m = 0$ frequencies in the $\ell = 0$ and $\ell = 2$ spectra are in fact due to the $m = 0$ modes, the confidence levels for the $\ell = 0$ and $\ell = 2$, $m = 0$ modes are 97.3% and 97.5%, respectively. It is now possible to compute the average physical amplitudes $\overline{\mathcal{I}}'_{0.5}/\mathcal{I}_\circ$ of the $\ell = 0$, $n = 12$–33 and $\ell = 2$, $n = 11$,12,14–32 axisymmetric p modes. Making the conservative assumption that the average power density is equal to the average noise power density, the average signal power density is obtained by subtracting the mean power density from the

peak height. Several factors must then be taken into account. First, there is the factor $(3/2 - x) = 0.95$ which appears in equation (4.7). Then there is a correction for spectral leakage due to the window function. The window function test shown in figure 4.1 was computed for a sinusoid of unit amplitude. This figure suggests that a factor of 1/0.19=5.263 is needed to obtain the correct power density. Finally, there is a factor of $1/\eta$, as can be seen from equation (3.10), relating the quantity $\mathcal{S}_\lambda$ to the relative intensity oscillations $\mathcal{I}'_\lambda/\mathcal{I}_{o\lambda}$. Using the value of $\overline{\eta}$ given for Ge detector 1 at 0.5 μ in table 3.1, the average amplitudes for the $\ell = 0$ and $\ell = 2$, $m = 0$ modes have been calculated and are presented in table 4.3. By way of comparison, the results of Woodard and Hudson (1983), obtained from an analysis of the Solar Max Mission total irradiance data, imply average relative amplitudes of $(1.812 \pm 0.071) \times 10^{-6}$ for $\ell = 0$ averaged over n = 18–24, and $(1.501 \pm 0.073) \times 10^{-6}$ for $\ell = 2$ averaged over n = 17–23. It must be remembered, however, that the results in table 4.3 are obtained for a 90 Å interval centered on 0.5 μ.

TABLE 4.3

Average Mode Amplitude at 0.5 μ

ℓ	m	$\overline{\mathcal{I}'}/\mathcal{I}_o$	Confidence
0	0	$(7.54 \pm 0.54) \times 10^{-7}$	97.3%
2	0	$(7.68 \pm 0.56) \times 10^{-7}$	97.5%

4.4 Rotational Splitting

Since whole-disk observations are sensitive only to modes having $\ell + m$ even, all rotationally-split members of a multiplet are not expected to be present. The symettry-allowed multiplet members are listed in table 4.4. The term *rotational splitting* refers to the frequency splitting between adjacent members of a multiplet. Since only every other multiplet member can be present in this case, the splittings measured from figures 4.7–4.10 must be divided by two for purposes of comparison with other results. Many researchers have reported rotational splitting values very close to the surface rotational frequency of 0.42 μHz. This would correspond to a peak spacing of about 0.84 μHz in spectra obtained from whole-disk observations. The natural linewidths of these modes are expected to be about 1 μHz, so that peaks spaced at 0.84 μHz should appear strongly blended. The peak seperation in figures 4.8–4.10 seems to rule out such a small rotational splitting. In particular, the strong central minimum in figure 4.10 and the strong minimum at -1 μHz in figure 4.9 suggest that rotational splitting near 0.42 μHz is quite unlikely in the cases of $\ell = 2$ and 3.

Table 4.4
Symmetry Allowed Modes

ℓ	m
0	0
1	-1,1
2	-2,0,2
3	-3,-1,1,3

While no rotational splitting is expected in the $\ell = 0$ case, figure 4.7 contains a number of strong off-axis peaks. These can be identified as the 1/day sidebands of the members of the $\ell = 2$ multiplet since the mean spacing between the $\ell = 0$ and $\ell = 2$ multiplets having adjacent radial orders is 9.2 ± 0.9 μHz. Thus, the strongly blended peak at +2 μHz is attributable to the +1/day sideband of the $\ell = 2$, $m = 0$ peak. The broadening of this peak is understandable since the frequency alignment of the portions of the power spectrum that were averaged in this figure was optimized for the $\ell = 0$ modes. It is tempting to identify the peaks at -2 μHz and +5.4 μHz as the $m = \pm 2$ members of the $\ell = 2$ multiplet. Careful examination of the x dependence in figure 4.3 reveals, however, that the peak at +5.4 μHz has the signiture of a noise peak as described in § 4.3. Returning to figure 4.7, it is apparrent that the peak under consideration is blended with a smaller, unresolved peak. This unresolved peak may yet be a candidate for the $\ell = 2$, $m = -2$ mode.

Moving now to figure 4.8 in which the frequency alignment is optimized to project the $\ell = 2$ multiplet, four prominent peaks have emerged. The peak at -2 μHz can be identified as the -1/day sideband of the $\ell = 0$ modes. The peak at +3 μHz corresponds to our candidate for the $\ell = 2$, $m = -2$ mode. Examination of the x dependence of this peak in figure 4.5 indicates that the noise component is much less dominant here than at the +1/day sideband location considered above. The asymmetry of this peak indicates, however, that interference effects are still important, making accurate frequency determination of the signal component difficult. Never-

theless, the seperation between the peak at -4.3 μHz and the one at +3 μHz is about 7.3 μHz, corresponding to a rotational splitting of about 1.83 μHz. A similar result was obtained by Hill (1985a) from differential radius data.

The average seperation between $\ell = 1$ and $\ell = 3$ multiplets having adjacent radial orders is 16.9$\pm$1.5 μHz. The 2.2 σ peak at -4 μHz in figure 4.8 is therefore attributable to the +1/day sideband of a peak in the $\ell = 3$ region. In the immediate neighborhood of the $\ell = 1$, $m = 0$ frequency, two peaks higher than the 1 σ level occur to the left of the central frequency whereas only one peak was expected. This fact, coupled with the marginal significance of the power to the right of the central frequency, makes any precise statement about the rotational splitting of the $\ell = 1$ multiplet impossible at this time. Similarly, the distribution of peaks in the $\ell = 3$ region does not clearly reflect the Zeeman-like pattern expected for rotational splitting. The concentration of power at +3 μHz is quite significant. It is, however, somewhat greater than expected based on the power at the $\ell = 0$ and $\ell = 2$ frequencies. Remember that the detection sensitivity is expected to *decrease* with increasing ℓ. Thus it is likely that a significant amount of noise power is contributing to this peak. More work is therefore required for the determination of rotational splitting in the $\ell = 3$ case as well.

Chapter 5

Conclusion

5.1 Summary

A new instrument has been developed for making unimaged whole-disk observations of low-degree solar normal-mode oscillations. The apparatus, referred to as the *sky monitor*, does not track the solar disk, but instead measures the radiant flux scattered by the Earth's atmosphere at 1.6 and 0.5 μ. The expected diurnal flux variation was obtained from a detailed radiative transfer calculation. Data were acquired for 15.5 months during 1991–92. Seventy-two days of data were analyzed for evidence of solar p modes in the frequency range 1800–4776 μHz. Noise generated by the Earth's atmosphere was reduced by scaling the Fourier amplitude computed from the infrared signal and subtracting it from the Fourier amplitude computed from the visible signal. A superimposed frequency analysis was then performed which revealed $\sim 2\ \sigma$ peaks

within 0.3 μHz of symmetry-allowed locations, while no excess power was detected at the symmetry-forbidden frequencies. The probability of obtaining by chance the observed excess power density at symmetry-allowed frequencies and deficit of power density at symmetry-forbidden frequencies was computed to be 6.9×10^{-3}. Correcting the frequencies for solar-cycle variations, the probability was reduced to 2.9×10^{-4}. These results indicate that it is quite unlikely that the observed symmetry properties have occurred by chance, and support the hypothesis that solar normal-mode signals are manifested in the data. The amplitudes $\mathcal{I}'/\mathcal{I}_0$ averaged over radial order n of the $\ell = 0$ and $\ell = 2$, $m = 0$ modes were found to be $(7.54 \pm 0.54) \times 10^{-7}$ and $(7.68 \pm 0.56) \times 10^{-7}$, respectively. These results are about a factor of two smaller than the amplitude of total irradiance oscillations measured from space. While the rotational splitting of the $\ell = 2$ multiplet appears to be consistent with that reported by Hill (1985a), results for $\ell = 1$ and $\ell = 3$ are inconclusive.

5.2 Discussion of Results

The symmetry test employed in § 4.3 is a powerful technique for evaluating the presence of solar signal in the data. It has produced strong evidence that solar oscillations have been detected despite having been implemented in a very conservative fashion. The probability that the observed symmetry properties could have occurred by chance decreases significantly when solar-cycle effects are included, from a 2.5 σ to a 3.5 σ result. This is primarily due to the improved alignment of the prominent

peak in the $\ell = 2$ region with the expected frequency. This result corroborates the frequency shift reported by Pallé, Régulo and Roca Cortés (1990a,b) for $\ell = 2$.

The strength of the central minimum in the $\ell = 3$ region did not effect the computed joint probability. Only the fact that the power density at the $\ell = 3$, $m = 0$ frequency was less than or equal to the power density at the $\ell = 1$, $m = 0$ frequency was used. It has been argued that the local minima at the symmetry-forbidden frequencies may be due to interference between nearby symmetry-allowed signals. These minima may also reflect, to some extent, the effect of signal power on the mean power density. If signal power makes a non-negligible contribution to the mean power density, then the power density at symmetry-forbidden frequencies would be expected to be somewhat below average.

The physical amplitudes $\mathcal{I}'/\mathcal{I}_\odot$ listed in table 4.3 are averages over 22 and 21 n values for the $\ell = 0$ and $\ell = 2$, $m = 0$ modes, respectively. Moreover, 72 days of data were used to generate the power spectrum, while a typical mode lifetime is on the order of 3–5 days. This means that a given mode will almost certainly be absent on at least some of the days used in the analysis, and that different n values may not be equally represented in the spectrum. Hill (1985a) estimated that the probability of an individual five-minute oscillation being excited to a detectable level is 0.5. Thus it is likely that the amplitudes listed in table 4.3 may be underestimated by a factor of two.

The sensitivity of whole-disk intensity observations for a mode of given ℓ and m

is given by (Hill and Kroll 1986)

$$2\pi K \mathrm{Y}_\ell^m \left(\frac{\pi}{2}, 0\right) \mathcal{I}'(0) \int_0^{\pi/2} g' \mathrm{P}_\ell \sin\theta \cos\theta \, d\theta, \tag{5.1}$$

where $\mathrm{Y}_\ell^m(\pi/2, 0)$ is the spherical harmonic at disk center, $\mathcal{I}'(0)$ is the Eulerian perturbation in radiation intensity at disk center, P_ℓ is the Legendre polynomial of degree ℓ, g' is a power series in $\cos\theta$ giving the variation of $\mathcal{I}'$ across the disk, and K is a constant. The ratio of detection sensitivity for modes of the same ℓ but different m is therefore simply the ratio of their respective spherical harmonics evaluated at disk center. In particular, the ratio of detection sensitivity for an $\ell = 2$, $m = 0$ mode to that for an $\ell = 2$, $m = 2$ mode is

$$\frac{\mathrm{Y}_2^0\left(\frac{\pi}{2}, 0\right)}{\mathrm{Y}_2^2\left(\frac{\pi}{2}, 0\right)} = \frac{2}{\sqrt{6}} \simeq 0.816. \tag{5.2}$$

If the peak at -4.3 μHz in figure 4.9 is identified as the $m = 2$ member of the $\ell = 2$ multiplet, then the observed ratio of the amplitude of the $\ell = 2$, $m = 0$ mode to the $\ell = 2$, $m = 2$ mode is 1.31. Correcting for the difference in detection sensitivity given by equation (5.2), the ratio of physical amplitudes is 1.6. By way of comparison, SCLERA differential radius observations imply a ratio of about 1.5 (Hill, Alexander and Caudell 1985). This tends to support the identification of the peak in question as the $m = 2$ member of the $\ell = 2$ multiplet and the subsequent splitting determination of $\sim$ 1.8 μHz. The observed ratio of the $m = 0$ mode amplitude to the $m = 2$ mode amplitude bears on the experimental determination of rotational splitting and has implications for theoretical work on mode-excitation mechanisms.

5.3 Discussion of Technique

One aspect of this work which should not be overlooked is the judicious choice of resolution for the power spectrum, determined by the length of the time strings that have been Fourier analyzed. The data was divided into nine sets having lengths of about nine days. This length produces a resolution sufficient to resolve individual modes and to study the rotational splitting. Had these sets been much longer, however, interference patterns would be expected to emerge due to the re-excitation of modes with arbitrary relative phase lags (Hill 1985a). This effect would considerably complicate the data analysis and interpretation, and may be partly responsible for the disparate rotational splitting results reported in the literature.

Another point worthy of mention is the precise frequency registration which has been employed in the superimposed frequency analysis. The superimposed spectra displayed in figures 4.7–4.10 have each been optimized for a particular ℓ value, enhancing the overall frequency and amplitude determinations. This has been made possible by the availability of extensive tables of accurately determined p mode frequencies. Previous superimposed frequency analyses have assumed a constant spacing between modes of different ℓ, and either constant or uniformly varying spacing between modes having the same ℓ but different n. Superposition of frequency intervals based on these assumptions tends to produce broadened peaks in the superimposed spectrum and compromises the determination of rotational splitting.

The noise-reduction technique introduced in Chapter 4 relies on the fact that the

visible and infrared radiation sample the same atmospheric conditions so that atmospheric noise at the two wavelengths is correlated. Atmospheric noise is due either to temporal variations in the spatial distribution of aerosols, or to density fluctuations along the path of the incident and scattered beams. It has been argued that the contribution to the noise due to aerosols, has a greater effect on the infrared signal than on the visible. In fact, the infrared Fourier amplitude was scaled by a factor of about 0.055 in order to maximize cancellation when subtracted from the visible amplitude. On the other hand, density fluctuations should produce the same fractional intensity variation at both wavelengths. Therefore, no correction has been made for density fluctuations in this analysis. Good agreement has nonetheless been obtained with Doppler-shift observations as well as with differential radius observations. It appears likely that density fluctuations have averaged out in the integration over all incident and scattered beams, which was discussed at length in § 3.3. Observations of direct sunlight, in contrast, can average density fluctuations only over a thin pencil of atmosphere between the detector and the top of the atmosphere.

5.4 Prospects for the Future

The superimposed frequency analysis has been useful in establishing the overall quality of the data. To make further progress, however, individual modes must be examined. The rotational splitting, in particular, may be better determined by such an analysis. The noise-reduction technique that has been developed will undoubtedly

have other applications. It may be applied to observations using direct as well as scattered light, and it may be extended from two to three wavelengths. This latter point is especially significant in light of the recent establishment of SCLERA's international network of three-color photometric solar telescopes. The sensitivity of intensity observations to solar oscillations does not decrease with decreasing frequency as do velocity observations. Thus, it may be worthwhile to apply this noise-reduction technique to lower frequencies in a search for evidence of low-order p modes and g modes. The wavelength dependence of atmospheric noise was previously noticed by Clarke (1978). He suggested that atmospheric aerosols may be swept along in the antinodes of terrestrial g modes, giving rise to the observed brightness fluctuations of the sky. If this interpretation is correct, the data obtained in this study may be fruitfully analyzed for terrestrial atmospheric waves. The sky monitor itself has proven to be a useful and low cost instrument which can be easily operated and maintained. A second-generation instrument could provide scientific and educational opportunities at the college or secondary level.

REFERENCES

Allen, C. W. 1973, *Astrophysical Quantities* (London: Athlone).

Andersen, B. N. 1984, *Mem. S. A. It.*, **55**, 339.

Andersen, B. N. 1986, In *Seismology of the Sun and the Distant Stars*, ed. D. O. Gough (Dordrecht: Reidel), 339.

Andersen, B. N., and Domingo V. 1988, In *Advances in Helio- and Asteroseismology*, ed. J. Christensen-Dalsgaard and S. Frandsen (Dordrecht: IAU), 67.

Andersen, B. N., and Maltby, P. 1983, *Nature*, **302**, 808.

Anguera Gubau, M., Pallé, P. L., Pérez Hernández, F., and Roca Cortés, T. 1990, *Solar Phys.*, **128**, 79.

Barnes, J. R. 1987, *Electronic System Design: Interference and Noise Control Techniques* (Englewood Cliffs, N.J.: Prentice-Hall).

Beckers, J. M., and Ayres, T. R. 1977, *Ap. J.*, **217**, L69.

Blackman, R. B., and Tukey, J. B. 1958, *The Measurement of Power Spectra* (New York: Dover).

Born, M., and Wolf, E, 1980, *Principles of Optics: Electromagnetic Theory of Propagation, Interference, and Diffraction of Light* (New York: Pergamon).

Bos, R. J., and Hill, H. A. 1983, *Solar Phys.*, **82**, 89.

Box, G. E. P., Hunter, W. G., and Hunter, S. J. 1978, *Statistics for Experimenters* (New York: Wiley).

Brookes, J. R., Isaak, G. R., and van der Raay, H. B. 1976, *Nature*, **259**, 92.

Brookes, J. R., Isaak, G. R., and van der Raay, H. B. 1978, *Mon. Not. R. Astr. Soc.*, **185**, 1.

Brown, T. M., Stebbins, R. T., and Hill, H. A. 1978, *Ap. J.*, **223**, 324.

Caudell, T. P., and Hill, H. A. 1980, *Mon. Not. R. Astr. Soc.*, **193**, 381.

Chandrasekhar, S. 1960, *Radiative Transfer* (New York: Dover).

Christensen-Dalsgaard, J. 1990, private communication.

Christensen-Dalsgaard, J., and Gough, D. O. 1976, *Nature*, **259**, 89.

Christensen-Dalsgaard, J., and Gough, D. O. 1982, *Mon. Not. R. Astron. Soc*, **198**, 141.

Clarke, D. 1978, *Nature*, **274**, 670.

Claverie, A., Isaak, G. R., and McLeod, C. P. 1981, *Solar Phys.*, **74**, 73.

Claverie, A., Isaak, G. R., McLeod, C. P., and van der Raay, H. B. 1979, *Nature*, **282**, 591.

Claverie, A., Isaak, G. R., McLeod, C. P., van der Raay, H. B., Pallé, P. L., and Roca Cortés, T. 1982, *Nature*, **299**, 704.

Claverie, A., Isaak, G. R., McLeod, C. P., van der Raay, H. B., and Roca Cortés, T. 1981, *Nature*, **293**, 443.

Dereniak, E. L., and Crowe, D. G. 1984, *Optical Radiation Detectors* (New York: Wiley).

Deubner, F.-L. 1975, *Astron. Astrophys.*, **44**, 371.

Deubner, F.-L. 1981, *Nature*, **290**, 682.

Deubner, F.-L., Ulrich, R. K., and Rhodes, E. J., Jr. 1979, *Astron. Astrophys.*, **72**, 177.

Domingo V. 1990, In *Progress of Seismology of the Sun and Stars*, ed. Y. Osaki and H. Shibahashi (Lecture Notes in Physics, No. 367; Berlin: Springer-Verlag), 257.

Durrant, C. J., and Schroeter, E. 1983, *Nature*, **301**, 589.

Duvall, T. L., Jr. and Harvey, J. W. 1983, *Nature*, **302**, 24.

Duvall, T. L., Jr., and Harvey, J. W. 1984, *Nature*, **310**, 19.

Duvall, T. L., Jr., Harvey, J. W., and Pomerantz, M. A. 1986, *Nature*, **321**, 500.

Edmunds, M. G., and Gough, D. O. 1983, *Nature*, **302**, 810.

Evans, J. W., and Michard, R. 1961 *Ap. J.*, **136**, 493.

Fossat, E., Gelly, B., and Grec, G. 1989, In *Astrophysics in Antarctica*, ed. D. J. Mullan, M. A. Pomerantz, and T. Stanev (AIP Conf. Proc. 198; New York: AIP), 231.

Fossat, E., and Grec, G. 1978, In *Pleins Feux sur la Physique Solaire*, ed. J. Rösch (Paris: CNRS), 151.

Fossat, E., Harvey, J., Hausman, M., and Slaughter, C. 1977, *Astron. Astrophys.*, **59**, 279.

Fossat, E., and Ricort, G. 1973, *Solar Phys.*, **28**, 311.

Fossat, E., and Ricort, G. 1975, *Astron. Astrophys.*, **43**, 243.

Frazier, E. N. 1968, *Zeit. Astrophys.*, **68**, 345.

Fröhlich C. 1984, *Mem. S. A. It.*, **55**, 237.

Fröhlich, C., and Delache P. 1984, In *Solar Seismology from Space* (NASA JPL Publ. 84-84), 183.

Fröhlich, C., Toutain, T., Bonnet, R. M., Bruns, A. V., Delaboudinière, J. P., Domingo, V., Kotov, V. A., Killath, Z., Rashkovsky, D. N., Vial, J, C., and Wehrli, Ch. 1990, In *Inside the Sun*, ed. G. Berthomieu and M. Cribier (Dordrecht: Kluwer), 279.

Fröhlich, C., and van der Raay, H. B. 1984, In *The Hydromagnetics of the Sun*, ed. T. D. Gutenne and J. J. Hunt (Noordwijk: ESTEC), 17.

Germain, M. E., and Hill, H. A. 1988, SCLERA Monograph Series in Astrophysics, no. 10.

Gonzi, G., and Roddier, F. 1969, *Solar Phys.*, **8**, 255.

Gough D. O. 1980, In *Nonradial and Nonlinear Stellar Pulsation*, ed. H. A. Hill and W. A. Dziembowski (Lecture Notes in Physics, No. 125; Berlin: Springer-Verlag), 273.

Grec, G., and Fossat, E. 1977, *Astron. Astrophys.*, **55**, 411.

Grec, G., and Fossat, E. 1979, *Astron. Astrophys.*, **77**, 351.

Grec, G., Fossat, E., and Pomerantz, M. 1980, *Nature*, **288**, 541.

Grec, G., Fossat, E., and Pomerantz, M. 1983, *Solar Phys.*, **82**, 55.

Harvey, J. 1988, In *Seismology of the Sun and Sun-Like Stars*, ed. E. Rolfe, ESA SP-286 (Noordwijk: ESA Pub. Div.), 55.

Harvey, J. W. 1990, In *Progress of Seismology of the Sun and Stars*, ed. Y. Osaki and H. Shibahashi (Lecture Notes in Physics, No. 367; Berlin: Springer-Verlag), 115.

Henning, H. M., and Scherrer, P. H. 1986, In *Seismology of the Sun and the Distant Stars*, ed. D. O. Gough (Dordrecht: Reidel), 55.

Hill, F. 1990, In *Inside the Sun*, ed. G. Berthomieu and M. Cribier (Dordrecht: Kluwer), 265.

Hill, F., and Newkirk, G. A. 1985, *Solar Phys.*, **95**, 201.

Hill, F., Toomre, J., and November, L. J. 1983, *Solar Phys.*, **82**, 411.

Hill, H. A. 1978, In *The New Solar Physics*, ed. J. A. Eddy (Boulder: Westview Press), 135.

Hill, H. A. 1985a, *Ap. J.*, **290**, 765.

Hill, H. A. 1985b, SCLERA Monograph Series in Astrophysics, no. 3.

Hill, H. A. 1992, *Ap. J. Sup.*, **78**, 283.

Hill, H. A., Alexander, N., and Caudell, T. P. 1985, SCLERA Monograph Series in Astrophysics, no. 2.

Hill, H. A., and Caudell, T. P. 1979, *Mon. Not. R. Astr. Soc.*, **186**, 327.

Hill, H. A., and Caudell, T. P. 1985, Ap. J., **299**, 517.

Hill, H. A., Caudell, T. P., and Rosenwald, R. D. 1976, *Ap. J.*, **213**, L81.

Hill, H. A., Fröhlich, C., Gabriel, M., and Kotov, V. A. 1991, In *Solar Interior and Atmosphere*, ed. A. N. Cox, W. C. Livingston and M. S. Matthews (Tucson: University of Arizona Press), 562.

Hill, H. A., and Gu, Yeming 1990, *Science in China* (Series A), **33**, 854.

Hill, H. A., and Kroll, R. 1986, SCLERA Monograph Series in Astrophysics, No. 5.

Hill, H. A., Livingston, W. C., and Caudell, T. P. 1977, *Ap. J.*, **214**, L137.

Hill, H. A., Rosenwald, R. D., and Caudell, T. P. 1978, *Ap. J.*, **225**, 304.

Hill, H. A., Stebbins, R. T., and Brown, T. M. 1976, In *Atomic Masses and Fundamental Constants*, Vol. 5, ed. J. H. Sanders and A. H. Wapstra (New York: Plenum), 622.

Hill, H. A., Stebbins, R. T., and Oleson, J. R. 1975, *Ap. J.*, **200**, 484.

Hill, H. A., Tash, J., and Padin, C. 1986, *Ap. J.*, **304**, 560.

Howard, R. 1962, *Ap. J.*, **136**, 211.

Isaak, G. R. 1986, In *Seismology of the Sun and the Distant Stars*, ed. D. O. Gough (Dordrecht: Reidel), 223.

Isaak, G. R., van der Raay, H. B., Pallé, P. L., and Roca Cortés, T. 1984, *Mem. S. A. It.*, **55**, 353.

Jackson, J. D. 1975, *Classical Electrodynamics* (New York: Wiley).

Jefferies, S. M., Pomerantz, M. A., Duvall, T. L., Jr., Harvey, J. W., and Jaksha, D. B. 1988, In *Seismology of the Sun and Sun-Like Stars*, ed. E. J. Rolfe (Noordwijk: ESTEC), 279.

Jiménez, A., Pallé, P. L., Régulo, C., Roca Cortés, T., Elsworth, Y. P., Isaak, G. R., Jefferies, S. M., McLeod, C. P., New, R., van der Raay, H. B. 1988, In *Advances in Helio- and Asteroseismology*, ed. J. Christensen-Dalsgaard and S. Frandsen (IAU Symp. Proc. no. 123; Dordrecht: D. Reidel), 215.

Jiménez, A., Pallé, P. L., Roca Cortés, T., and Domingo, V. 1988, *Astron. Astrophys.*, **193**, 298.

Jiménez, A., Pallé, P. L., Roca Cortés, T., Domingo, V., and Korzennik, S. 1987, *Astron. Astrophys.*, **172**, 323.

Leighton, R. B. 1961, In *Aerodynamic Phenomena in Stellar Atmospheres: Proc. IAU Symp. 12*, ed. R. N. Thomas, *Nuovo Cimento Suppl.*, **22**, 321.

Leighton, R. B., Noyes, R. W., and Simon, G. W. 1962, *Ap. J.*, **135**, 474.

Libbrecht, K. G., Woodard, M. F., and Kaufman, J. M. 1990, *Ap. J.*, **359**, 232.

Livingston, W., Milkey, R., and Slaughter, C. 1977, *Ap. J.*, **211**, 281.

Mahlman, G. W., Nottingham, W. B., and Slater, J. C. 1956, In *Photconductivity Conference*, ed. R. G. Breckenridge (New York: Wiley), 489.

Mein, P. 1966, *Ann. Astrophys.*, **29**, 153.

Mihalis, D. 1978, *Stellar Atmospheres* (New York: Freeman).

Musman, S., and Nye, A. H. 1977, *Ap. J.*, **212**, L95.

Musman, S., and Rust, D. M. 1970, *Solar Phys.*, **13**, 261.

Oglesby, P. H. 1987, Ph.D. dissertation, University of Arizona.

Oglesby, P. H. 1993, SCLERA Symposium: *Selected Topics in Science and Technology*, November 19–22, 1991, Tucson, Arizona. To be published in the Conference Proceedings.

Oglesby, P. H., Hill, H. A., Rabaey, G. F. 1989, *Adv. Space Res.*, **8**, No. 7, 115.

Oleson, J. R., Zanoni, C. A., Hill, H. A., Healy, A. W., Clayton, P. D., and Patz, D. L. 1974, *Appl. Opt.*, **13**, 206.

Ott, H. W. 1988, *Noise Reduction Techniques in Electronic Systems* (New York: Wiley).

Otnes, R. K., and Enochson, L. D. 1978, *Applied Time Series Analysis* (New York: Wiley).

Pallé, P. L., Régulo, C., and Roca Cortés, T. 1990a, In *Inside the Sun*, ed. G. Berthomieu and M. Cribier (Dordrecht: Kluwer), 349.

Pallé, P. L., Régulo, C., and Roca Cortés, T. 1990b, In *Progress of Seismology of the Sun and Stars*, ed. Y. Osaki and H. Shibahashi (Lecture Notes in Physics, No. 367; Berlin: Springer-Verlag), 129.

Reif, R. J., and Musman, S. 1971, *Solar Phys.*, **20**, 257.

Rhodes, E. J., Jr., Ulrich, R. K., Harvey, J. W., and Duvall, T. L., Jr. 1981, In *Solar Instrumentation: What's Next ?*, ed. R. B. Dunn (Sunspot: SPNO), 37.

Rhodes, E. J., Jr., Ulrich, R. K., and Simon, G. W. 1977, *Ap. J.*, **218**. 901.

Richard, J-P. 1975, In *General Relativity and Gravitation*, ed. G. Shaviv and J. Rosen (New York: Wiley), 169.

Scargle, J. D. 1982, *Ap. J.*, **263**, 835.

Scherrer, P. H., Wilcox, J. M., Christensen-Dalsgaard, J., and Gough, D. O. 1983, *Solar Phys.*, **82**, 75.

Scherrer, P. H., Wilcox, J. M., Severny, A. B., Kotov, V. A., and Tsap, T. T. 1979, *Nature*, **277**, 635.

Scherrer, P. H., Wilcox, J. M., Severny, A. B., Kotov, V. A., and Tsap, T. T. 1980, *Ap. J.*, **237**, L97.

Schmidt-Kaler, T., and Winkler, C. 1984, *Mem. S. A. It.*, **55**, 231.

Severny, A. B., Kotov, V. A., and Tsap, T. T. 1976, *Nature*, **259**, 87.

Shibahashi, H. 1990, In *Progress of Seismology of the Sun and Stars*, ed. Y. Osaki and H. Shibahashi (Lecture Notes in Physics, No. 367; Berlin: Springer-Verlag), 3.

Stebbins, R. T. 1980, In *Nonradial and Nonlinear Stellar Pulsation*, ed. H. A. Hill and W. A. Dziembowski (Lecture Notes in Physics, No. 125; Berlin: Springer-Verlag), 394.

Stebbins, R. T. and Wilson, C. 1983, *Solar Phys.*, **82**, 43.

Stein, R. F., and Leibacher, J. 1974, *Ann. Rev. Astron. Astrophys.*, **12**, 407.

Tanenbaum, A. S., Wilcox, J. M., Frazier, E. N., and Howard, R. 1969, *Solar Phys.*, **9**, 328.

Ulrich, R. K. 1970, *Ap. J.*, **162**, 993.

Ulrich, R. K., Rhodes, E. J., Jr., Cacciani, A., and Tomczyk, S. 1984, In *Solar Seismology from Space*, (NASA JPL Publ. 84-84), 263.

Unno, W., Osaki, Y., Ando, H., and Shibahashi, H. 1979, *Nonradial Oscillations of Stars* (Tokyo: Univ. of Tokyo Press).

Volland, H. 1988, *Atmospheric Tidal and Planetary Waves* (Dordrecht: Kluwer).

Whitaker, W. A. 1963, *Ap. J.*, **137**, 914.

Wolff, C. L. 1972, *Ap. J.*, **177**, L87.

Woodard, M. 1984, *Nature*, **309**, 530.

Woodard, M., and Hudson, H. 1983, *Nature.*, **305**, 589.

Woodard, M., and Hudson, H. 1983, *Solar Phys.*, **82**, 67.

Woodard, M. F., Kuhn, J. R., Murray, N., and Libbrecht, K. G. 1991, *Ap. J.*, **373**, L81.

Worden, S. P., and Simon, G. W. 1977, *Ap. J.*, **210**, L163.